



# Master's Thesis

## Multiphoton and heralded entanglement sources for applications in quantum cryptography

Mikkel Thorbjørn Mikkelsen

### Supervisor

Prof. Peter Lodahl

<lodahl@nbi.ku.dk>

### Second Supervisor

Prof. Ravitej Uppu

<ravitej-uppu@uiowa.edu>

Submitted on the 14<sup>th</sup> of June 2021



This page was intentionally left blank.

## Abstract

Qubit entanglement is a key enabler of secure communication protocols of tomorrow. The robust nature of photons against environmental influences makes these viable encoding candidates for quantum information processing over long distances. Heralded qubit entanglement enables cryptography based on device-independent quantum key distribution (DIQKD), which promises unconditional security, relying on only the validity of quantum physics. The work on this thesis demonstrates heralded entanglement generation using highly indistinguishable pure single-photons. The single-photon source is based on an InAs/GaAs quantum dot coupled to an 'on-chip' planar nanophotonic waveguide circuit. Upon pulsed excitation of the quantum dot, it emits a temporal chain of single photons which is demultiplexed (temporal-to-spatial modes) to create a four-photon source. A single-photon rate of 2.3Mhz is observed to result in a demultiplexed four-fold coincidence rate of 3.4Hz, with a lower bound indistinguishability of  $V_{HOM} = (84.8 \pm 1.7)\%$  for superimposed output modes. The four-photon source has been employed in a quantum gate for heralded entanglement generation. We here observe a violation of Bell's inequality (more specifically the Clauser-Horne-Shimony-Holt inequality) within  $3\sigma$ , i.e.  $S = 2.24 \pm 0.08$ . The quantum correlation fringe visibility achieved of  $V_E = (81.3 \pm 0.8)\%$  predicts an even greater violation of  $S = 2.30 \pm 0.02$ . Further, the security of E91 based DIQKD protocols are dependent on detection loophole free Bell inequality violation. This can be achieved by heralding the presence of an Einstein-Podolsky-Rosen pair with means of the ability to distinguish between Bell states. We here propose a design for a thin-film metasurface implementation of partial Bell state measurement to realise a low-loss device. The estimated output fidelity reaches  $F = 94.1\%$  proving a viable platform for this purpose.

## Acknowledgements

First of all, I would like to thank Peter Lodahl for giving me the opportunity to carry out my Master's thesis in the Quantum Photonics group at the Niels Bohr Institute. Too Ravitej Uppu who has been my daily supervisor I owe a special thanks for his patience in the countless hours of lab training and for always finding time to help me and answer my questions, in addition, to proofread my thesis, even after moving halfway around the world. Thank you!

A great thanks go out to the laboratory hack-master Martin Appel for always taking his time to answer my questions and for sharing his expertise on laboratory temperature issues. I would also like to stress my gratitude towards Camille Papon, Ying Wang, and Freja Pedersen for their help and guidance on the source setup. A Thanks also to Patrik Sund for great sparring and help on the demultiplexing setup and for proofreading parts of my thesis for which I also would like to thank Eric Planz. Thank you Vasiliki Angelopoulou for your always friendly disposition and a great thanks to Adam Knorr, Arianne Brooks, Carlos Faurby, Mathias Staunstrup, Simon Pabst, Sif Fugger, and Celeste Qvortrup for great fun, sparring, and coexistence in the master student life.

Last but certainly not least endless thanks to my dear Karen and our son Erik for their love and patience during this year, and thanks to Erik's little brother for waiting to announce his arrival until I finished writing my thesis.

---

# Contents

---

<b>Introduction</b>	<b>1</b>
<b>1 Theoretical background and motivation</b>	<b>3</b>
1.1 Qubits	3
1.2 Entanglement	5
1.2.1 The CHSH inequality	5
1.3 Applications	7
1.3.1 Quantum key distribution	7
1.3.2 Device-independent quantum key distribution	8
<b>2 Single Photon Source</b>	<b>10</b>
2.1 Quantum emitters	10
2.1.1 Semiconductors	10
2.1.2 Quantum dots	11
2.1.3 Spontaneous emission	12
2.1.4 Resonance fluorescence	14
2.2 Photonic nanostructures	15
2.3 Source setup and efficiency	17
2.4 Characterisation and goodness of source	19
2.4.1 Single-photon purity	19
2.4.2 Photon indistinguishability	22
2.5 Summary	27
<b>3 Temporal-to-spatial mode conversion</b>	<b>28</b>
3.1 Demultiplexing	28
3.2 Active demultiplexing	29
3.2.1 Polarisation modulators	29
3.3 Scheme and operation	30
3.3.1 Experimental limitations	31
3.3.2 Switching efficiency and alignment	32
3.4 Timing	34
3.5 Four-fold rates	35
3.6 Demultiplexed photon indistinguishability	37
3.7 Summary	40
<b>4 Heralded entanglement generation</b>	<b>41</b>

4.1	Heralded entanglement gate operation . . . . .	41
4.2	State evolution . . . . .	42
4.3	Heralding efficiency . . . . .	44
4.4	Experimental setup alignment and characterisation . . . . .	45
4.4.1	HWP alignment and characterisation . . . . .	46
4.4.2	Transmission efficiency . . . . .	49
4.4.3	Mode matching . . . . .	50
4.5	Entanglement confirmation . . . . .	52
4.6	Experimental results . . . . .	53
4.7	Summary . . . . .	61
<b>5</b>	<b>Metasurface design proposal for partial Bell state measurement</b>	<b>62</b>
5.1	Partial Bell state measurement . . . . .	62
5.2	Metasurfaces . . . . .	64
5.2.1	Matrix Fourier optics . . . . .	64
5.3	Metasurface partial Bell state measurement . . . . .	65
5.4	Summary . . . . .	68
<b>6</b>	<b>Conclusion and outlook</b>	<b>69</b>
	<b>Bibliography</b>	<b>72</b>
<b>A</b>	<b>Appendix</b>	<b>78</b>
A.1	Single photon detectors . . . . .	78
A.2	Transformation matrices of optical elements in partial Bell state measurement	79
A.3	Metasurface design transformation matrix . . . . .	80

---

# Introduction

---

In the beginning of the 20<sup>th</sup> century quantum mechanics made its entrance shaking the very foundations of physics as it was known. It all began in 1901 with the quantified radiation postulate by Planck's radiation law[1] forming the basis for the wave-particle duality of light. This new idea was complimented by Einstein's photoelectric effect in 1905[2] and Bohr's atomic model with discretized energy states[3]. The intrinsic random nature in quantum mechanics [4] that emerged in the formalism developed by Heisenberg, Schrödinger, Dirac among others, revolutionised the understanding of the microscopic world.

In 1935 Einstein, Podolsky and Rosen(EPR) presented a critique of non-local correlations or "spooky action at a distance", claiming the description of quantum mechanical theory to be incomplete, in what is referred to as the EPR paradox[5]. Three decades later Bell proposed an inequality to test whether predictions of quantum mechanics are correct or that physics must apply to local realism[6]. The phenomenon that was under trial in the EPR paradox was *entanglement*, describing the non-local correlations between two or more quantum mechanical entities. Recently, loophole-free Bell inequality violations has been demonstrated[7, 8, 9] delivering statistically significant evidence of quantum correlations.

Quantum information theory emerged from the fusion of quantum- and information-theory. By incorporating the principle of quantum mechanical superposition into information processing, classical bits are replaced by quantum bits(qubits) enabling new information processing protocols. Especially in the field of computation[10] and cryptography[11, 12], the quantum advantage is proposed to be significant. Recent progress in quantum computers[13] does especially motivate a new take on cryptography as the security of the present most widely used cryptography protocols is based on complexity of mathematical problems e.g. hardness of factorisation. Such problems are a difficult task for a classical computer, but for a quantum computer it is significantly easier (i.e. could arrive at a solution faster). Quantum cryptography on the other hand, such as device independent quantum key distribution(DIQKD)[14] solely relies on the physics of quantum mechanics for security. The key resource for DIQKD is high rate, on demand heralded entangled qubits, i.e. EPR pairs.

Photonic qubits, also referred to as flying qubits, are strong candidates for quantum cyptography. These can be easily manipulated using linear optical components and efficiently transmitted over long distances at the speed of light with very low losses.

The goal of this thesis is to demonstrate temporal-to-spatial mode demultiplexing of a four-photon source from a high-purity, indistinguishable single-photon source based on InAs/GaAs quantum dot embedded in a photonic nanostructure. The four-photon source

will subsequently be implemented in quantum gate protocol for entanglement generation based on an entanglement gate scheme proposed in [15] in a push towards DIQKD. A design proposal for a metasurface grating [16] to do a Bell state measurement is also presented, which is a key component in DIQKD protocols. A schematic overview of the project is shown in fig. 0.1.

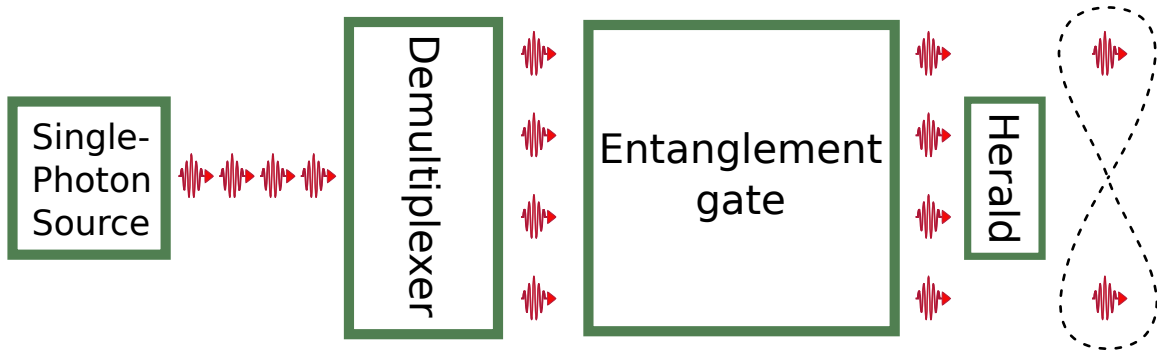


Figure 0.1: Schematic overview of the full experimental setup of this work; from the generated stream of single photons to the generation of a heralded entangled photon pair. The single photon source is discussed in chapter 2, the demultiplexer is discussed in chapter 3 and the entanglement gate and implemented heralding is discussed in chapter 4. In chapter 5 an alternative design for a heralding station is presented based on metasurface gratings.

- Chapter 1 introduces the basic theory of qubits and operations along with the phenomena of entanglement and how to quantify the non-local nature of EPR pairs. Subsequently, a motivational section briefly introducing quantum key distribution (QKD) and DIQKD.
- Chapter 2 covers the basics of semiconductor quantum dot(QD) single photon emitters embedded in nanostructures. The goodness of the source in terms of purity and indistinguishability is also introduced and experimentally determined for a specific QD employed in the subsequent chapters.
- Chapter 3 introduces an efficient method to generate a multi-photon source using temporal to spatial mode conversion of a single-photon source. The single photon source introduced in chapter 2 is then implemented, and the indistinguishability across output modes are experimentally determined.
- Chapter 4 introduces a heralded entanglement generation scheme along with alignment and characterisation of the setup. Subsequently, the chapter discusses the experimental demonstration of Bell inequality violation, using the demultiplexed single photon source presented in chapter 3 and chapter 2, as a fundamental evidence of quantum correlations.
- Chapter 5 puts forward a proposal for a metasurface grating design for Bell state measurement implementation to be used on EPR pairs in the photon polarisation basis.



---

# Chapter 1

## Theoretical background and motivation

---

Quantum information processing is based on information encoded in strings of qubits. These quantum entities are key enablers for any quantum information schemes, e.g in quantum cryptography[12, 11, 17]. In this chapter, qubits as fundamental encoding units of quantum information processing are introduced, both as single quantum transistors and multi-qubit systems. For multi-qubit systems, a correlation phenomena known as entanglement is presented along with an experimental validation method of such quantum correlations. Lastly this chapter briefly introduces the concept of quantum key distribution(QKD) and device independent quantum key distribution(DIQKD), as a motivational factor for pursuing high rate heralded entanglement generation.

### 1.1 Qubits

Classical information processing is based on a simple indivisible binary platform consisting of binary digits that can take only one of two values. Depending on the encoding unit, this can be either  $\{1, 0\}$ ,  $\{\text{true}, \text{false}\}$ ,  $\{\text{on}, \text{off}\}$  etc.. These most basic information holders are called a *bit*, from contraction of "binary digit". Strings of bits permeate all modern information technology and are the information holders that, when scaled up, are the building blocks on which computers, currency, information encryption etc. are based.

The quantum analogy is called quantum bits or *qubits*. A qubit describes a state in the simplest possible quantum system, which live in a two-dimensional complex *Hilbert space* [18] in the orthonormal basis  $\{|0\rangle, |1\rangle\}$  - these two states are called the *computational basis states*[19]. A qubit differs from the classical bit, with the property of being able to be in a superposition(linear combination) of the two classical bit values. The most general normalised qubit state is

$$|\psi\rangle = \alpha|0\rangle + \beta|1\rangle, \quad (1.1)$$

where  $\alpha, \beta \in \mathbb{C}$ . Measuring a qubit requires projecting it onto the computational basis states which will yield the outcome  $|0\rangle$  with probability  $|\alpha|^2$  and  $|1\rangle$  with probability  $|\beta|^2$ , which naturally leads to the normalisation requirement  $|\alpha|^2 + |\beta|^2 = 1$ . Upon a measurement, the

qubit state will collapse onto a new state, that differs from its previous state, which we can not retrieve information about. This property also distinguishes a qubit from a classical bit. We may measure a classical bit and decipher all of the information that it encodes without disturbing the system [18] in contrast to the qubit.

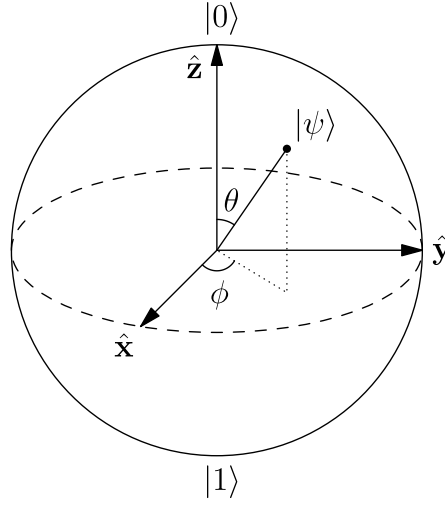


Figure 1.1: The Bloch sphere. Any pure cubit can be represented as a vector of unity length on this sphere.

A qubit can be geometrically represented on a Bloch sphere as seen in fig. 1.1, where the qubit state in eq. (1.1) due to its normalisation can be rewritten as [19]

$$|\psi\rangle = \cos(\theta/2)|0\rangle + e^{i\phi}\sin(\theta/2)|1\rangle, \quad (1.2)$$

where  $\theta$  and  $\phi$  are interpreted as the polar and azimuthal angle in a spherical coordinate system in fig. 1.1. In this representation all pure states (states which probability constants normalise to unity) are represented on the Bloch sphere that has a radius of unity.

A qubit is physically prepared in a quantum mechanical two-level system. This system could be a spin- $\frac{1}{2}$  particle where the spin up  $|\uparrow\rangle$  and spin down  $|\downarrow\rangle$  would form the binary basis. In this work, photonic qubits, also known as *flying qubits*, are the central quantum system. Photon qubits can be encoded in the number-, timebin- or polarisation-basis, the latter will be the focus in this work. In the polarisation basis the binary basis is  $\{|H\rangle, |V\rangle\}$ , which corresponds to a horizontal polarised photon and vertical polarised photon respectively, which in vector notation reads

$$|H\rangle = \begin{pmatrix} 0 \\ 1 \end{pmatrix}, \quad |V\rangle = \begin{pmatrix} 1 \\ 0 \end{pmatrix}. \quad (1.3)$$

For ease of computation we may introduce the bosonic creation  $\hat{a}_{H,V}^\dagger$  and annihilation  $\hat{a}_{H,V}$  operators [4]. With this notation, the polarisation encoded photonic qubit may be written as

$$|\psi\rangle_A = (\alpha\hat{a}_H^\dagger + \beta\hat{a}_V^\dagger)|0\rangle, \quad (1.4)$$

where  $|0\rangle$  is the vacuum state in the Fock basis for photon number [20], and the subscript  $|\rangle_A$  holds information about the mode to which the creation/annihilation operators apply.

When applying the creation operators to the vacuum state, it becomes  $|\psi\rangle_A = \alpha |H\rangle_A + \beta |V\rangle_A$ . The bosonic creation and annihilation operators apply to the following commutation relations[4]

$$[\hat{a}_i^\dagger, \hat{a}_j^\dagger] = [\hat{a}_i, \hat{a}_j] = [\hat{a}_i, \hat{a}_j^\dagger] = 0, \quad [\hat{a}_i, \hat{a}_j] = \delta_{ij}. \quad (1.5)$$

Classical information processing require bits in strings to encode more complex information than simple true/false. Qubits may also exist in strings for similar purposes.

Take a bipartite qubit system, which lives in the composite Hilbert space  $\mathcal{H}_A \otimes \mathcal{H}_B$  where  $\mathcal{H}_A$  and  $\mathcal{H}_B$  are the Hilbert spaces of the two individual qubits. Qubits can in this systems be written as  $|i\rangle_A \otimes |j\rangle_B = |ij\rangle_{AB}$ , where  $i, j \in \{1, 0\}$ , such that an arbitrary pure state in the bipartite system is given by

$$|\psi\rangle_{AB} = \alpha_{00} |00\rangle_{AB} + \alpha_{01} |01\rangle_{AB} + \alpha_{10} |10\rangle_{AB} + \alpha_{11} |11\rangle_{AB}, \quad (1.6)$$

which again is normalized to unity  $|\alpha_{00}|^2 + |\alpha_{01}|^2 + |\alpha_{10}|^2 + |\alpha_{11}|^2 = 1$ . This notation can be generalised to systems of N qubits  $|\psi\rangle_{AB\dots N}$ . In this notation  $\hat{a}_k^\dagger \hat{b}_l^\dagger |0\rangle = |kl\rangle_{AB}$  where  $k, l \in \{H, V\}$  which may be generalised to multi qubit systems such as  $|HHV\dots H\rangle_{ABC\dots\mu}$ . This notation may be useful when describing multiple qubits.

## 1.2 Entanglement

If a bipartite pure state consisting of the individual states  $|\psi\rangle_A$  in  $\mathcal{H}_A$  and  $|\psi\rangle_B$  in  $\mathcal{H}_B$  is a direct product of the individual states, the bipartite state is *separable*. If this is not the case, the state is non-separable also known as *entangled*, which means that A and B have *quantum correlations*[18]

$$\underbrace{|\psi\rangle_{AB} = |\psi\rangle_A \otimes |\psi\rangle_B}_{\text{Seperable}}, \quad \underbrace{|\psi\rangle_{AB} \neq |\psi\rangle_A \otimes |\psi\rangle_B}_{\text{non-Seperable}}. \quad (1.7)$$

For two qubits in a bipartite quantum system the maximally entangled states are known as EPR pairs or Bell states and are given by[21]

$$|\Psi^\pm\rangle = \frac{1}{\sqrt{2}} (|01\rangle_{AB} \pm |10\rangle_{AB}), \quad (1.8)$$

$$|\Phi^\pm\rangle = \frac{1}{\sqrt{2}} (|00\rangle_{AB} \pm |11\rangle_{AB}). \quad (1.9)$$

### 1.2.1 The CHSH inequality

Consider a bipartite system(AB) where Alice has access the observables  $\mathbf{a}$  and  $\mathbf{a}'$  of system A and Bob has access to the observables  $\mathbf{b}$  and  $\mathbf{b}'$  of system B. All observables can take values  $\{\pm 1\}$ . Assuming local realism, where Alice and Bob are able to measure both of their respective observables which are uncorrelated, such that the observables are functions of hidden random variables, it follows that if  $\mathbf{a} + \mathbf{a}' = 0$  then  $\mathbf{a} - \mathbf{a}' = \pm 2$  and if  $\mathbf{a} + \mathbf{a}' = \pm 2$  then  $\mathbf{a} - \mathbf{a}' = 0$ . By defining a parameter  $C$ , the following equation must hold

$$C \equiv (\mathbf{a} + \mathbf{a}') \mathbf{b} + (\mathbf{a} - \mathbf{a}') \mathbf{b}' = \pm 2. \quad (1.10)$$

From the triangle inequality<sup>1</sup> it follows that  $|\langle C \rangle| \leq \langle |C| \rangle = 2$ , such that the measurable S parameter must comply to the inequality referred to as the Clauser-Horne-Shimony-Holt(CHSH) inequality [22]

---

<sup>1</sup>  $|\int f(x)dx| \leq \int |f(x)|dx$

$$S = |\langle \mathbf{a}\mathbf{b} \rangle + \langle \mathbf{a}'\mathbf{b} \rangle + \langle \mathbf{a}\mathbf{b}' \rangle - \langle \mathbf{a}'\mathbf{b}' \rangle| \leq 2, \quad (1.11)$$

which must hold for any local realist theory. The correlations described by quantum theory however violates this inequality, which can be shown[18] by considering the observables  $\mathbf{a}$ ,  $\mathbf{a}'$ ,  $\mathbf{b}$ ,  $\mathbf{b}'$  as Hermitian operators

$$\mathbf{a} = \vec{\sigma}^A \cdot \hat{a}, \quad \mathbf{a}' = \vec{\sigma}^A \cdot \hat{a}', \quad (1.12)$$

$$\mathbf{b} = \vec{\sigma}^B \cdot \hat{b}, \quad \mathbf{b}' = \vec{\sigma}^B \cdot \hat{b}'. \quad (1.13)$$

Here  $\hat{a}$ ,  $\hat{a}'$ ,  $\hat{b}$  and  $\hat{b}'$  are unitary vectors that designate the projection on the Bloch sphere, in fig. 1.1, that Alice and Bob can measure in, and  $\vec{\sigma}^{A(B)} = \sigma_x^{A(B)}\hat{x} + \sigma_y^{A(B)}\hat{y} + \sigma_z^{A(B)}\hat{z}$  is the Pauli vector. Considering quantum correlations with the maximally entangled Bell state  $|\Psi^-\rangle$ , we may calculate the expectation value of the correlation between operators  $\mathbf{a}$  and  $\mathbf{b}$ :

$$\langle \mathbf{a}\mathbf{b} \rangle = \langle \Psi^- | \mathbf{a}\mathbf{b} | \Psi^- \rangle = \langle \Psi^- | (\vec{\sigma}^A \cdot \hat{a})(\vec{\sigma}^B \cdot \hat{b}) | \Psi^- \rangle. \quad (1.14)$$

As  $|\Psi^-\rangle$  is invariant if Alice and Bob each apply the same unitary transformation[18] it follows that

$$(\vec{\sigma}^A + \vec{\sigma}^B) |\Psi^-\rangle = 0 \Rightarrow \vec{\sigma}^A |\Psi^-\rangle = -\vec{\sigma}^B |\Psi^-\rangle, \quad (1.15)$$

which implies that we may write the expectation value in eq. (1.14) as

$$\langle \mathbf{a}\mathbf{b} \rangle = -\langle \Psi^- | (\vec{\sigma}^A \cdot \hat{a})(\vec{\sigma}^A \cdot \hat{b}) | \Psi^- \rangle = -a_i b_i \text{Tr}\{\rho_A \sigma_i^A \sigma_j^A\} \quad (1.16a)$$

$$= -a_i b_i \delta_{ij} = -\hat{a} \cdot \hat{b} \quad (1.16b)$$

$$= -\cos(\theta_{ab}). \quad (1.16c)$$

Here  $\theta$  is the angle between the chosen measurements axis  $\hat{a}$  and  $\hat{b}$  as shown in fig. 1.2. We see that the observables  $\mathbf{a}$  and  $\mathbf{b}$  are anti-correlated depending on this angle. This derivation can be generalised to all the expectation values of the S parameter in eq. (1.11). If we now consider the case shown in fig. 1.2 where  $\hat{a}$ ,  $\hat{a}'$ ,  $\hat{b}$  and  $\hat{b}'$  are co-planar in the plane spanned by  $\hat{x}$  and  $\hat{z}$ , and separated by a  $\pi/4$  angle, such that  $\theta_{ab} = \theta_{a'b} = \theta_{ab'} = \pi/4$  and  $\theta_{a'b'} = 3\pi/4$ , then the CHSH inequality may be written as

$$S = | -\cos\theta_{ab} - \cos\theta_{a'b} - \cos\theta_{ab'} + \cos\theta_{a'b'} | \quad (1.17)$$

$$= 4 \cdot \frac{1}{\sqrt{2}} = 2\sqrt{2} \geq 2, \quad (1.18)$$

which outlines that the quantum mechanical prediction clearly violates the CHSH inequality. Quantum mechanics predicts the correlation between two observables  $\mathbf{a}$  and  $\mathbf{b}$  to be given by  $\langle \mathbf{a}\mathbf{b} \rangle = -V \cos\theta_{ab}$  assuming the experimentally obtained fringe visibility  $V$  is unity. In practice, the visibility is less than one setting a limit on the obtainable  $S$  parameter value. This is given by the supremum  $\sup\{S\} = V2\sqrt{2}$  effectively putting a violation thresh hold of the CHSH inequality given by the visibility

$$V > \frac{1}{\sqrt{2}} \approx 0.71, \quad (1.19)$$

Achieving a fringe visibility above  $1/\sqrt{2}$  predicts a violation of the CHSH inequality in eq. (1.11).

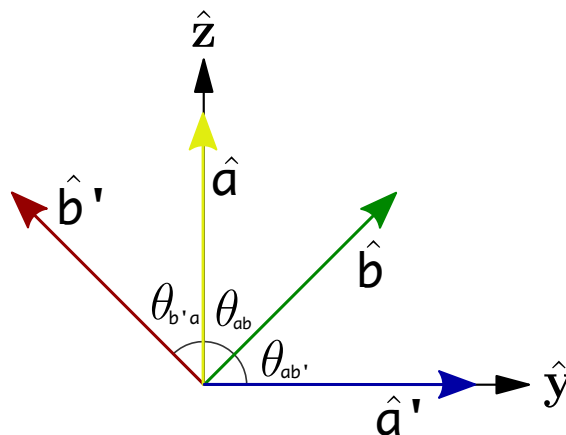


Figure 1.2: Choise of measurement axis  $\hat{a}$ ,  $\hat{a}'$ ,  $\hat{b}$  and  $\hat{b}'$  with which the maximal violation of the CHSH inequality is achieved in the same coordinate system as the Bloch sphere in fig. 1.1.

### 1.3 Applications

Single photons are a viable resource for different quantum protocols due to their robustness against environmental influences. Furthermore, photons travels at the speed of light, making it the fastest known information carrier. This make single photons strong candidates for communication and cryptography protocols[23].

The era of the internet has brought a vast need for secure communication. Symmetric cryptography relies on a priori exchange of secrets such as encryption keys and authentication keys between the communicating parties(e.g. Alice and Bob)[24]. *Public key* systems, such as the widely used asymmetric RSA(Rivest–Shamir–Adleman)[25], use secret private keys combined with public keys to encrypt/decrypt a secret message. This eliminates the problem that key distribution is facing by allowing Alice to encrypt a message to Bob prior to sharing a private key. The security of these types of classical cryptography protocol relies on unproven mathematical assumptions, e.g. hardness of factorisation or the computation of discrete logarithms. Also these protocols suffer from a blind spot when it comes to the cloneability of the digitally stored keys compromising the security of the protocol. With increasing success rate with quantum computers[13], capable of breaking these types of mathematical problems, classical cryptography is facing a serious security threat. In contrast to asymmetric cryptography the security of quantum cryptography protocols relies solely on the fundamentals of quantum physics[23], and hence comes with the promise of unconditional security.

In this section, two quantum cryptography protocols are introduced to motivate why Device-Independent Quantum Key Distribution(DIQKD) is a promising next-step in the development of safer communication and why a high rate heralded Bell state gun is a key building block.

#### 1.3.1 Quantum key distribution

Quantum key distribution (QKD) is the quantum analogy of classical key distribution protocols, and works on the principle of one-time pad for encrypting secret messages. The first protocol for QKD was proposed by C. H. Bennett and G. Brassard in 1984[17], commonly referred to as BB84. The protocol in the photon polarisation basis only requires one single photon source, but has since also been implemented with weak coherent light sources[23].

The working principle of the BB84 protocol starts with Alice sending a photon polarisation qubit  $\{|1\rangle, |0\rangle\}$  to Bob in either the rectilinear basis(R)  $\{|\rightarrow\rangle, |\uparrow\rangle\}$  or in the diagonal basis(D)  $\{|\swarrow\rangle, |\nearrow\rangle\}$ , where  $|\uparrow\rangle$  is a vertical polarised photon,  $|\rightarrow\rangle$  is a horizontal polarised photon,  $|\swarrow\rangle = 1/\sqrt{2}(|\rightarrow\rangle + |\uparrow\rangle)$  and  $|\nearrow\rangle = 1/\sqrt{2}(|\rightarrow\rangle - |\uparrow\rangle)$ . The bit value and basis is chosen randomly. Next, Bob measures the received photon projecting it on to either basis D or R, also chosen randomly. When Bob uses the same basis as Alice, he will measure the correct bit value every time, but when Bob measures on a  $|\uparrow\rangle$  or  $|\rightarrow\rangle$  state in the diagonal basis, the measurement outcome will be  $|\nearrow\rangle$  or  $|\swarrow\rangle$  both with 50% probability and vice versa. On a public line Alice and Bob may now compare basis and keep the bit values with coincident basis choice. Alice and Bob now share a private key for use in a one-time pad information exchange. An example of the protocol is detailed in table 1.1, with overlapping basis choice shown in red and green.

The security of this protocol is based on the quantum *no cloning theorem*[18], which states that it is not possible to clone a quantum state. Imagine an eavesdropper(Eve) on the line that intercepts a photon and passes on a copy to Bob, in the hope that the two parties do not notice her presence. Eve intercepts this photon by measuring it in either the R or D basis. There is a 50% chance that Eve chooses the same basis as Alice and hence get the right bit value, and may send an identical photon on to Bob. Nothing is noticed. But should Eve choose the wrong basis and pass on a photon in the opposite basis to what Alice initially sent the photon in, there is a 50% chance that Bob will measure the wrong bit value with a basis choice identical with Alice's. As a result there is a 25% chance that a bit value evaluated by Bob and Alice that has been intercepted by Eve will not coincide. By sacrificing a number of bits in the share key(red in table 1.1) and comparing bit values on a public channel, Alice and Bob may now ensure the privacy of the quantum channel. An example of an eavesdropper indicator is shown by white X in a black box in table 1.1.

	Random bit	1	0	0	1	1	0	0	1	0	1	0	1
Alice	Random basis	R	D	R	R	R	D	R	D	R	D	D	R
	Polarization	$\rightarrow$	$\swarrow$	$\uparrow$	$\rightarrow$	$\rightarrow$	$\swarrow$	$\uparrow$	$\nearrow$	$\uparrow$	$\nearrow$	$\swarrow$	$\rightarrow$
Bob	Random basis	D	D	D	R	D	D	R	R	D	R	D	R
	Outcome	0	0	0	1	1	0	1	1	0	0	0	1
shared bit			0		1		0	X			0	1	

Table 1.1: Example of the completion of BB84 protocol, from the generation of the bit string until sharing the secret key. Green columns shows the key shared with matching measuring basis. Red columns shows the sacrificed shared bits for privacy validation. White X in a black box indicates the presence of Eve.

In practice, the promise of unconditional security does however not hold. Real life implementations of QKD rarely conform to the assumptions made in idealised models used in security proofs, that neglect many relevant device imperfections. Especially photon detectors are vulnerable components for loopholes such as side channel attacks [26] and detector control attack [27], and the protocol does, like classical key distribution, rely on an a priori exchange of classical authentication keys.

### 1.3.2 Device-independent quantum key distribution

In a publication from 1991[12], Eckert proposed a QKD protocol based on Bell's theorem referred to as E91. In this protocol Alice and Bob each receive one half of a specific EPR pair(e.g. singlet state  $|\Psi^-\rangle = 1/\sqrt{2}(|01\rangle - |10\rangle)$ ) generated by Charlie, a third party. Now

Alice may apply one out of three measurement basis  $\{A_0, A_1, A_2\}$  and Bob may measure the received state in either of the basis  $\{B_0, B_1, B_2\}$  all chosen at random, and proceed to compare basis on a public channel in resemblance to the BB84 protocol. The security of the protocol relies on a Bell test on a sacrificed portion of the compared measurements. If the result is within the constraints of Bell's inequality, Eve could not have tampered with the photons and hence dismantle the quantum correlations. However, shortly after publication it was proven that the security of E91 in its original form using EPR pairs and Bell's inequality violation was not exceeding that of BB84, but was only equivalent [28].

A little more than a decade after Ekerts paper, modifications to E91 were proposed [11, 29, 14] introducing a new type of QKD known as device-independent QKD (DIQKD). To understand how DIQKD differs from regular QKD we may first clarify the assumptions under which the security of any QKD is proven[14]:

1. *Quantum physics is correct,*
2. *Alice's and Bob's physical locations are secure,*
3. *They have a trusted random number generator,*
4. *They have trusted classical devices (e.g., memories and computing devices),*
5. *They share an authenticated, but otherwise public, classical channel,*
6. *Alice and Bob must trust their respective quantum devices.*

What distinguished DIQDK from other QKD protocols is that the security is not based on the 6<sup>th</sup> assumption: The trust in the quantum devices. As the security of QKD are limited by the quantum devices used, this assumption relaxation offers security against more powerful attacks. In DIQKD it is assumed that Eve has access and control of both source and measuring devices. This means that the only data available to Alice and Bob to make a bound on Eve's information is the observed correlation between classical in- and outputs, without any assumption on the type of quantum measurement and systems used for their generation. The non-local nature of the EPR pair is the physical principle on which all device-independent security proofs are based. Bell inequalities are the only entanglement witness that are device-independent, such that the physical details underlying Alice's and Bob's apparatuses do not play a vital role[14]. To ensure the security of the DIQKD protocol a loophole-free violation of Bell's inequality is required. Both the locality and detection loophole must be closed; however, while closing the locality loophole only requires ensuring a determined distance between Alice and Bob, the detection loophole demands very high transmission efficiencies[14]. To overcome this a heralding mechanism can be employed in a central heralding station(CHS) as proposed by [30], that can be implemented as a partial Bell state measurement. The CHS creates entanglement by measurement(entanglement swapping) between the pair of photons shared by Alice and Bob whilst sending a classical message to Alice and Bob that they are ready to measure the entangled photons, thus avoiding the detection loophole. High rate heralded photonic Bell state generators are hence key to realise fast and contemporary secure cryptography.

---

## Chapter 2

# Single Photon Source

---

Photonic qubits are key enablers for long distance quantum-information processing as discussed in chapter 1. The first part of this chapter presents a single photon source based on self assembled InAs/GaAs quantum dots(QD) embedded in nanophotonic structures. Basic theory of the QD energy levels and light matter interaction enabling single photon emission is then discussed. Next the experimental setup for the QD single photon source manipulation is presented and the goodness of the emitted single photons is evaluated.

### 2.1 Quantum emitters

Quantum emitters exist in a variety of formats. Spontaneous parametric down conversion and atom-like systems are two very commonly used platforms. Atoms enable high rate single photon emission, but implementation/trapping of single atoms in optical systems is a difficult task; hence, atom-like solid state emitters, e.g QDs, has in recent years attracted a great deal of interest[31].

In this thesis a QD single-photon source is presented and employed. QDs are also known as artificial atoms, as they due to three dimensional confinement of the electrons that gives rise to discrete energy levels, behaves similarly to an isolated two level system. A QD is a solid state semiconductor heterostructure that can be grown, e.g. by self-assembly, in a given semiconductor material utilising molecular-beamepitaxy.

#### 2.1.1 Semiconductors

In general two types of materials exist: Metals and insulators. Where insulators has a band gap at Fermi level(chemical potential), metals do not. I.e., for insulators the valence band(VB) is completely filled and the conduction band(CB) utterly empty at 0Kelvin. For a solid to be conducting, charge carriers that can repopulate must be present. For an insulator with filled VB and empty CB no such carrier is available and this material does not conduct current. This is a result of electrons being fermions; thus, must apply by *Pauli's exclusion principle*, which does not allow two electrons to populate the same state [4]. In the case of a metal, when a band is partially filled, the electrons can repopulate when a small electric field is applied and in this manor conduct current.



Semiconductors are a subgroup of insulators which is generally classified by their electrical resistivity at room temperature ( $10^{-5}\Omega\text{m}$  to  $10^6\Omega\text{m}$ ) [32]. What distinguished semiconductors from insulators is their VB to CB energy band gap ( $< 4\text{eV}$  for semiconductors[33]). Due to the small band gap energy, electrons in the VB of a semiconductor may be optically or thermally excited at room temperature to the CB leaving behind a vacant orbital or a hole in the VB. Both CB electrons and VB holes contributes as charge carriers to the electrical conductivity of the semiconductor[32]. The energy band gaps of the three different materials are shown in fig. 2.1a.

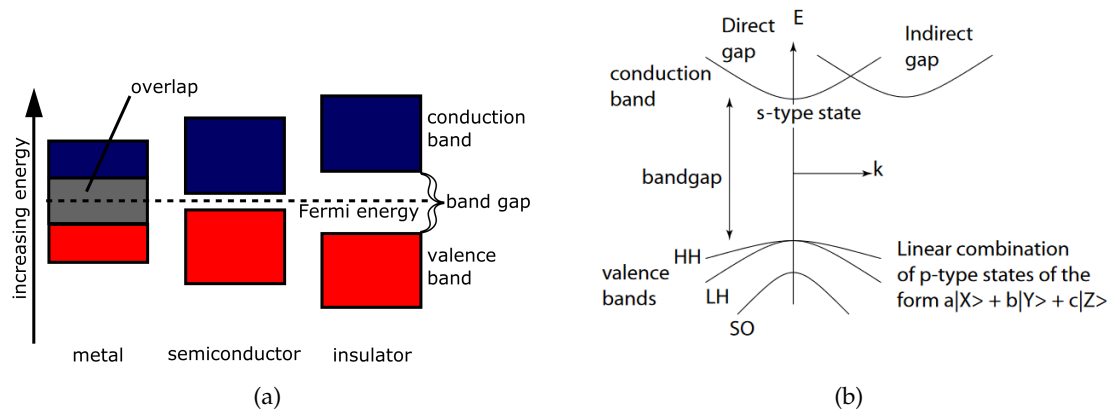


Figure 2.1: (a) a schematic drawing of the energy levels of a solid. The red colour represents occupied orbitals, and the blue unoccupied. The boxes represent the available energy levels(bands) due to the dispersion relation of the solid. Reprinted from [34], (b) schematic illustration of dispersion for a semiconductor. Here it is visualised how a direct and indirect band gap appears. Due to momentum conservation, electrons may only excite/decay at direct band gaps.

Amongst the variety of semiconductor materials that exists, a very interesting group is the **III-V** compound semiconductors(alloys containing elements from groups **III** and **V** of the periodic table). **III-V** compounds are of special interest in optical physics due to superior electronic properties including: **1.** high electron mobility, **2.** direct band gaps and **3.** exciton(bound state of an electron and an electron hole) binding energies at optical frequencies. The second property is important as the selection rules governing optical transitions require momentum conservation ( $\Delta k = 0$ ). A band gap structure illustrating direct and indirect band gaps is shown in fig. 2.1b.

From the solid state structure of **III-V** semiconductors, the valence band splits into three sub-bands which are the heavy hole(HH), light hole(LH) and split-off band(SO) visualised in fig. 2.1b. Due to quantum confinement, the HH band has the highest energy; hence,  $\text{CB}\rightarrow\text{HH}$ -band is usually the addressed transition.

### 2.1.2 Quantum dots

The working principle of a QD is the combination of the electronic band structure of two semiconductors to form a trapping potential acting as a two-level system. QDs are made from two semiconductors with different bandgap energies. Such combination of materials are referred to as *heterostructures*. A QD is a small islands of a semiconductor(e.g. InAs) with a direct band gap of energy  $\Delta E_1$  surrounded by another semiconductor(e.g. GaAs) with a bandgap of  $\Delta E_2$ , with  $\Delta E_1 < \Delta E_2$  as illustrated in Figure 2.2b. In contrast to a quantum well(1D confined quantum emitter) and a quantum nanowire(2D quantum emitter), the

quantum dot is confined in all three spatial dimensions effectively creating a zero-dimensional (0D) nanostructure[32].

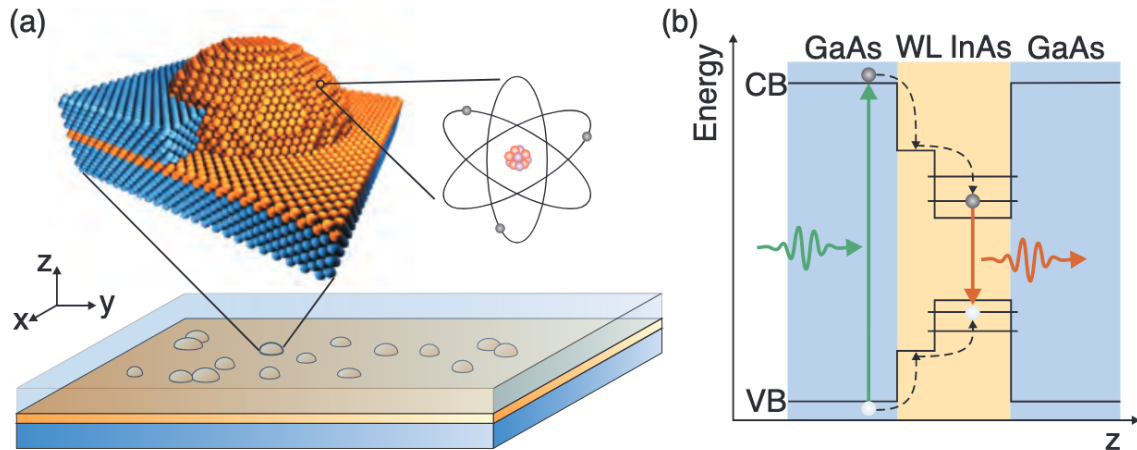


Figure 2.2: Structure and energy diagram of a self-assembled InAs/GaAs QD. **(a)** Sketch of a self-assembled QD that is formed in the interface between GaAs(blue) and InAs(orange) layers. The spontaneous growth appears due to lattice strain in the interface between GaAs and the InAs wetting layer(WL). **(b)** Illustration of the confined bandgap of the InAs QD embedded in GaAs. Illustration shows a typical optical transition scheme: A photon(green) with energy close to the bandgap of GaAs is absorbed exciting an electron to the CB and leaving behind a hole in the VB. These particles can now act as electronic charge carriers and will relax to the ground state of an exciton in the QD and recombine whilst emitting a single photon(orange) of InAs band gap energy. Reprinted from [35]

The excited state of a QD is called an *exciton* and appears when an electron of the VB is excited to the CB e.g. by being optically addressed. In such an event the CB is occupied by one electron and a hole is left behind in the VB. This electron-hole pair form the exciton bound state, which upon recombination emits a photon with energy equal to the band gap. A hole is quasiparticle, i.e. a theoretical approach to the absence of an electron in the VB, which has been excited to the CB. This can be treated as a positively charged particle equivalent to a positron in the effective mass approximation [33].

### 2.1.3 Spontaneous emission

A QD has multiple energy levels and can as a result undergo multiple different excitations and decays. Though, by spectral filtering and polarisation control of the excitation laser it is possible to almost only address a single transition, effectively making the QD behave like a two-level system. When an exciton is excited, this may undergo spin-flip into a dark state. This mechanism is for simplification neglected in this section, simplifying the QD energy-levels to the highlighted white area in fig. 2.3. The presence of the dark state is reintroduced as a loss factor when discussing the source efficiency in section 2.3.

An excitation confined in a QD will spontaneously recombine, emitting a photon with band gap energy. The spontaneous emission is a consequence of the emitters coupling to a continuum of radiation modes  $\omega_{\mathbf{k}}$ . This behaviour can be modelled using the Wigner-Weisskopf theory, which holds when  $\omega_{\mathbf{k}}$  varies insignificantly over the linewidth of the emitter[36]. Considering the QD emitter in the dipole approximation, and neglecting high frequency interaction terms(Rotating wave approximation), the Hamiltonian governing the light matter interaction of the QD emitter is given by three terms accounting for **1** the two-level system(TLS), **2** the radiation *field* and **3** the *interaction*, respectively:

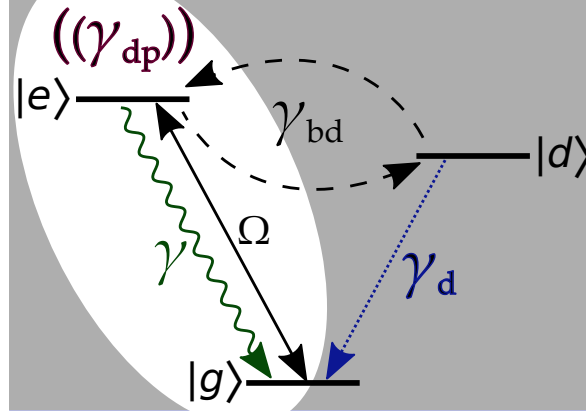


Figure 2.3: Three level diagram, including a dark excitation state  $|d\rangle$  in addition to the bright excitation state  $|e\rangle$  and ground state  $|g\rangle$ . Only decay rates and coupling terms highlighted in the white area is included in the model in eq. (2.10).

$$\hat{H} = \underbrace{\frac{1}{2}\hbar\omega_0\hat{\sigma}_{eg}\hat{\sigma}_{ge}}_{TLS} + \underbrace{\sum_{\mathbf{k}}\hbar\omega_{\mathbf{k}}\hat{a}_{\mathbf{k}}^\dagger\hat{a}_{\mathbf{k}}}_{field} + \underbrace{\sum_{\mathbf{k}}\hbar\left[g_{\mathbf{k}}\hat{\sigma}_{eg}\hat{a}_{\mathbf{k}}e^{i(\omega_0-\omega_{\mathbf{k}})t} + \text{h.c.}\right]}_{Interaction}. \quad (2.1)$$

Here  $\omega_0$  is the quantum dot resonance frequency,  $\hat{\sigma}_{ij} = |i\rangle\langle j|$  is the emitter-population inversion operator with  $i, j \in \{g, e\}$ ,  $\hat{a}_{\mathbf{k}}$  and  $\hat{a}_{\mathbf{k}}^\dagger$  are the quantized field operators for photon mode  $\mathbf{k}$  and 'h.c.' is short for Hermitian conjugate. The coupling strength to each optical mode is given by the electric dipole matrix element  $g_{\mathbf{k}}(\mathbf{r}_0) = i\mathbf{d}_{eg} \cdot \mathbf{E}_{\mathbf{k}}^*(\mathbf{r}_0)/\hbar$ . The sum over  $\mathbf{k}$  includes full polarisation range. At a given time the TLS may be considered to be in the excited state and the field in the vacuum state, i.e.  $\psi = |e\rangle|0\rangle$ . In accordance with the system Hamiltonian in eq. (2.1) the emitter may decay into the ground state, emitting a photon of frequency  $\omega_{\mathbf{k}}$  into mode  $|1\rangle_{\mathbf{k}}$  such that the final state of the system is  $\psi = |g\rangle|1\rangle_{\mathbf{k}}$ .

There exist several ways of solving the decay dynamics of a two-level system coupled to a continuum of radiation modes. One may continue with Schrödinger's equation in the Heisenberg picture and solve for the probability amplitude dynamics of the full state vectors. Here we will continue in the master equation approach. It can be shown[37] that the dynamics of the reduced density matrix for a harmonic oscillator(H.O.) coupled to a bath of H.Os (a system such as the QD and environment) in the Markov approximation is governed by the *master equation* in the interaction picture:

$$\dot{\rho}(t) = -\frac{\gamma}{2}(\bar{n} + 1)[\hat{\sigma}_{ge}\hat{\sigma}_{eg}\rho(t) - \hat{\sigma}_{eg}\rho(t)\hat{\sigma}_{ge}] - \frac{\gamma}{2}\bar{n}[\rho(t)\hat{\sigma}_{eg}\hat{\sigma}_{ge} - \hat{\sigma}_{ge}\rho(t)\hat{\sigma}_{eg}] + \text{h.c.} \quad (2.2)$$

Here it is assumed that the reservoir is thermal, with mean photon number  $\bar{n}$ , and the decay rate  $\gamma = 2\pi\mathcal{D}(\omega_0)|g(\omega_0)|^2$  is introduced as the product of the Density of Optical States (DOS),  $\mathcal{D}(\omega_0)$ , at the emitter frequency and the coupling strength of the light matter interaction( $g(\omega_0)$ ) which again can be shown to have the form [36]

$$\gamma = \frac{\pi d_{eg}^2}{\epsilon_0\hbar}\omega_0\mathcal{D}(\mathbf{r}_0, \omega_0, \mathbf{e}_d). \quad (2.3)$$

Here  $\mathcal{D}(\mathbf{r}_0, \omega_0, \mathbf{e}_d)$  is the Local Density of States (LDOS), which specifies the number of optical states at the frequency  $\omega$  per frequency bandwidth and volume as experienced by

the emitter[36]. Returning to the master equation (eq. (2.2)), the equations of motion of the two-level system, may be solved by considering the density matrix

$$\rho(t) = \sum_{i,j} \rho_{ij}(t) |i\rangle \langle j|, \quad i, j \in \{g, e\}, \quad (2.4)$$

which is given by the outer product of the possible states weighted by the overlap of the states as a matrix element  $\rho_{ij} = \langle i | \rho | j \rangle$ . In the situation of interest the structure, in which the two-level system(QD) is embedded in, is cooled to  $\simeq 1.6\text{K}$ , meaning that the thermal photon number may be assumed to vanish, i.e.  $\bar{n} = 0$ . Now, by inserting the density matrix of eq. (2.4) into the master equation in eq. (2.2), we may derive the equations of motion for the populations of the two states and the off-diagonal elements of the density matrix:

$$\begin{pmatrix} \dot{\rho}_{gg}(t) \\ \dot{\rho}_{ge}(t) \\ \dot{\rho}_{eg}(t) \\ \dot{\rho}_{ee}(t) \end{pmatrix} = \begin{bmatrix} 0 & 0 & 0 & \gamma \\ 0 & -\gamma/2 & 0 & 0 \\ 0 & 0 & -\gamma/2 & 0 \\ 0 & 0 & 0 & -\gamma \end{bmatrix} \begin{pmatrix} \rho_{gg}(t) \\ \rho_{ge}(t) \\ \rho_{eg}(t) \\ \rho_{ee}(t) \end{pmatrix}. \quad (2.5)$$

The density matrix leads to the excited state population dynamics given by

$$\dot{\rho}_{ee}(t) = -\gamma\rho_{ee}(t) \quad \rightarrow \quad \rho_{ee}(t) = \rho_{ee}(0)e^{-\gamma t}, \quad (2.6)$$

with decay rate given in eq. (2.3). We see that the rate at which the emitter decays is highly dependent on the LDOS which for solid state QDs can be engineered by introducing nanophotonic structures.

#### 2.1.4 Resonance fluorescence

In section 2.1.3 the coupling between the emitter in the excited state and a continuum of reservoir modes leading to spontaneous emission is described. In this section the focus is on the excitation of the QD i.e. bringing the emitter into the excited state. Various methods exists for this purpose: The QD can be excited by above-band excitation, p-shell excitation and resonant excitation. The third method is referred to as resonance fluorescence and is the one implemented this thesis. With resonance fluorescence the QD is irradiated with a laser of same frequency as the QD excitation energy i.e. in *resonance* with the QD. The Rabi model[20] describes this scenario assuming the laser to be a strong monochromatic classical field  $\mathbf{E} = \mathcal{E} \cos(\omega_L t)$  and the QD a two-level system. In the rotating frame oscillating with  $\omega_L$  the Hamiltonian in the dipole approximation governing the system is described by:

$$H_{Rabi} = \hbar\Delta\hat{\sigma}_{eg}\hat{\sigma}_{ge} + \hbar\frac{1}{2}(\Omega\hat{\sigma}_{eg} + \Omega^*\hat{\sigma}_{ge}). \quad (2.7)$$

Here  $\Delta = \omega_0 - \omega_L$  is the detuning between the laser and the two-level systems resonance frequency and  $\Omega = -\mathbf{d} \cdot \mathcal{E} / \hbar$  is the Rabi frequency of the driving field at zero detuning. The state of the system(S) can now be described by the reduced density operator  $\rho_S(t) = \text{Tr}_R[\rho_{SR}(t)]$  where the reservoir(R) is traced out of the full system-reservoir(SR) density operator. The dynamics of resonance fluorescence can efficiently be described in the interaction picture with the *master equation* formalism. The master equation is based on the equations of motion of the system with the assumption that the reservoir is memoryless i.e. the frequency response of the reservoir is constant with the bandwidth of the system known as the *Markov approximation*

and assuming vacuum in the radiation continuum. The equation of motion is then given by[37]

$$\dot{\rho}(t) = -\frac{i}{\hbar} [H_{Rabi}, \rho(t)] + \mathcal{L}_\gamma(\rho(t)) + \mathcal{L}_{dp}(\rho(t)), \quad (2.8)$$

where the Linblad superoperator  $\mathcal{L}(\cdot)$  accounts for the two decay mechanisms: Spontaneous emission of the QD( $\gamma$ ) and pure dephasing  $\gamma_{dp}$ . The Linblad Superoperator is given by

$$\mathcal{L}_\gamma(\rho(t)) = \sum_{k,l} \frac{\gamma_{kl}}{2\hbar^2} (2\hat{\sigma}_{kl}\rho(t)\hat{\sigma}_{kl} - \hat{\sigma}_{kk}\rho(t) - \rho(t)\hat{\sigma}_{ll}), \quad (2.9)$$

where  $k, l \in \{g, e\}$ . The pure dephasing only affects the off diagonal terms, i.e.  $k, l = eg$  or  $ge$  as this describes the loss of coherence due to interaction with the environment. Hence, this has no effect on the state population ( $k, j = ee$  or  $gg$ ). The master equation describes the dynamics of the density operator  $\rho(t)$  of the system governed by eq. (2.7), where the reservoir is traced out of the SR density operator such that the information about the system is found in the density matrix. By projecting the equation of motion on to the four matrix elements of the two-level system  $\langle k | \rho | l \rangle$  where  $k, l = \{e, g\}$  we may arrive at the *optical Bloch equations*

$$\begin{pmatrix} \dot{\rho}_{gg}(t) \\ \dot{\rho}_{ge}(t) \\ \dot{\rho}_{eg}(t) \\ \dot{\rho}_{ee}(t) \end{pmatrix} = \begin{bmatrix} 0 & i\frac{\Omega}{2} & -i\frac{\Omega^*}{2} & \gamma \\ i\frac{\Omega}{2} & -\frac{\gamma}{2} - \gamma_{dp} + i\Delta & 0 & -i\frac{\Omega}{2} \\ -i\frac{\Omega}{2} & 0 & -\frac{\gamma}{2} - \gamma_{dp} - i\Delta & i\frac{\Omega^*}{2} \\ 0 & -i\frac{\Omega}{2} & i\frac{\Omega^*}{2} & -\gamma \end{bmatrix} \begin{pmatrix} \rho_{gg}(t) \\ \rho_{ge}(t) \\ \rho_{eg} \\ \rho_{ee} \end{pmatrix}. \quad (2.10)$$

When driving the QD continuously by e.g. applying a continuous wave(CW) driving field, the steady state solution ( $\dot{\rho}(t) = 0$ ) of the excited state population can be found to be[38]

$$\rho_{ee}(t \rightarrow \infty) = \frac{\Omega^2}{\gamma} \frac{\gamma + 2\gamma_{dp}}{4\Delta^2 + (\gamma + 2\gamma_{dp})(\gamma + 2\gamma_{dp} + 2\Omega^2/\gamma)}. \quad (2.11)$$

The steady solution of the optical Bloch equation of the two-level system is important for deriving a fit model for the experimental measure of the second order correlation function used in section 2.4.1 to characterise the single photon purity of the single photon source. For the actual implementation of the source resonance fluorescence, pulsed excitation is preferable in order to enable a triggering of the QD single photon emission. Calculations do however intensify drastically considering pulsed excitation and requires numerical methods to describe the time dynamics and fluorescence spectrum(Fourier transform). Pulsed excitation can be modelled with a temporal Gaussian envelope function such that the Rabi frequency is

$$\Omega(t) = \frac{\Omega_0}{\sqrt{2\pi}\delta} e^{-(t-t_0)^2/\delta^2}, \quad (2.12)$$

where  $\Omega_0$  is the pulse area,  $\delta$  is the width of the pulse and  $t_0$  is the temporal centre of the pulse. Solutions to the pulsed excitation of the QD is important for proper operation of the single photon source and is discussed in [38][39].

## 2.2 Photonic nanostructures

By controlling the environment in which the QD is embedded, it is possible to affect the decay rate of the QD as well as effectively guide the emitted photons to realise a near-unity

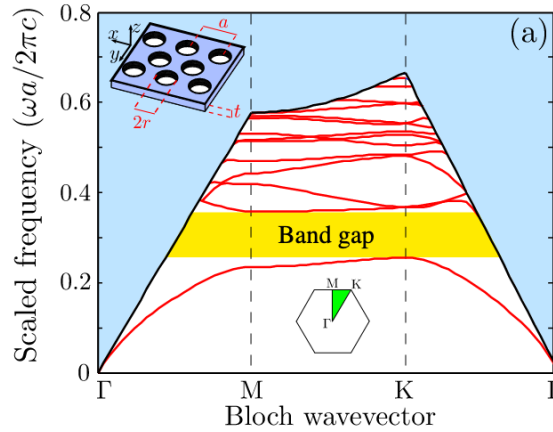


Figure 2.4: Band diagram of a 2D photonic crystal(PC) membrane made from GaAs for TE-like modes. The photonic band gap is shown shaded in yellow and the blue area corresponds to unbound modes(leaky modes). The blue print in upper left corner shows the structure of the PC. Reprinted from [36]

efficiency single-photon source. For this purpose an engineered photonic nano-structure called a photonic crystal wave guide (PCWG) is fabricated on the sample containing the QDs. Photonic crystals(PC) are inhomogeneous dielectric materials, where the refractive index is modulated periodically on the scale of the optical wavelength. By choosing the semiconductor GaAs with a refractive index of  $n_{GaAs} \approx 3.5$  with periodic air holes  $n_{air} \approx 1$ , large refractive index contrast PC can be obtained. These structures effectively lead to total

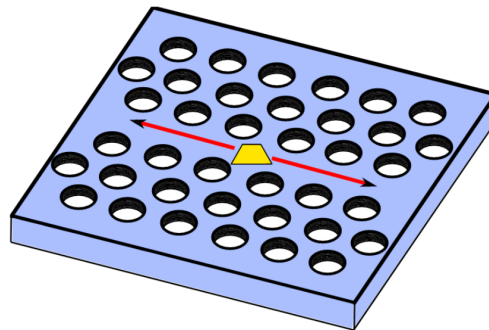


Figure 2.5: Schematic drawing of a photonic crystal wave guide (PCWG) made by Gallium Arsenide in blue with periodic etched air voids in white. The defect Channel in the middle effectively guides the light mode in plane due to Bragg scattering and out of plane due to total internal reflection. The yellow trapez exemplifies the positioning of a QD in the PCWG. Reprinted from [36]

Bragg scattering arising from the periodic refractive index creating a photonic band gap as shown in fig. 2.4. By fabricating a structure with a defect line(line of missing air holes) as depicted in fig. 2.5 the light in the waveguide is trapped by total Bragg scattering in the in-plane dimension. Out of plane the light is trapped by total internal reflection, where light is guided in a higher refractive index material than the surrounding material, leading to total internal reflection for incidence angles greater than the critical angle [36]. These effects can be utilised not only for PCWG, but also for engineering cavities, mirrors or filters.

A PC is also characterized by its spatially periodic dielectric permittivity  $\varepsilon(\mathbf{r})$ , for which the imaginary component accounts for absorption in the material. Semiconductor materials can be constructed to have a vanishing absorption for a desired frequency range, i.e.  $\text{IM}[\varepsilon(\mathbf{r})] \sim 0$ , which is the case for GaAs at IR wavelengths.

A quantum dot embedded in a PCWG may couple to both a guided mode and non-guided modes (modes leaking out of the PCWG). The decay rate of the QD into the guided mode is given by  $\gamma_{wg}$  while the decay into non-guided modes is  $\gamma_{ng}$ . Furthermore, the QD can decay by intrinsic non radiative processes for which the decay rate is given by  $\gamma_{nrad}$ [40]. Naturally the decay into the guided modes is of high interest and is quantified by the  $\beta$ -factor:

$$\beta = \frac{\gamma_{wg}}{\gamma_{wg} + \gamma_{ng} + \gamma_{nrad}}, \quad (2.13)$$

where  $\beta = 1$  corresponds to a deterministic single-photon source, emitting a photon into the wave guide upon excitation. For self-assembled InAs QDs embedded in a GaAs PCWG  $\beta = 98.43 \pm 0.04\%$  has been experimental achieved in [40], whilst a Chip-to-fiber coupling of  $> 60\%$  has been achieved in [41].

## 2.3 Source setup and efficiency

The QD used in this work is an InAs self-assembled heterostructure on a 170 nm-thin suspended GaAs membrane. The PCW is terminated with high-efficiency shallow-etched grating (SEG) outcouplers for collection of the QD emission. A scanning electron microscope (SEM) image of the PCW with SEG outcouplers is shown in fig. 2.6b. The bidirectional waveguides with grating outcouplers at each end is used to perform resonant transmission measurement for selecting a QD that is well-coupled to the PCW, as the self-assembled QDs are randomly distributed. The membrane constitutes an ultra-thin p-i-n diode used to apply an electric field across the QD to reduce charge noise, control the charge state and to Stark tune the QD emission wavelength. The bias voltage across the QD is tuned using a low-noise high-resolution DC voltage source. The sample, on which the structure containing QD and PCWG is located, is cooled to 1.6K in a cryostat with optical and electrical access. The QD is excited from the top of the sample using a wide field-of-view confocal microscope with a high numerical aperture objective. This same objective is used to collect QD emission at the grating outcoupler, which is then imaged onto a single-mode optical fibre. The excitation and collection paths are separated at a 10:90 (reflection:transmission) beam splitter, with the 90% transmission path for collection. The QD emission collected in the fibre is spectrally filtered using a 3.5GHz linewidth etalon (free spectral range: 100 GHz) to suppress the emission in the phonon sideband. This setup is schematically shown in fig. 2.6a. The QD is tuned with a bias voltage of  $\sim 1.25\text{V}$  to ensure selective excitation of the neutral exciton  $X_0$  with emission wavelength  $\lambda = 942.0\text{nm}$ , which is spectrally overlapped with the etalon filter and the excitation laser.

### Setup efficiency

The efficiency of the single photon source can be split up into the QD source efficiency and the setup efficiency. The transmittance of the collection optics is estimated at  $\eta_{optics} = (41 \pm 3)\%$ , which includes the optical elements, objective and fibre coupling. The SEG outcouplers has a finite outcoupling efficiency, which on similar samples has been measured to be  $\eta_{gr} = (47 \pm 3)\%$ [38] and a wave guide propagation efficiency  $\eta_{prop} \simeq 96\%$  leading to an estimation of the total outcoupling efficiency of

$$T = \eta_{prop}\eta_{gr}\eta_{optics} = (18.5 \pm 1.8)\%. \quad (2.14)$$

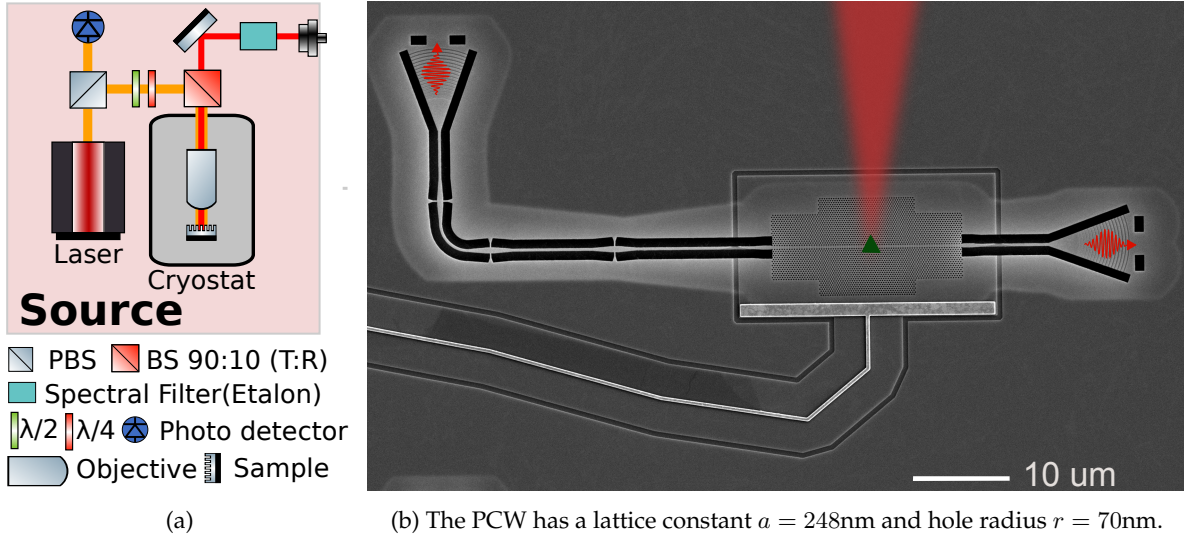


Figure 2.6: (a) Schematic of the source setup. The setup is included in the full experimental setup presented in fig. 4.8. (b) SEM image of sample with the photonic crystal waveguide structure (PCWG), exemplified QD marked with green triangle. Resonant top excitation laser and emitted single photons in red. The photons are coupled out of the waveguide in the shallow-etched grating forming a Y-structure at each end. Metal electrical contacts (P-contact visible in bottom of the PCWG) are used for applying a gate voltage across the QD embedded in the 170 nm thin membrane.

The waveguide in fig. 2.6b is bidirectional and the QD emission couples equally to both directions, which limits the efficiency to 50%. Lastly the spectral filter transmittance is  $\eta_m > 80\%$ , leading to a total setup efficiency of  $\eta_{setup} \simeq 7.4\%$ . The setup efficiencies are summarised in table 2.1.

Component	Efficiency
PWC directionality	50%
Total Outcoupling $T$	$(18.5 \pm 2.0)\%$
Spectral filter $\eta_f$	$> 80\%$
Total setup efficiency $\eta_{setup}$	7.4%

Table 2.1: Setup efficiency  $\eta_{setup}$ .

The source efficiency is intrinsically limited by the quantum efficiency of the quantum dot itself. This includes: **1** loss of emission due to partially exciting the wrong dipole. The neutral exciton  $X_0$  has two bright states corresponding to spectrally non-degenerate dipoles (fine structure splitting of  $\sim 7.5$  GHz) with orthogonal linear polarisation. The half- and quarter-wave plate in fig. 2.6a are implemented to optimize the coupling by polarisation control to address only the efficiently coupled dipole. The second dipole contribution is not observed in the QD emission spectrum, which is why this efficiency is assumed to be  $> 98\%$ , which is what we usually observe [39]. **2** red and blue shifted emission in a broad phonon sideband due to inelastic scattering between the exciton and phonons in the suspended membrane under strict resonant excitation. As we operate the sample at the temperature 1.6K in resemblance to [39], we here assume the efficiency  $\sim 95\%$ . The phonon sideband is filtered out by the etalon spectral filter. **3** coupling to the dark exciton (i.e. non radiative) state via spin-flip limiting the efficiency to  $\sim 98\%$  [38]. **4** loss due to QD emission coupling into non-guided modes. The location of the QD in the photonic crystal waveguide determines the



coupling of the dipoles, quantified by the non-unitary  $\beta$ -factor. The efficiency is on average observed in the order of  $\sim 90\%$  in these structures[39, 38]. All four loss contributions are not characterised for the specific QD used in the experimental setup, but based on previously characterisations on similar structures. These all contributes to a rough estimate of the total source efficiency of  $\eta_{QD} \approx 82\%$ . Combining the QD source and setup efficiency, the total single photon source efficiency is estimated to be

$$\eta_S = \eta_{QD}\eta_{setup} \approx 6.1\%. \quad (2.15)$$

The QD is in the experimental setup excited with a pulsed laser at a repetition frequency of  $F_{ex} = 76.152\text{MHz}$ , leading to an expected single photon rate of  $F_{SP} = F_{ex}\eta_S = 4.6\text{MHz}$ . The single photon rate is measured with SNSPDs to be  $2.5\text{MHz}$ . The used SNSPDs has an efficiency of  $65\%$ (appendix A.1) resulting in a single photon rate of  $3.8\text{MHz}$  corresponding to a  $5.0\%$  source efficiency. The disparity can here probably be attributed to a lower  $\beta$ -factor than expected and a slight misalignment in the collection optics.

## 2.4 Characterisation and goodness of source

A perfect single photon source emits anti-bunched and indistinguishable photons. The goodness measure of merit for these two properties are presented and experimentally demonstrated in this section on the QD single photon source employed in this work with an emission wavelength of  $\lambda = 942.0\text{nm}$ .

### 2.4.1 Single-photon purity

Correlation properties of a single photon stream are key indicators for a good single-photon source. The correlation properties of a stream of photons are quantified by the quantum correlation functions. The coherence of emitted photons is described by the normalised first order correlation function

$$g^{(1)}(t, \tau) = \frac{\langle \hat{a}^\dagger(t)\hat{a}(t+\tau) \rangle}{\langle \hat{a}^\dagger(t)\hat{a}(t) \rangle}. \quad (2.16)$$

Here  $\hat{a}^\dagger(t)$ ( $\hat{a}(t)$ ) is the single-mode field creation(annihilation) operator, and  $\tau$  is the correlation time delay. The first order correlation function is a measure of the coherence of two light sources (or a single light source split on a beam splitter(BS)) by measuring its interference properties. From the correlation of the field at different times the emission spectrum can be calculated[20]. Perfectly monochromatic light is quantified by  $|g^{(1)}| = 1$ , where  $1 > |g^{(1)}| \geq 0$  is chaotic light with a finite spectral width of  $\Delta\omega$ .

A stream of photons emitted from a two-level system which is continuously excited will ideally never have two temporally overlapping photons. This phenomenon is called anti-bunching and is a purely quantum optical phenomenon with no classical counterpart. To identify such photon anti-bunching we may look to the normalised second order intensity correlation function given by:

$$g^{(2)}(t, \tau) = \frac{\langle \hat{a}^\dagger(t)\hat{a}^\dagger(t+\tau)\hat{a}(t+\tau)\hat{a}(t) \rangle}{\langle \hat{a}^\dagger(t)\hat{a}(t) \rangle^2}. \quad (2.17)$$

This describes the probability of detecting a photon at time  $t$  and  $t + \tau$ . The second order correlation function has three regimes: a) *bunched light*, where upon detecting of a photon

there is a higher probability of detecting another photon at short time scales than at long. This is called chaotic light and is often seen in thermal states. b) *coherent light*, where the photon arrival probability apply to poissonian statistics, i.e. arrive with random time intervals. c) *anti-bunched light* where photons have regular temporal gaps. Their conditions are respectively given by[42]:

$$g^{(2)}(\tau = 0) > 1, \quad (2.18a)$$

$$g^{(2)}(\tau = 0) = 1, \quad (2.18b)$$

$$g^{(2)}(\tau = 0) < 1. \quad (2.18c)$$

Anti-bunching and sub-Poissonian statistics are signatures of the quantum nature of single photons and is desired for an ideal single photon emitter i.e.  $g^{(2)}(\tau = 0) = 0$ . For a two-level system that has just emitted a photon it takes time on the order of the radiative lifetime before the two-level system can be re-excited, which means that two photon-emission events will ideally not be observed in the same time bin.

Using the quantum regression theorem it can be shown[38] that the second-order correlation operator(two-time correlation) satisfies the same equation of motion as the first order correlation function (single time correlation). Utilising this we may find an expression for the second-order correlation function from the steady-state solution of the optical Bloch equation in eq. (2.11) in the simplest limit where the Rabi frequency  $\Omega$  and the pure dephasing rate  $\gamma_{dp}$  are much smaller than the spontaneous decay rate  $\gamma$ :

$$g^{(2)}(\tau) = 1 - e^{-|\tau|\gamma/2}. \quad (2.19)$$

This gives the second order correlation for the case when the two-level system is driven with a continuous wave laser. It is clear that a suppression of coincidences at  $\tau = 0$  is present. The same suppression of the coincidences at  $\tau = 0$  is present when driving the source with a pulsed laser. Instead of having a flat correlation at  $|\tau| \gg 0$  we will now see a set of equally spaced peaks with separation  $\tau_{rep} = 1/F_{ex}$  where  $F_{ex}$  is the repetition rate of the excitation laser.

### 2.4.1.1 Experimental results of single-photon purity

The Hanbury, Brown and Twiss (HBT) experiment experimentally quantifies the second order intensity correlation function[43]. The stream of photons emitted from the single photon

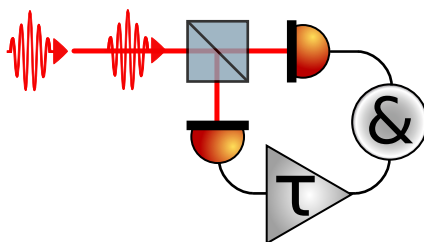


Figure 2.7: Experimental setup to perform a Hanbury Brown Twiss experiment. A stream of single photons is incident to a 50:50 BS, and the output is detected. On one arm a time delay  $\tau$  is added. Coincidences are collected at &.

source is routed through 50/50 beam splitter after which each output is detected by a single photon detector as seen in fig. 2.7. By examining the time correlation of the coincidences on the two detectors as a function of the correlation delay  $\tau$ , we obtain a correlation histogram with coincidences as a function of  $\tau$ . The quantized nature of photons forbids coincident detection events at  $\tau = 0$ , if the input is truly a stream of single photons.

The QD is excited with a pulsed excitation laser at a repetition rate of  $F_{ex} = 76.152\text{MHz}$ , such that the correlation histogram has equally spread peaks with separation  $\tau_{rep} = 1/F_{ex} \sim 13\text{ns}$ . The emission from the QD single photon source is spectrally filtered with an etalon spectral filter. For photon detection SNSPDs as described in appendix A.1 are used and the correlation histogram is generated using a *Swabian* time tagger with time bin width of 100 ps. The central slice of the  $100\mu\text{s}$  long measured correlation histogram is shown in fig. 2.8, where the suppression of the central peak, as described in section 2.4.1, is evident.

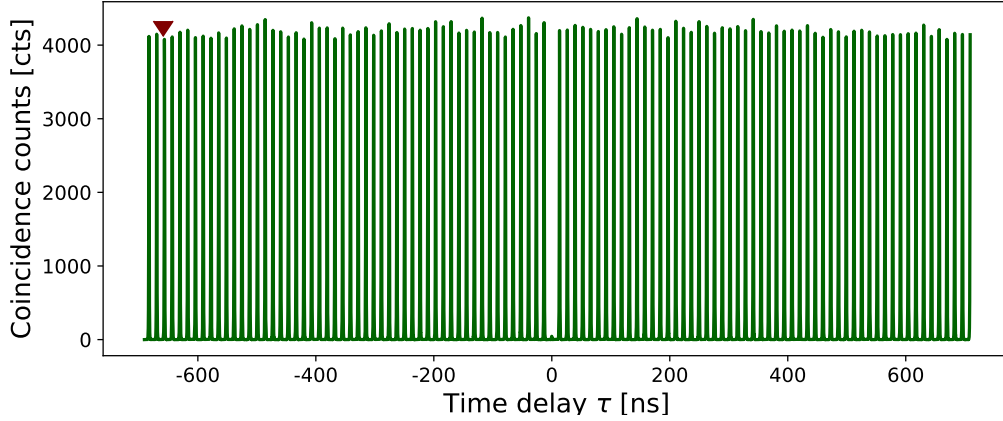


Figure 2.8: Correlation histogram recorded in the HBT experiment displayed in green. Red arrow marks the 50<sup>th</sup> side peak, used in eq. (2.21)

Each peak of the correlation histogram can be modelled as a two sided single exponential with decay  $\gamma$  of the emitter. The 5 central peaks, shown in fig. 2.9, are fitted simultaneously for fit robustness and to account for the contribution from neighbouring peaks. Hence, the fit-model is described by a summation of 5 peaks. In order to account for the instrument response the fit-model is convoluted with a Gaussian of width  $\sigma$ .

$$f(\tau, \tau_0, \gamma, \sigma) = \left( \overbrace{a_0 e^{-|\tau-\tau_0|\gamma}}^{\text{Center peak}} + \overbrace{a \sum_n e^{-|\tau-\tau_0-n\tau_{rep}|\gamma}}^{\text{Side Peaks}} + b \right) \otimes \text{IRF}(\tau, \sigma). \quad (2.20)$$

Here IRF is the *instrument response function*, i.e.  $\text{IRF}(\tau, \sigma) = e^{-\frac{1}{2}(\frac{\tau}{\sigma})^2}$ ,  $n \in \{-2, -1, 1, 2\}$  is the side peak number,  $\gamma$  is the spontaneous emission rate(decay) of the emitter and  $b$  is an offset accounting for coincidences occurring due to detector dark counts. In such way the final fit is a convolution of multiple two sided exponentials with a Gaussian function. The fitting method applied is non-linear least-squares minimisation. The second order correlation function is now found by taking the ratio of the area under the central peak with respect to a peak at large time delay ( $\tau \rightarrow \infty$ ). As the histogram has a finite time axis, it is here approximated by picking the 50th side peak (marked with a red arrow in fig. 2.8), information about which is acquired in resemblance to that of the central peak. The acquired second order correlation function is

$$g^{(2)}(0) = \frac{A(\tau = 0)}{A(\tau = 50\tau_{rep})} = (0.92 \pm 0.02)\%, \quad (2.21)$$

where  $A(\tau)$  is the area under the respective peak, found by integration of the fitted peak with an integration window of 4ns around the peak centre. The integration time window is indicated by the axis limits of the insert in fig. 2.9. The background coincidences from the  $g^2$

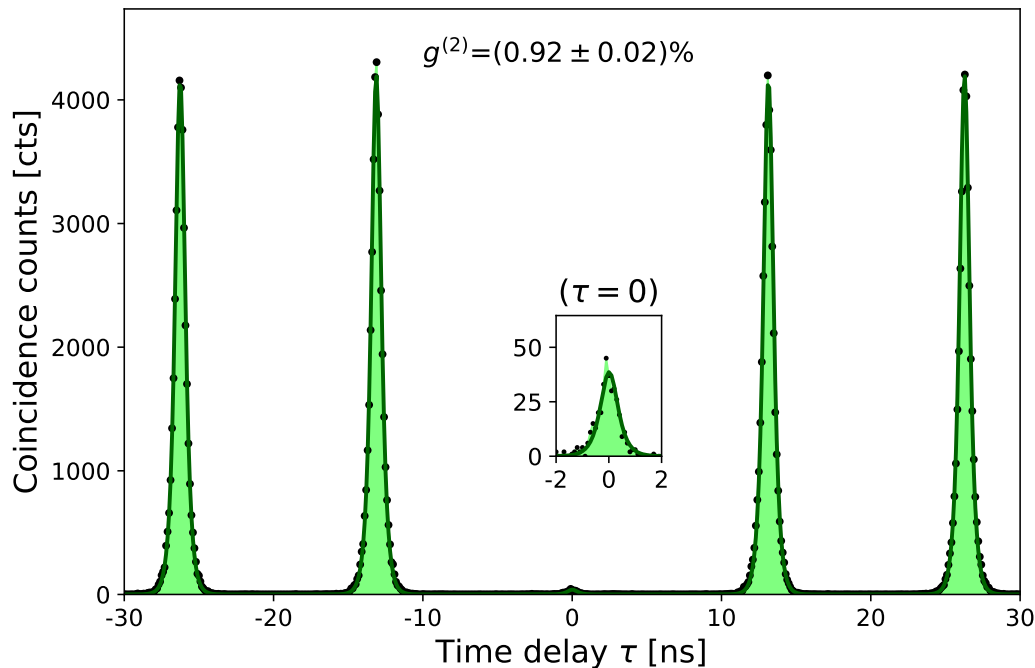


Figure 2.9: Correlation histogram recorded from the HBT experiment displayed in green dots, zoomed in to the central five peaks. All data presented are raw with no background subtracted. The fit of the data set using eq. (2.20) is shown in the green curve. The insert in the centre is a zoom of the central peak, visualising the area under curve integration window indicated by the limits of the x-axis.

estimation is accounted for by setting the background parameter to zero under integration ( $b = 0$ ).

The error estimation is based on the assumption that the coincidences apply to Poissonian statistics. As the integrals are numerical estimated the error on these are found by propagating the statistical error on the fit parameters and their correlations via the covariance matrix  $\text{cov}(x_i, x_j)$ . By sweeping over all fit parameters, the error is given by  $\sigma_f^2 = \sum_i^N \sum_j^N \frac{\partial f}{\partial x_i} \frac{\partial f}{\partial x_j} \text{cov}(x_i, x_j)$  with  $x_i, x_j \in \{\gamma, \sigma b, \tau_0\}$ . As the area under peak estimation is numerical the derivative is likewise so i.e.  $\partial f / \partial x_i \approx \Delta f / \Delta x_i$ . In the central peak the number of coincidence counts is too small for the fit to converge robustly enough to estimate error-bars. Here the error bars are estimated as the square root of the integrated coincidence counts under the peak. The final error on the normalised second order correlation function ( $\sigma_{g^{(2)}}$ ) is estimated by the means of error propagation[44]. The data analysis in this section is based on modified script developed in [38].

## 2.4.2 Photon indistinguishability

In order to implement photons in quantum information protocols, it is of utmost importance that the photons are *indistinguishable*. Indistinguishability of photons is required for any type of protocol relying on quantum interference. The indistinguishability of two photons can be evaluated by the Hong-Ou-Mandel(HOM) effect[45], which is a two photon interference phenomenon. The quantification of the photon indistinguishability of a single photon source is carried out in the HOM experiment shown in fig. 2.10a. When two indistinguishable photons are spatially and temporally superimposed on a 50:50 beam splitter(BS) with the input modes  $a_1, a_2$  and the output modes  $a_3, a_4$  as depicted in fig. 2.10b the two photons will

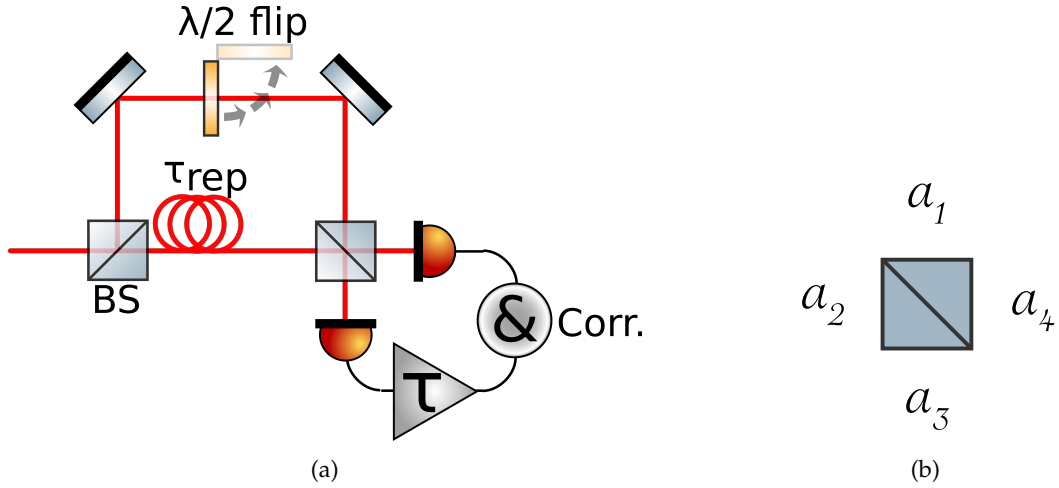


Figure 2.10: **(a)** Schematic drawing of a Hong Ou Mandel(HOM) setup. The photon stream enters the asymmetric Mach-Zehnder interferometer from the left, where it enters a beam splitter(BS) splitting the photon stream into two arms. One arm is delayed by the time between photons  $\tau_{rep}$ . Next the two arms are superimposed on the BS to the right, after which coincidences are detected in the &-correlator. A time delay  $\tau$  is added to one of the detection signals. To enable a cross- and co polarised overlap configuration on the second BS a  $\lambda/2$  plate is mounted on a flip mount on one arm. **(b)** In- and output modes of a beam splitter.  $a_1$  and  $a_2$  are input modes and  $a_3$  and  $a_4$  are output modes.

always exit in the same output mode. To understand why this is the case the propagation of the photons through a BS can be examined. The transformation matrix governing the BS in- and output relations is described by:

$$\begin{pmatrix} \hat{a}_3^\dagger(t) \\ \hat{a}_4^\dagger(t) \end{pmatrix} = \underbrace{\frac{1}{\sqrt{2}} \begin{bmatrix} 1 & i \\ i & 1 \end{bmatrix}}_{\hat{M}_{BS}} \begin{pmatrix} \hat{a}_1^\dagger(t) \\ \hat{a}_2^\dagger(t) \end{pmatrix}, \quad (2.22)$$

where a  $i = e^{i\pi/2}$  phase shift is introduced upon reflection from the BS. In this transformation matrix it is assumed that the photons are both temporally and spatially overlapped on the BS. This input-output relation results in an interference phenomenon when the state  $\hat{a}_1^\dagger(t)\hat{a}_2^\dagger(t)|0\rangle$  enters the BS:

$$\hat{a}_1^\dagger(t)\hat{a}_2^\dagger(t)|0\rangle \xrightarrow{\hat{M}_{BS}} \frac{1}{2}(\hat{a}_3^\dagger(t) + i\hat{a}_4^\dagger(t))(i\hat{a}_3^\dagger(t) + \hat{a}_4^\dagger(t))|0\rangle \quad (2.23a)$$

$$\rightarrow \frac{1}{2} \left( i\hat{a}_3^\dagger(t)\hat{a}_3^\dagger(t) + \hat{a}_3^\dagger(t)\hat{a}_4^\dagger(t) - \hat{a}_4^\dagger(t)\hat{a}_3^\dagger(t) + i\hat{a}_4^\dagger(t)\hat{a}_4^\dagger(t) \right) |0\rangle \quad (2.23b)$$

$$\rightarrow \frac{i}{2}(\hat{a}_3^\dagger(t)\hat{a}_3^\dagger(t) + \hat{a}_4^\dagger(t)\hat{a}_4^\dagger(t))|0\rangle. \quad (2.23c)$$

It is here evident that after applying the creation operators to the vacuum state only states with two photons in either output mode  $a_3$  or  $a_4$  of the BS is allowed if the input photons are identical in terms of frequency, temporal shape, polarisation, and are indistinguishable. The interference in eq. (2.23b) is based on the commutation relation  $[\hat{a}_i^\dagger, \hat{a}_j^\dagger] = 0$  with  $i, j \in \{1, 2, 3, 4\}$ , which is only satisfied for truly identical bosons [4].

The HOM measurement is carried out on an asymmetric interferometer as illustrated in fig. 2.10a. Here the single photon stream enters from the left, firstly encountering a 50 : 50 BS,

splitting the single photon stream into two arms. These two arms are next superimposed on a second BS with output modes coupled to single photon detectors, e.g. SNSPDs. One arm is delayed by  $\tau_{rep}$  (the time between two consecutive photons), to obtain temporal overlap on the second BS. To distinguish the degree of interference in the unbalanced Mach-Zehnder interferometer a half wave plate ( $\lambda/2$ ) is mounted on a flip mount, to have either co ( $\parallel$ ) or cross ( $\perp$ ) polarised photons overlapping on the BS which enable an interfering- and a non-interfering configuration, respectively. What is acquired by collecting detection coincidences over a time period is a coincidence histogram, from which we may extract the second-order cross-correlation between the two output modes  $\hat{a}_3^\dagger(t)$  and  $\hat{a}_4^\dagger(t)$ :

$$G_{3,4}^{(2)}(t, \tau) = \langle \hat{a}_3^\dagger(t) \hat{a}_4^\dagger(t + \tau) \hat{a}_4^\dagger(t + \tau) \hat{a}_3^\dagger(t) \rangle. \quad (2.24)$$

As described in section 2.4.2 the second-order correlation function can be calculated by applying the quantum regression theorem and solving the optical Bloch equations in eq. (2.10). The solution according to [46] is given by

$$G_{HOM}^{(2)}(\tau) = \frac{1}{4\gamma} e^{-\gamma|\tau|} \left( 1 - e^{-2\gamma_{dp}|\tau|} \right). \quad (2.25)$$

Here  $\gamma$  is the QD decay rate and  $\gamma_{dp}$  is the pure dephasing rate of the QD. The behaviour of the central peak is illustrated in fig. 2.11 for different  $\gamma_{dp}$  rates normalised to the spontaneous emission rate  $\gamma$ .

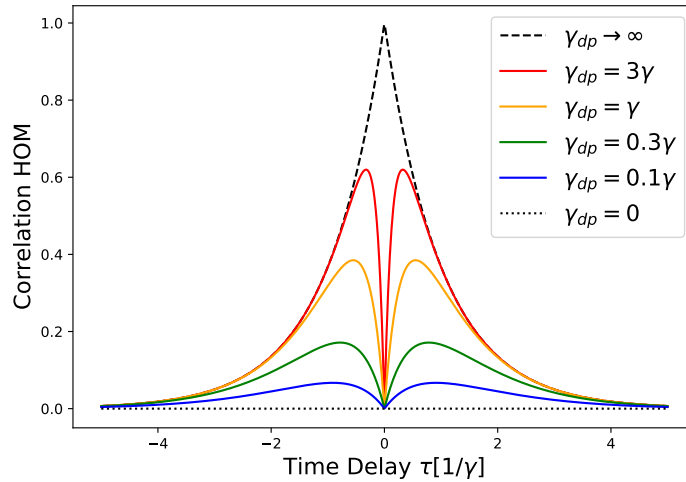


Figure 2.11: The HOM-interference peak from eq. (2.25) with pure dephasing rate  $\gamma_{dp}$  relative to the radiative decay rate  $\gamma$ . The indistinguishable case ( $\gamma_{dp} = 0$ ) shows a full suppression of coincidences and the distinguishable case ( $\gamma_{dp} \rightarrow \infty$ ) is represented with a double sided exponential.

The indistinguishability of the single photons may now be quantified by the HOM visibility given by the ratio of the area under the central peak in the co-polarised configuration and the area under the central peak in the cross-polarised configuration:

$$V_{HOM} = 1 - \frac{A_{\parallel}}{A_{\perp}} \quad (2.26)$$

### 2.4.2.1 Experimental results of photon indistinguishability

The source is operated with a pulsed excitation laser with repetition rate  $F_{ex} = 76.152\text{MHz}$  and the emitted photons from the QD are spectrally filtered and routed to the HOM setup

in fig. 2.10a. The actual implementation features a fiber BS at the second BS instead of a crystal cube as depicted in fig. 2.10a. This eases the spatial overlapping procedure of the photons significantly. The first BS is implemented as a half wave plate(HWP) followed by a polarising beam splitter(PBS) to enable power balancing of the two arms by rotating the HWP. The arm balancing is carried out by sending a polarisation stable coherent continuous wave(CW) laser through the setup and measuring one of the outputs on a photo diode. By alternately blocking one of the two arms, the two arms may be balanced by adjusting the HWP. Lastly a polarisation paddle is implemented prior to the overlapping BS, to maximise the classical interference visibility  $(1 - \varepsilon) = (I_{max} - I_{min}) / (I_{max} + I_{min})$ . This is carried out by again sending a CW laser through the setup and measuring one of the outputs on a photo diode, with the setup in the cross-polarised configuration. By minimising the interference fringes on the photo diode by adjusting the polarisation paddle, the classical interference visibility is maximised in the co-polarised configuration. The correlation histogram acquired for the co- and cross-polarisation configuration is shown in fig. 2.12, where a suppression of the central peak in the co-polarised configuration is visible. The 50% suppression of the central peak is expected for distinguishable single photons(e.g. cross-polarised), due to their anti-bunched nature.

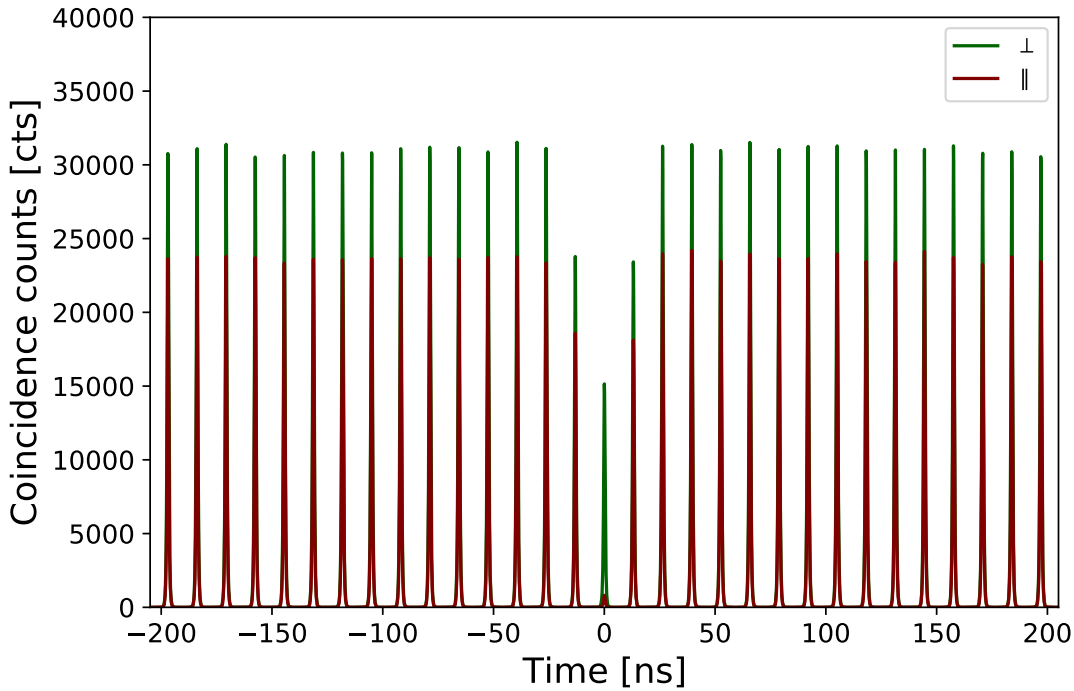


Figure 2.12: Raw time correlation histograms recorded in the HOM experiment. The green data points are coincidences recorded in the cross-configuration( $\perp$ ) and the red in the co-configuration( $\parallel$ ) of the HOM experiment setup shown in fig. 2.10a. Re-scaled to the  $\tau = 0$  value on the cross-polarised configuration.

The central 3 peaks of the two correlation histograms are respectively normalised to a peak far away( $\sim 500$ ns) from the central peak and is fitted by a function similar to that of the  $g^{(2)}$  analysis (eq. (2.20)) but with eq. (2.25) as the central peak. Again the correlation histogram is fitted with a convolution of an instrument response function(IRF). This gives

the final fit model

$$f(\tau; \tau_0, \gamma, \gamma_{dp}, \sigma) = \left( \overbrace{a_0 e^{-|\tau-\tau_0|\gamma} (1 - e^{-2|\tau-\tau_0|\gamma_{dp}})}^{\text{Center peak}} + a \sum_n \overbrace{e^{-|\tau-\tau_0-n\tau_{rep}|\gamma}}^{\text{Side Peaks}} + b \right) \otimes \text{IRF}(\tau, \sigma), \quad (2.27)$$

where IRF is the *instrument response function* i.e.  $\text{IRF}(\tau, \sigma) = e^{-\frac{1}{2}(\frac{\tau}{\sigma})^2}$ ,  $n \in \{-2, -1, 1, 2\}$  is the side peak number,  $\gamma$  is the spontaneous emission rate(decay) of the emitter,  $\gamma_{dp}$  is the pure dephasing rate and  $b$  is an offset. The normalised central peak of the co(∥)- and cross(⊥)-polarised configuration can be seen in fig. 2.13. From the fitted central peaks the raw HOM visibility is quantified by

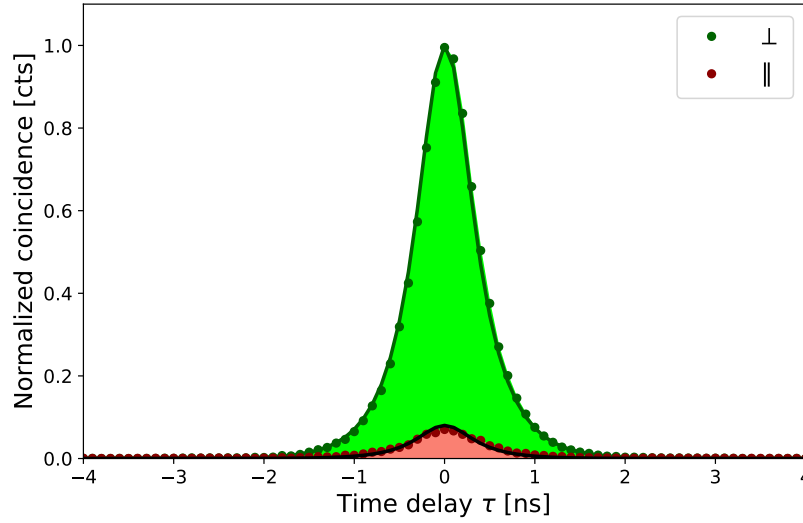


Figure 2.13: Normalised central interference peaks of the time correlation histograms presented in fig. 2.12 in the co(∥)- and cross(⊥)-configurations. The black(green) curve is a fit of the normalised coincidences in the co(cross)-polarised configuration using the fitmodel in eq. (2.27).

$$V_{raw} = \frac{A_{\perp} - A_{\parallel}}{A_{\perp}}, \quad (2.28)$$

where  $A_{\parallel}$  ( $A_{\perp}$ ) is the integral under the central peak for the co(cross)-polarised configuration estimated with an integration time window of 4ns centered around  $\tau = 0$ . This is, as noted in the subscript, however the raw (measured) HOM visibility where imperfections in the used unbalanced Mach-Zehnder interferometer of the HOM experiment is not taken into account. In the  $V_{raw}$  the BS, on which the photons are superimposed, is assumed to have 50 : 50 ( $R : T$ ) splitting ratio. The measured transmittance/reflectance values of the BS is  $R = (47.6 \pm 0.1)\%$  and  $T = (52.4 \pm 0.1)\%$ . Furthermore, the visibility is reduced due to the classical interference visibility measured to be  $(1 - \epsilon) = (99.820 \pm 0.09)\%$  of the interferometer. In order to correct for these imperfections we may look to the area under the curve value as given in the ideal scenario [47]:

$$A_{\perp, \parallel} \propto (R^3 T + R T^3) [1 + 2g^{(2)}(0)] - 2(1 - \epsilon)^2 R^2 T^2 V \quad (2.29)$$

By normalizing the raw HOM visibility with the ideal HOM visibility, we may arrive at the corrected intrinsic HOM visibility[48]

$$V_{intrinsic} = \frac{V_{Raw}}{V_{Ideal}} \quad (2.30)$$



This definition of the intrinsic HOM visibility also corrects for any presence of laser background photons (weak coherent states), i.e. imperfect single photon purity  $g^{(2)}(\tau = 0) \neq 0$ . This impurity will, however, still be present in the photon stream, when used for any quantum applications such as the heralded entanglement gate described in chapter 4. Thus, correction is only relevant with respect to the imperfections of the unbalanced Mach-Zehnder interferometer and we arrive at the following expression for the corrected HOM visibility as it is experienced by any subsequent setup:

$$V_{HOM} = \frac{(R^2 + T^2)}{2RT(1 - \epsilon)^2} V_{raw}. \quad (2.31)$$

The HOM visibility extracted from the correlation histograms is

$$V_{HOM} = (92.8 \pm 0.3)\%. \quad (2.32)$$

Here the error is estimated in accordance with the error estimation of section 2.4.1.1

## 2.5 Summary

An InAs/GaAs QD embedded in a photonic nanostructure emitting single photons of wavelength  $\lambda = 942.0\text{nm}$  is described in this chapter and the goodness of the QD single photon source is characterised. The QD excitation rate of  $F_{ex} = 76.152\text{MHz}$  combined with an estimated source efficiency of  $\eta_S \approx 6.1\%$  results in an expected single photon rate of  $F_{SP} = 4.6\text{MHz}$ . The single photon rate was measured to  $3.8\text{MHz}$  corresponding to a  $5.0\%$  source efficiency. The experimentally achieved single photon purity of the QD single photon source is  $g^{(2)}(\tau = 0) = (0.92 \pm 0.02)\%$  and with a photon indistinguishability of  $V_{HOM} = (92.8 \pm 0.3)\%$ .

---

## Chapter 3

# Temporal-to-spatial mode conversion

---

For many quantum information protocols a set of  $M$  spatially separated modes with identical and indistinguishable photons are required. The single photon source presented in chapter 2 emits single photons in a fixed spatial mode in different temporal modes. With the intent of obtaining a spatially separated multi-photon source we may introduce temporal-to-spatial mode conversion, also known as *demultiplexing*. This chapter will introduce a demultiplexing scheme for converting a single photon source emitting a stream of single photons into a spatial four-mode source.

### 3.1 Demultiplexing

The role of the demultiplexer is to convert a string of spatially overlapped photons with temporal separation into being spatially separated and temporally overlapped. The demultiplexer can be configured to split the incoming single photon stream into a desired number of spatial modes, depending on the demultiplexer setup configuration. In this work the desired number of spatial modes is  $M = 4$ , corresponding to the number of input modes in the entanglement gate discussed in chapter 4. The demultiplexer is schematically presented for  $M = 4$  in fig. 3.1a.

Optical demultiplexing can be carried out either by probabilistic (passive) or deterministic (active) means. A *passive demultiplexer* is constructed by probabilistic optical elements that applies the same transformation to all photons, such as 50/50 beam splitters in a tree like structure. This protocol will work for  $M = 2^n$ -fold demultiplexing. Due to the probabilistic nature of this scheme the efficiency, i.e. probability of achieving 1 photon in each of the  $M$  spatial modes at time  $t$  is  $\eta_{passive,M} = (1/M)^M$ , which for  $\eta_{passive,4} = 3.9\%$ . If we want to address separate temporal modes individually we need a component with a controllable time-dependence, i. e. an active component. By instead switching the photons *actively* into the separated spatial modes, the demultiplexing efficiency is given by  $\eta_{active} = 1/\eta_{sw}^M$ , where  $\eta_{sw}$  is the switching efficiency of each active optical switch. With switching efficiencies close to unity, this proves to be the viable solution.

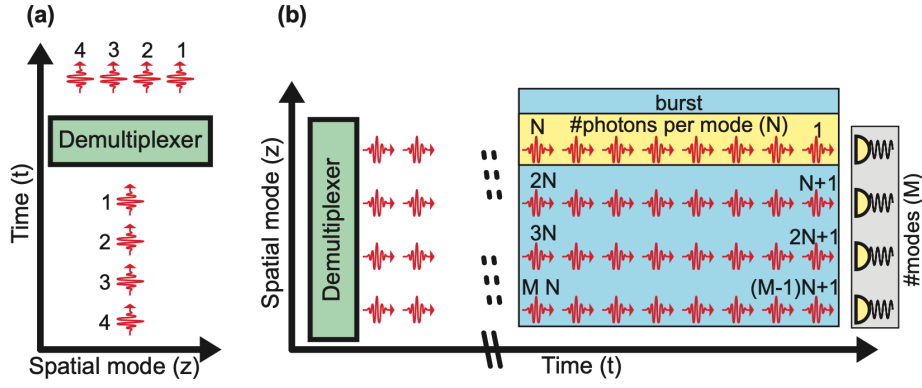


Figure 3.1: Schematic of the temporal-to-spatial demultiplexer operation with (a) the ideal scenario where every individual photon (red wiggles) is switched to a different spatial mode and (b) the realistic scenario where the switching rate is limited and multiple photons per mode are switched. Reprinted from [49].

## 3.2 Active demultiplexing

Where passive demultiplexing is based on consecutive beam splitters, the active demultiplexing setup is based on consecutive active switches. An active optical switch can be realised by combining two optical components in the following order: A polarisation modulator and a polarising beam splitter (PBS). This type of optical switch requires a polarisation stable source.

### 3.2.1 Polarisation modulators

The polarisation modulators in the optical switching elements are in our setup implemented using electric optical modulators (EOMs). These utilise the *electro optic effect* describing the creation and control of a material's optical properties by the application of an electric field. This effect can be utilised to change a material's absorption and/or birefringence. The latter of the two effects can be used to realise a voltage controlled wave plate by the linear electro-optic effect also known as *Pockel's electro optic effect* [50]. The Pockels effect describes the linear response of a material's refractive indices in two orthogonal spatial dimensions, orthogonal to the electric field. When an electric field ( $\mathcal{E}$ ) is applied in the  $z$  direction the refractive indices of the crystal is altered according to

$$n_x = n_0 + \frac{1}{2}\mathcal{N}\mathcal{E}, \quad n_y = n_0 - \frac{1}{2}\mathcal{N}\mathcal{E}, \quad (3.1)$$

where  $\mathcal{N}$  is a material specific constant quantifying the linear dependency of the Pockel cells refractive index, at the optical frequency  $\omega$  of interest, when an electric field ( $\mathcal{E}$ ) is applied.  $n_0$  is the refractive index at this frequency ( $\omega$ ) in absence of an applied electric field, such that when no voltage is applied the crystal is non-birefringent and will only alter the overall phase of the transmitted light. Vice versa, when a voltage is applied the transmitted light will experience voltage dependent birefringence.

The EOMs used in the demultiplexer setup are *Eksma Optics Ultrafast Pulse Pickers* made from a 5 mm diameter KTP-crystal. By tuning the bias voltage across the crystal these EOM's can operate as half wave plates (HWP). The HWP operational voltages for light at wavelength  $\lambda = 942\text{nm}$  were found to be in the range  $(2.5 \pm 0.1)\text{kV}$ . Using the EOMs as active switches, the bias voltage is applied in pulses. The maximal switching rate of the Eksma EOMs is  $F_{max} \simeq 1.0\text{MHz}$  with a maximum duty cycle of  $\sim 28\%$ .

### 3.3 Scheme and operation

The active demultiplexer implemented in this work functions by cascading a set of EOMs described in previous section (section 3.2.1). Each EOM is followed by a PBS, such that the number of spatial output modes is  $M = (N_{EOM} + 1)$ , with  $N$  being the number of cascaded EOMs. With the incident light being vertically polarised, the light is transmitted on the PBS when a bias voltage is applied across the EOM, and reflected in absence of a bias voltage. For switching a stream of single photons into 4 modes three switches are needed, such that one optical path is un-switched, while the other three are actively switched into. The experimental implementation is shown in fig. 3.2, where EOM1-3 are the optical switches and  $M_{1-4}$  are the four spatial output modes.

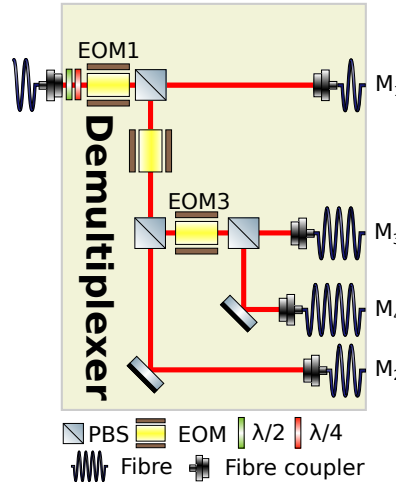


Figure 3.2: Schematic of the demultiplexer setup. The fibre coupler in the upper left corner is connected to a single photon source. The stream of single photons arriving from the single photon source is switched into the four spatial modes  $M_1$ ,  $M_2$ ,  $M_3$  and  $M_4$ . The demultiplexer setup is included in the full experimental setup presented in fig. 4.8.

The timing of the three EOMs is controlled by a field programmable gate array (FPGA) programmed with a phase locked loop (PLL). This FPGA has four output trigger signals which are all phase locked to one of the FPGA input ports that receives a trigger signal from the single photon source excitation laser working as a master clock. In this way the demultiplexer and single photon source may be synchronised. The master clock pulse is down sampled by  $M \cdot N$ , where  $N$  is the number of photons per burst as described in next section (section 3.3.1), in order to encapsulate the full demultiplexed photon train. Two of the FPGA outputs are added a  $\pi/2$  and  $\pi$  phase-shift respectively, such that the three outputs coupled to the EOMs are  $\pi/2$  out of phase. The timing electronics are included in the schematic of the experimental setup including source, demultiplexer and entanglement gate in fig. 4.8.

The incoming single photons are vertically polarised and hence reflected on all PBSs. This will send the un-switched photon burst (first  $N$  photons) to  $M_4$ . The *first* FPGA output will then trigger the EOM3 to work as a HWP rotating the photon polarisation by  $90^\circ$ , which will transmit through the following PBS and be routed to  $M_3$ .  $\pi/2$  out of phase with the first FPGA output, the *second* output triggers EOM2 routing the third burst to  $M_2$  and lastly  $\pi$  out of phase with the first FPGA output the *third* output triggers EOM1 to route the last photon burst to  $M_1$ . This process is cyclic with the frequency  $F_{sw} = F_{source}/(M \cdot N)$ . The *fourth* FPGA output is used as a detection reference clock in phase with the master clock.

### 3.3.1 Experimental limitations

Ideally the demultiplexer switches one photon into each spatially separated output mode as visualised in fig. 3.1a, such that the switching rate is  $F_{sw} = F_{sp}/M$ . Due to hardware limitations, more specifically the maximal repetition rate of the EOMs ( $F_{max}$ ), the realisable setup switches a finite train of photons into each spatial mode per switching event called a *photon burst*, as illustrated in fig. 3.1b. Hence, the switching rate of each EOM is given by

$$F_{sw} = \frac{F_{rep}}{N \cdot M} \leq F_{max}. \quad (3.2)$$

Here  $M$  is the number of spatial separated modes and  $N$  is the number of photons pr. burst. This result in a minimum photon burst size of

$$N = \left\lfloor \frac{F_{sp}}{F_{max} \cdot M} \right\rfloor \quad (3.3)$$

where  $\lfloor \rfloor$  implies rounding down to nearest integer. The experimental setup for the demultiplexer is limited as described in section 3.2.1 by a maximal switching rate of  $F_{max} \simeq 1.0$  MHz. The excitation rate of the QD single-photon source as given in chapter 2 is  $F_{ex} = 76.152$  MHz; hence, assuming a perfect single photon source, the time difference between two consecutive single photons entering the demultiplexer is  $\Delta t = 1/F_{sp} = 13.132$  ns. The number of photons per burst satisfying eq. (3.3) is  $N = 20$  and the switching rate of the demultiplexer is then (cf. eq. (3.2))  $F_{sw} = 952$  kHz. The EOMs operate with a duty cycle of 27.5% for accommodating the rise and fall time of 6.6 ns. This is just below the operational limitations for the Pulse pickers at  $\sim 28\%$ .

The demultiplexer setup has a finite transmission that is dependent on: **1** the the optical fibre efficiency of the 30 meter fibre transporting the photons from the source to the demultiplexer and its coupling efficiency. The measured efficiency is  $\eta_{fiber} = (92 \pm 2)\%$ . **2** The collection ports of the four output modes of the demultiplexer, including the respective delay fibres, which has collection efficiency  $\eta_m$  measured to be  $\eta_1 = (89.8 \pm 1.0)\%$ ,  $\eta_2 = (87.4 \pm 1.2)\%$ ,  $\eta_3 = (86.5 \pm 1.1)\%$  and  $\eta_4 = (84.1 \pm 1.1)\%$ . **3** The setup dedicated single photon detectors, i.e. SNSPDs, efficiency that is the combination of the specified detector efficiency  $> 95\%$ , the connection between the fibre and the detector, that is made with a splice with an estimated efficiency of  $\sim 98\%$ , and the transmission of the fibre itself  $\sim 94\%$ [49]. This results in a total detection efficiency of  $\eta_{det} = (88 \pm 1)\%$ . **4** The end-to-end efficiency of the optical elements in the optical path from input to output. The lowest end-to-end efficiency is measured from input to  $M_4$  at  $\eta_{optics} = (78.3 \pm 2.0)\%$  working as a lower threshold for the four switching paths. This path includes the HWP and QWP for polarisation control, three EOMs, three PBSs and five alignment mirrors(not visualised in fig. 3.2). The demultiplexer transmission efficiencies are summarised in table 3.1.

Component	Efficiency
Collection( $\eta_m$ )	$\eta_1 = (89.8 \pm 1.0)\%$
	$\eta_2 = (87.4 \pm 1.2)\%$
	$\eta_3 = (86.5 \pm 1.1)\%$
	$\eta_4 = (84.1 \pm 1.1)\%$
Optics end-to-end	$\eta_{optics} \geq (78.3 \pm 2.0)\%$
Detection	$\eta_{det} = (88 \pm 1)\%$
Photon transport	$\eta_{fiber} = (92 \pm 2)\%$

Table 3.1: Efficiencies of the Demultiplexer setup.

### 3.3.2 Switching efficiency and alignment

Each of the switching elements in the demultiplexer consists of an EOM followed by a PBS. The switching efficiency  $\eta_{sw}$  is defined as the accumulated switching efficiency of the two optical elements such that  $\eta_{sw} = \eta_{pbs}\eta_{EOM}$ . Here the switching efficiency of the EOMs is given by the optical transmission of the Pockels cell ( $T_{EOM}$ ) and an extinction parameter ( $r_{ext}$ ) i.e. how many photons experiences a  $\lambda/2$  effect in the EOM whilst an electric field is applied across the Pockels cell compared to when no electric field is applied.

The alignment of the input field path through the Pockels cells of the EOM is done in two steps in accordance with [51]: **Firstly** a rough alignment is performed by observing the Pockels cell's isogyre pattern visible when shining diffused laser light through the crystal. Whilst doing so the pulse picker is off. When observing this pattern, we align the input laser field to be centred in the isogyre pattern, and ensure that the isogyre pattern is as symmetric as possible. The Pockels cell of each EOM have 3 control knobs for adjusting spatial translation and angle with respect to the incident optical field, that we utilise to optimise the light beams interaction with the crystal. **Secondly** the pulse picker is turned on. While the EOM is active, we observe the transmitted (or reflected) light on a photo diode connected to an oscilloscope. Here the ratio between the transmitted (or reflected) signals high and low is optimised using the Pockels cell's control knobs in order to obtain the best possible extinction.

This extinction ratio is finally characterised by passing an attenuated vertically polarised pulsed Mira 900 (Coherent) laser in phase with the pulse picker of the EOMs through all three EOMs. Output  $M_4$  (in fig. 3.2) is then connected to a SNSPD and detection time stamps collected using a *quTAU* time tagger. The signal when no EOM is active is seen in fig. 3.3a. Here both detector saturation and data aliasing is visible. The detector saturation arises from an intrinsic detector dead-time, that can be overcome by simply attenuating the incident light field. The aliasing is compensated for by binning the collection rates into 80 time bins corresponding to the 80 photons of the switched photon train. When activating one EOM at a time, we observe how 20 pulses is actively switched out as seen in figs. 3.3b to 3.3d. The extinction is now quantified by

$$r_{ext} = \frac{C_{on} - C_0}{C_{off} - C_0}, \quad (3.4)$$

with  $C_{on/off}$  being the count rate per second ([cts/s]) when the respective EOM is turned on/off and  $C_0$  is the dark counts of the SNSPDs i.e. the count rate when the laser is blocked. The EOM efficiency is then given by  $\eta_{EOM} = (1 - r_{ext})T_{EOM}$ . Both EOM extinction ratios and efficiencies is presented in table 3.2. The PBS efficiency is similarly given by the optical

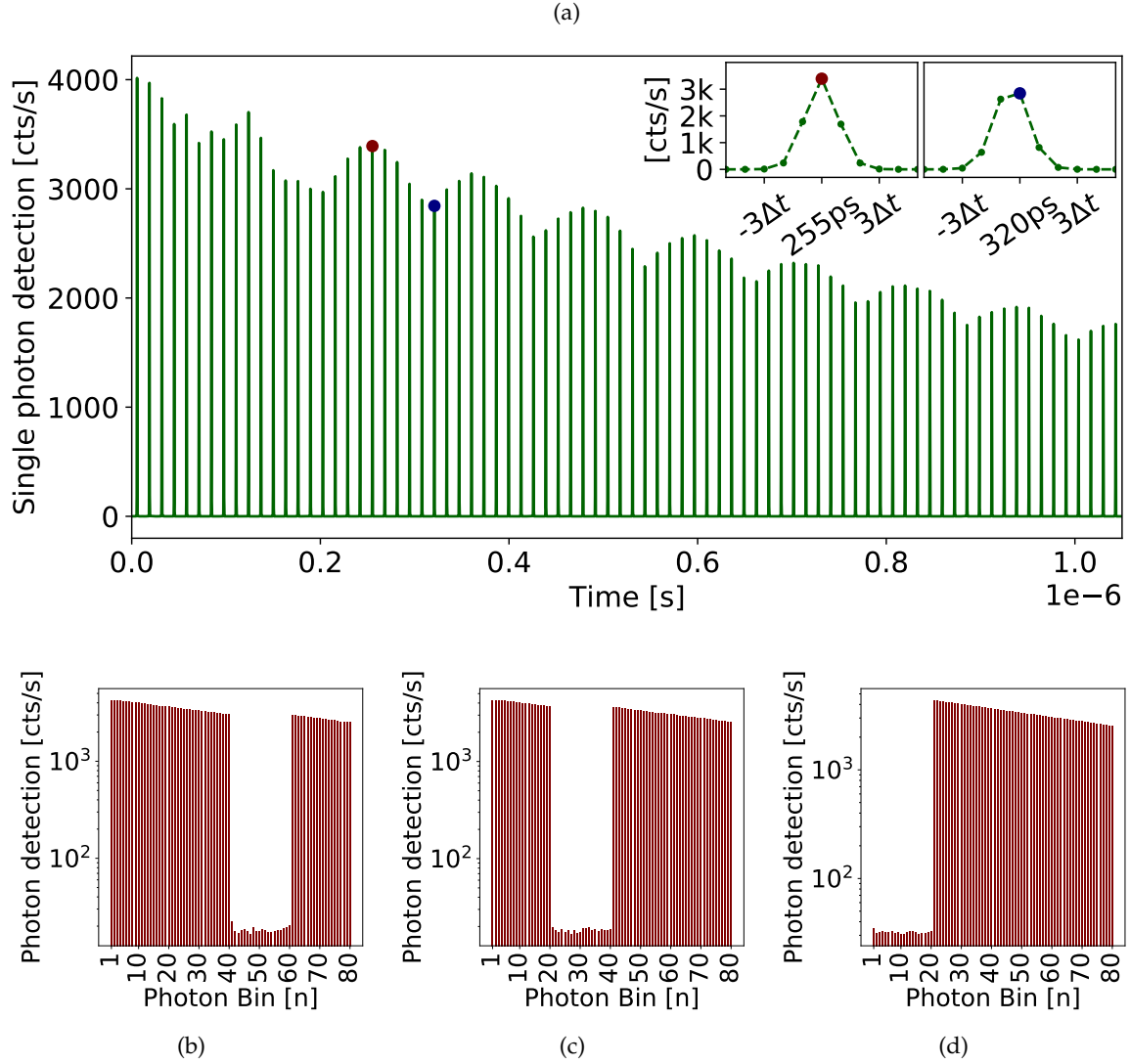


Figure 3.3: **(a)** Histograms of arrival times of photons, with respect to a trigger of period  $T_{trigger} = 80/F_{rr} = 1.05\mu s$ , with all EOMs inactive. Oscillations are due to aliasing as seen in the two inserted plots, where the red dot corresponds to the red dot on the main plot and the blue dots likewise so. This is corrected for by binning the arrival histogram into 80 separate bins corresponding to the photon arrival bins. The decay component arises due to detector oversaturation. **(b)** Binned histogram of photon arrival times with EOM1 active. **(c)** Binned histogram of photon arrival times with EOM2 active. **(d)** Binned histogram of photon arrival times with EOM3 active. Note that (b), (c) and (d) are plotted on a logarithmic detection scale.

transmission and extinction ratio. The PBS transmission efficiency is  $T_{PBS} > 98.0\%$  with an extinction ratio  $< 1 : 1000$  and the reflection efficiency is  $R_{PBS} > 99.5\%$  with extinction ratio  $\sim 1 : 100$  [52]. Using the transmitted efficiency as a lower bound leads to the total switching efficiencies  $\eta_{sw}$  presented in table 3.2

	EOM1	EOM2	EOM3
High voltage	2.51kV	2.53kV	2.47kV
Extinction ( $r_{ext}$ )	1 : (164 ± 12)	1 : (201 ± 8)	1 : (136 ± 4)
$T_{EOM}$	99.45%	99.52%	99.3%
$\eta_{EOM}$	98.9%	99.0%	98.6
$\eta_{sw}$	96.8%	96.9%	96.5%

Table 3.2: Characterised extinction ratio according eq. (3.4) and optical transmission  $T_{EOM}$  efficiency of the EOM at wavelength  $\lambda = 930\text{nm}$  as specified by the manufacturer (*Eksma Optics*) combined in a total EOM efficiency  $\eta_{EOM}$ . Including PBS efficiency and extinction ratio this results in a total switching efficiency  $\eta_{sw}$ . "High voltage" is the pulse picker operational voltage at which, the optimised extinction is reached.

### 3.4 Timing

For quantum information processing applications the timing of the photons is crucial. For interference in quantum gates photons must be spatially as well as temporally overlapped. For temporal alignment a delay fibre is added to output  $M_{2,3,4}$  such that

$$L_m = L_1 + (m - 1) \frac{c \cdot \Delta\tau}{n_{fibre}} \quad (3.5)$$

Where  $L_m$  is the fibre length at output mode  $M_m$  for  $m \in \{1, 2, 3, 4\}$ ,  $c$  is the speed of light in vacuum,  $n_{fibre}$  is the refractive index of the fibre for light @  $\lambda = 942$  and  $\Delta\tau$  is the time between two consecutive photon bursts i.e.  $\Delta\tau = N/F_{source}$ . Adding this delay should ensure temporal overlap of the four output modes. On collection port  $M_{2,3,4}$  an additional free space delay line is implemented in order to fine tune the time-matching.

In order to characterise the temporal overlap of the output modes, the four output fibres are connected, one at a time, to a low timing-jitter APD as described in appendix A.1 with timestamps collected by a high resolution timetagger with a minimum binwidth of 4ps. Whilst doing so the demultiplexer is active and an attenuated pulsed Mira laser at rate  $F_{rr} = 76.152\text{MHz}$  is transmitted through the demultiplexer. From this we acquire a histogram of the photon arrival time with respect to the laser trigger. In fig. 3.4 inserted plot the 20 pulses of one burst is shown. The main plot in fig. 3.4 shows the photon arrival histogram in the first pulse of the burst of each of the four demultiplexer output modes i.e. the shaded green area in the insert.

As the photon arrival histogram in fig. 3.4 can be considered a probability density function (PDF), we may estimate the overlap using hypothesis testing tools such as the Kolomorgov-Smirnoff test and the two sample test[44]. Using the Python `scipy.stats`[53] toolbox, the statistics of the two test are evaluated and shown in table 3.3. These two hypothesis testing tools yield a  $p$ -value of unity for all overlaps. To provide a more nuanced overlap quantity the reduced chi square between the photon arrival histograms has also been calculated according to

$$\chi_\nu^2 = \frac{1}{\nu} \sum_i^N \left[ \frac{X_i - Y_i}{\sqrt{\sigma_{X_I}^2 + \sigma_{Y_I}^2}} \right]^2, \quad (3.6)$$



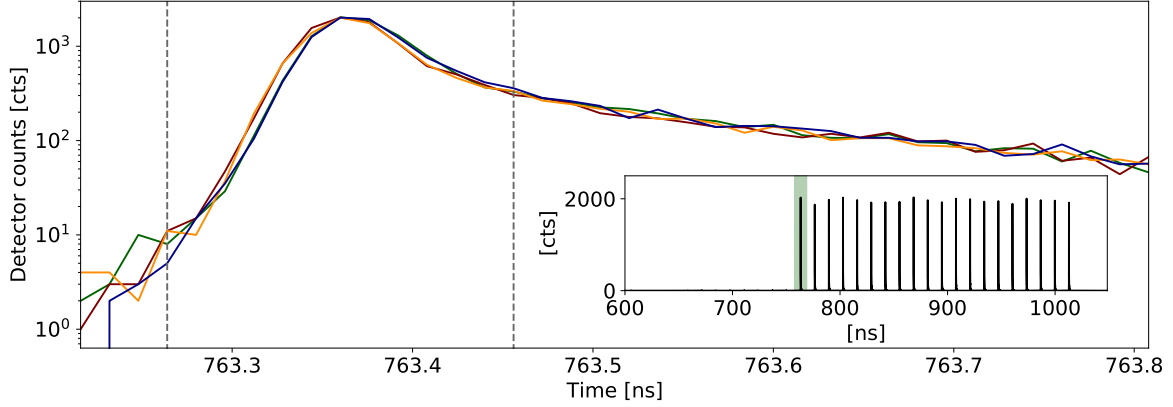


Figure 3.4: Photon arrival histogram in the first photon bin of the photon burst shown in the insert. The green shaded region in the insert corresponds to the time-window of the main figure. The photon arrival time of spatial outputmode  $M_1$  is shown in green, in red  $M_2$ , in orange  $M_3$  and in blue  $M_4$  in accordance with fig. 3.2.

where  $\nu$  is the number of included points in the comparison (degrees of freedom),  $N$  the number of data points of each peak evaluated,  $X_i$  and  $Y_i$  are the normalised data points of the two histograms in time wise consecutive order and the error on each data point is estimated by  $\sigma_{X_i} = \sqrt{X_i}$  and  $\sigma_{Y_i} = \sqrt{Y_i}$ . The reduced chi square is also presented in table 3.3. All the hypothesis testing is done within a time window of 192ps shown in the grey dotted lines in fig. 3.4, in order to ignore most detector dependent noise effects e.g after pulsing.

Overlap	$M_1$			$M_2$			$M_3$		
	$\chi_\nu^2$	t-test	KS	$\chi_\nu^2$	t-test	KS	$\chi_\nu^2$	t-test	KS
$M_2$	5.60	0.0	0.0833						
$M_3$	4.53	0.0	0.0833	0.555	0.0	0.0833			
$M_4$	0.424	$-3.83 \cdot 10^{-16}$	0.167	5.40	$3.85 \cdot 10^{-16}$	0.0833	4.73	$3.90 \cdot 10^{-16}$	0.0833

Table 3.3: Pair wise overlap test between photon arrival histograms displayed in fig. 3.4.  $\chi_\nu^2$  is the chi square reduced value (eq. (3.6)) of the two photon arrival histograms, t-test is the two sample test statistics and KS is Kolomorgov-Smirnoff test statistics.

### 3.5 Four-fold rates

The desired outcome of the demultiplexer is four simultaneous and indistinguishable photons, one in each of the output modes. The rate of such a four fold coincidence event is dependent on two things: **1** The overall efficiency of the demultiplexer setup and **2** the rate and efficiency of the source. The general  $M$ -fold measured coincidence rate for a demultiplexer is given by [49]

$$F_{MF} = \frac{F_{rep}}{M \cdot N} \sum_{n=1}^N \prod_{m=1}^i \rho_i^n. \quad (3.7)$$

Here  $F_{rep}$  is the rate at which the source is excited,  $M$  the number of spatially separated output modes,  $N$  the number of photons per burst and  $\rho_i^n$  is the probability of measuring a photon in the  $i^{\text{th}}$  output mode in the  $n^{\text{th}}$  photon bin of the burst. The first three parameters ( $F_{rep}$ ,  $M$ ,  $N$ )

are specified by the rate of the QD excitation laser as given in section 2.3 and the experimental limitations in section 3.3.1. The probability of measuring a photon in the  $i^{\text{th}}$  output mode in the  $n^{\text{th}}$  photon bin is given by

$$\rho_i^n = \eta_i \sum_{k=0}^{n-1} \left[ \prod_{\epsilon=k+1}^{n-1} (1 - \rho_i^\epsilon) \rho_i^k T_i^{n,k} \right]. \quad (3.8)$$

Here the end-to-end efficiency of each of the demultiplexer output modes is given by:  $\eta_i = \eta_S \eta_{fibre} \eta_m \eta_{sw} \eta_{det}$ , where  $\eta_S$  is the source efficiency presented in section 2.3,  $\eta_{fibre}$  is the efficiency of the fibre transporting the single photons from the source to the demultiplexer as characterised in section 3.3.1,  $\eta_m$  with  $m \in \{1, 2, 3, 4\}$  is the coupling efficiency of each of the demultiplexer output modes including delay fibre propagation losses as characterised in section 3.3.1,  $\eta_{sw}$  is the efficiency of the three optical switches in the demultiplexer as characterised in section 3.3.2 and  $\eta_{det}$  is the detector efficiency as estimated in section 3.3.1.  $T_m^{n,k}$  is the time response function of the detectors, which occurs due a dead time limitation of the detectors used. Upon detection the SNSPDs will have a dead time where no detection is possible given by  $T_m^{n,k} = 1 - \exp\left\{-\frac{n-k}{\tau_{norm}}\right\}$ , where  $\tau_{norm} = \frac{\tau_{dead} F_{rep}}{-\ln(0.05)}$  is the normalised dead time[49]. The detector deadtime ( $\tau_{dead} = 70\text{ps}$ ) is presented in appendix A.1. Furthermore we have for the first photon of each burst that  $T_m^{n,k=0} = 1$  indicating that the first photon of a burst(no matter in which time bin this occurs) does not suffer from the detector time response, as the detector dead time is much smaller than the time between two consecutive bursts ( $\Delta t_{burst} \simeq 1.05\text{ns}$ ). The expected measured four fold coincidence rate cf. eq. (3.7) with

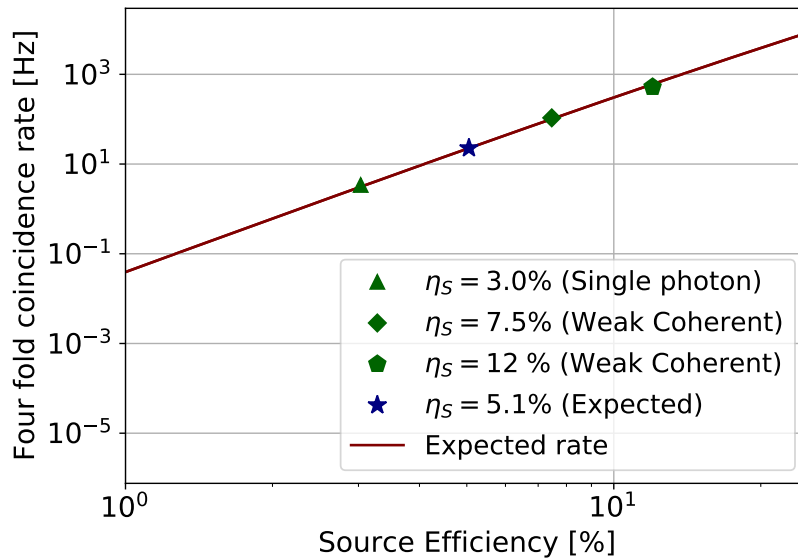


Figure 3.5: Four-fold coincidence rates(FFCR) calculated from eq. (3.7) shown in red with respect to the efficiency of a QD single photon source excited at a rate of  $F_{ex} = 76.152\text{Hz}$  as introduced in chapter 2. The Star marks the calculated FFCR rate of 23Hz for the achieved source efficiency discussed in section 2.3 of  $\eta_S = 5.0\%$ . The triangle marks a measured FFCR of 3.406Hz with the QD single photon source optimised to  $\eta_S = 3.0\%$  efficiency. The square(pentagon) marks a measured FFCR of 521.3Hz(34.64Hz) with a weak coherent state source corresponding to  $\eta_S = 12\%$ ( $\eta_S = 7.5\%$ ) QD single photon source efficiency.

respect to the source efficiency is shown in a red curve in fig. 3.5. Here the blue star indicates the expected count rate of 23Hz for the obtained source efficiency of  $\eta_S = 5.0\%$  presented in

section 2.3. In green polygons experimentally obtained values are shown. The single photon source four-fold coincidence rate(triangle) is experimentally acquired by operating the single photon source at an excitation rate of  $F_{ex} = 76.152\text{MHz}$ , optimised to a single photon rate of  $2.3 \cdot 10^6$  counts per second corresponding to a source efficiency of 3.0%. Simultaneously the demultiplexer is active and the photons are routed through the setup, while the four output modes are coupled to four different SNSPD detector channels. The detection time stamps are collected by a time tagger with 81ps resolution [54], down sampled and logged by a MATLAB script. The down sampling factor is 6 resulting in a time bin width of  $6 \times 81\text{ps} = 486\text{ps}$  for mere storage concerns over longer integration time, while still maintaining a sufficient time resolution i.e much smaller than the time between two consecutive excitation pulses. The acquired time stamps of the four output modes are next intersected within a time window of three timebins(1.458ns) to check for four fold coincidences. This procedure was also carried out with a weak coherent laser at two different count rates of 5.23MHz and 8.41MHz corresponding to a 7.4% and 12% source efficiency respectively. The measured four-fold coincidence rates with a weak coherent source are shown in fig. 3.5 as a square and a pentagon.

### 3.6 Demultiplexed photon indistinguishability

For the demultiplexed source to be used as a  $M$ -photon source in any quantum information processing protocol, the photons must be indistinguishable across the  $M$  output modes. The output photons of the demultiplexer output modes all originate from the same single photon source. These have been separated into  $M$  sections and each output delayed to make all  $M$  photon burst modes overlap in time. This entails that the temporally overlapped photons of the demultiplexer output modes are emitted by the same single photon source, but at different times with a time separation given by  $\Delta t_{i,j} = (i - j) \cdot N / F_{rep}$ , where  $j, i \in \{1, 2, 3, 4\}$  are the demultiplexer output mode number arranged from the shortest delay line to the longest. The largest time difference between the emission event of any two concurrent output photons of the demultiplexer is hence given by  $\Delta t_{1,4} = \frac{(4-1) \cdot N}{F_{rep}} = 789.0\text{ns}$ . A drop in indistinguishability on these timescales has been observed on quantum dot single-photon sources[55, 56]. The drop in indistinguishability is expected to be owed to pure dephasing. In resemblance, on a QD in a sample similar to the one of this work the indistinguishability have been observed to be unchanged at timescales up to 785.7ns [38].

Following the experimental procedure of section 2.4.2 we characterise the photon indistinguishability of the photons across the four output modes. To do so output  $M_1$  (the first  $N$  photons of the switched photon train) is superimposed with output  $M_2$ ,  $M_3$  and  $M_4$  respectively on a beam splitter(BS), which together with the demultiplexer assemble an unbalanced Mach-Zehnder interferometer executing a time correlation measurement with the outputs at co and cross polarised configurations(A half wave plate has been installed at output  $M_1$  to enable these two configurations). The correlation histogram measured on output  $M_1$  and  $M_2$  is visualised in fig. 3.6a.

The triangular shape arises due to the fact that the photons arrive in trains of 20 (per burst) and thus gives the shape of two convoluted of squares. For the co-polarised configuration ( $\parallel$ ) the central peak is suppressed due to photon interference as described in section 2.4.2 and similarly to section 2.4.2 we observe a  $\sim 50\%$  suppression of the central peak in the cross polarised configuration. The central coincidence peaks are normalised with respect to central peaks of the sideburst shown in fig. 3.6b in the co- and cross-polarised configuration, respectively. The HOM visibility is found by fitting the normalised central peaks in figs. 3.6c to 3.6e in the two configurations( $\perp, \parallel$ ) in accordance with section 2.4.2 and integrating the

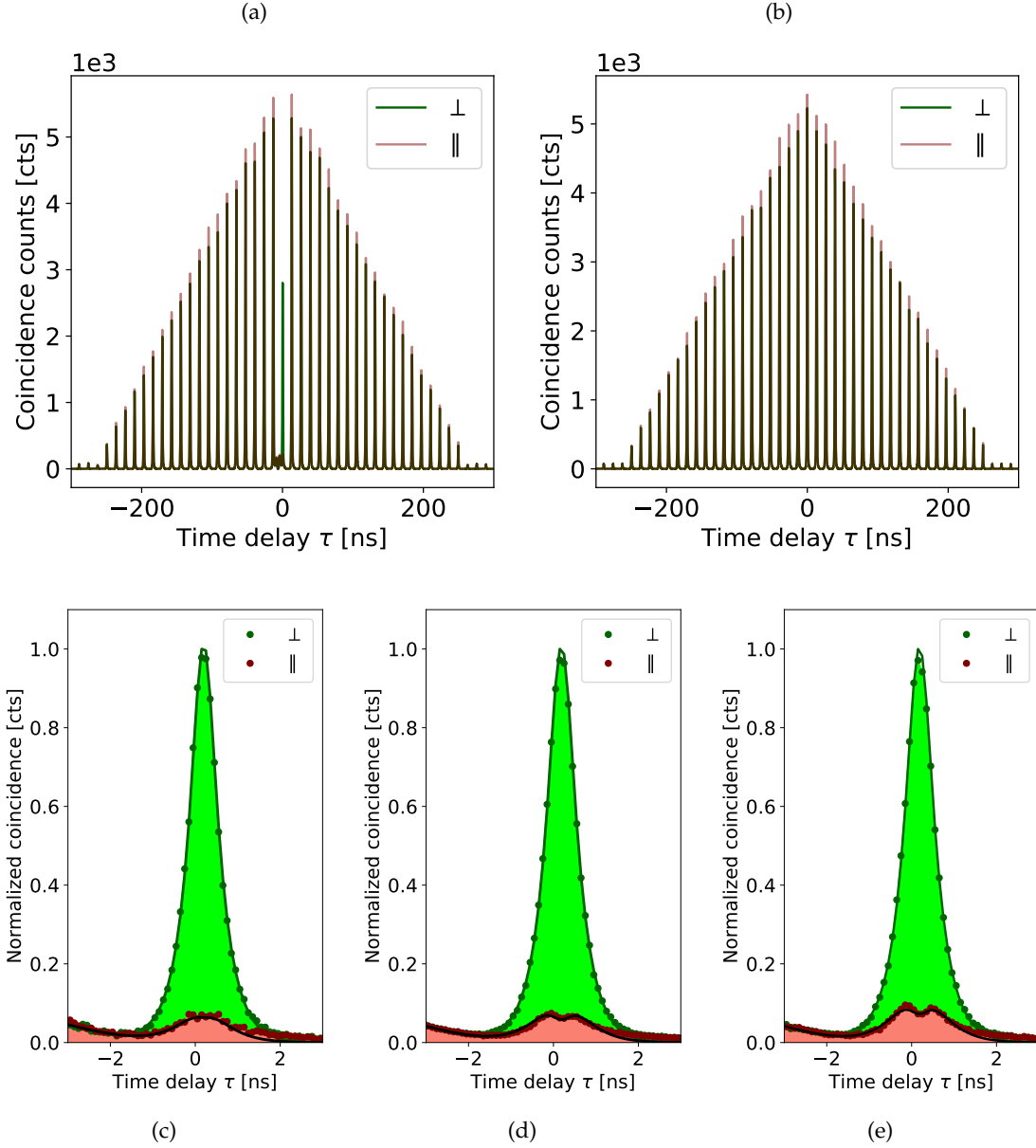


Figure 3.6: HOM interference coincidence histograms of the demultiplexer output modes. **(a)** Raw coincidence histogram of overlap between output  $M_1$  and  $M_2$  in the **co**( $\parallel$ )- and **cross**( $\perp$ )-polarised configuration of the HOM experiment. The time difference between emission of the photons in this overlap is  $\Delta t = 262.6$  ns. Note the detector correlation noise at time delays close to  $\tau = 0$ . **(b)** The same coincidence histogram as (a) but time shifted by  $\frac{M \cdot N}{F_{rep}} = 262.6$  ns i.e. coincidence histogram of two consecutive photon bursts. **(c)** Normalised central peaks in the **co**( $\parallel$ )- and **cross**( $\perp$ )-configuration for overlap of output  $M_1$  and  $M_2$ . The black(**green**) curve is a fit of the central peak of the histogram acquired in the **co**(**cross**)-configuration according to eq. (2.27) with an added Gaussian contribution to account for the detector correlation noise. **(d)** same as (c) for output  $M_1$  and  $M_3$  overlap. Time between photon emission is here  $\Delta t = 525.3$  ns. **(e)** same as (c) for output  $M_1$  and  $M_4$  overlap. Time between photon emission is here  $\Delta t = 789.9$  ns.

area under the peak within a time window of 4 ns. From the area under peak values the corrected HOM visibility is calculated according to eq. (2.28) and eq. (2.31). The corrected HOM visibilities of the three demultiplexer output overlap configurations ( $M_1$  &  $M_2$ ,  $M_1$  &  $M_3$

and  $M_1 \& M_4$ ) are found to be

$$V_{HOM,1\&2} = (89.5 \pm 1.8)\%, \quad V_{HOM,1\&3} = (86.9 \pm 1.7)\%, \quad V_{HOM,1\&4} = (84.8 \pm 1.7)\%. \quad (3.9)$$

For reference, the direct measured corrected HOM visibility i.e. measured directly from the source (before entering the demultiplexer) just before measuring the demultiplexer output HOM visibility, is

$$V_{HOM,source} = (91.1 \pm 1.3)\%. \quad (3.10)$$

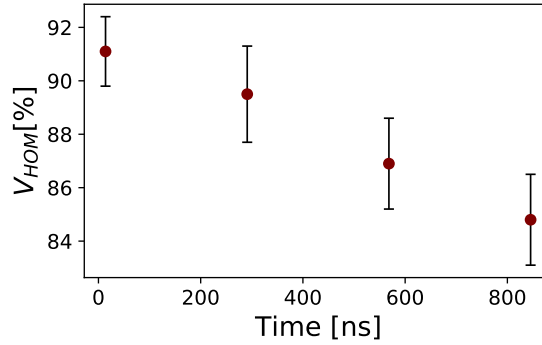


Figure 3.7: HOM visibilities of the demultiplexed QD single photon source. The horizontal axis denotes the time between the emission of the photons overlapped in the HOM experiment i.e. the photon age difference. The HOM visibility at time  $t = 13\text{ps} (\sim 0)$  is measured directly out of the source setup, and the last three visibilities corresponds the overlap of demultiplexer output  $M_1 \& M_2$ ,  $M_1 \& M_3$  and  $M_1 \& M_4$  respectively, as presented in eq. (3.9) calculated from correlation histograms presented in figs. 3.6c to 3.6e.

The central peaks of each HOM measurement and corresponding fit are plotted in figs. 3.6c to 3.6e. In contrast to the initial HOM visibility observed in section 2.4.2 (fig. 2.13), we do at longer timescales observe the characteristics of some dephasing phenomena similar to the pure dephasing described in eq. (2.25) and illustrated in fig. 2.11. The increase in magnitude of the suppressed peaks could be an artefact of imperfect polarisation quality in the reflection arms of the PBSs. The extinction ratio on the PBS reflection are specified to be 20 : 1 to 100 : 1 [52] in contrast to 1000 : 1 for transmission. Going from overlap  $M_1 \& M_2$  to  $M_1 \& M_3$  to  $M_1 \& M_4$  the number of reflections increase probably degrading the polarisation quality. This could be overcome by implementing a high efficiency polariser on the reflected path of each PBS. The polarisation quality is not an issue when using the demultiplexed photons in the entanglement gate presented in chapter 4, as this has a polarisation filter on the input.

The anomaly in the tail of central peak for the co- and cross-polarized configuration is considered an artefact of the detector due to channel correlation effects. This noise is compensated for by adding a Gaussian contributions to the fit, which is not included in the HOM visibility estimation. Even so this correlation artefact probably still contributes to the amplitude of the central peak, effectively lowering the obtainable HOM visibility. Furthermore, the HOM setup used in this sections differs from that of section 2.4.2, in the sense of the implemented BS with a measured transmission and reflection at  $(T : R) = (0.507 : 0.493) \pm 0.013$ . In addition the classical visibility is not sufficiently characterised in this setup, why it is assumed to be limited only by the BS ratio i.e.  $(1 - \epsilon) = 2\sqrt{RT}$ . In reality the classical visibility will also be limited by imperfect polarisation matching and imperfect

balancing of the power in the two arms of the Mach Zehnder interferometer. These two parameters are in this setup optimised by minimising interference fringes and balancing the two arms best possible when installing the experimental setup. Under the assumption that the classical visibility is only limited by the BS and considering the detector channel correlation noise, the presented HOM visibilities should only be considered as giving a lower bound. Errors are in this section estimated in accordance with section 2.4.2.

### 3.7 Summary

In this chapter temporal-to-spatial mode conversion of a QD single photon source to a four-photon source is presented. The expected four-fold coincidence rate with respect to an achieved source efficiency  $\eta_S = 5.1\%$  presented in section 2.3 is 23Hz. The estimated rate is consistent with the measured four-fold coincidence rate of 3.41Hz for a source efficiency of 3.0%. The HOM visibility measured of the overlapped demultiplexer output modes are across output  $M_1$  and  $M_2$ :  $V_{HOM,1\&2} = (89.5 \pm 1.8)\%$ , across  $M_1$  and  $M_3$ :  $V_{HOM,1\&3} = (86.9 \pm 1.7)\%$  and across  $M_1$  and  $M_4$ :  $V_{HOM,1\&4} = (84.8 \pm 1.7)\%$ , which is considered a lower bound for demultiplexed single photons with a HOM visibility  $V_{HOM,source} = (91.1 \pm 1.3)\%$  measured directly out of the QD single photon source.

---

## Chapter 4

# Heralded entanglement generation

---

EPR pairs are key to enable secure communication in DIQKD protocols as introduced in section 1.3.2. In this chapter a scheme for generation of heralded entangled photon pairs is presented. The scheme was first proposed and demonstrated with a spontaneous parametric down conversion (SPDC) single photon source in [15]. In this work, we demonstrate the same entanglement generation scheme using the demultiplexed QD single photon source as presented in chapter 2 and chapter 3, which offers a significantly higher operational rate in comparison to SPDC sources.

### 4.1 Heralded entanglement gate operation

The entanglement gate setup is presented in fig. 4.1. The implementation has four inputs ( $A$ ,  $B$ ,  $C$  and  $D$ ) coupled to a four-mode single photon source e.g. the demultiplexed QD single photon source, and four outputs  $A'$ ,  $B'$ ,  $C'$  and  $D'$  coupled into polarisation resolving detectors.

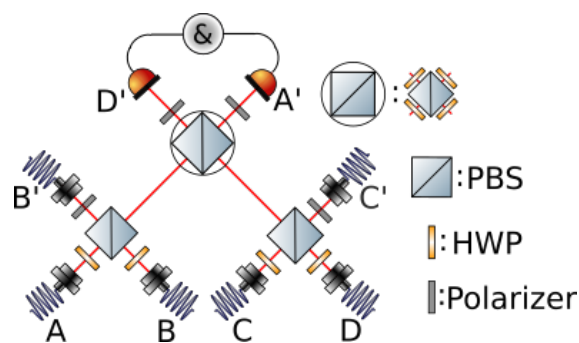


Figure 4.1: Schematic of the heralded entanglement gate requiring four indistinguishable photons on input  $A$ ,  $B$ ,  $C$  and  $D$ . Photon pairs interfere when superimposed on PBSs after which two outputs ( $A'$  and  $D'$ ) are sacrificed for heralding a Bell state photon pair on output  $B'$  and  $C'$ .

The first optical element each input photon encounters is a half wave plate (HWP) oriented at  $22.5^\circ$ , which rotates the photons into a diagonal polarisation state. From here the photons on path  $A$  and  $B$  and the photons on path  $C$  and  $D$  are superimposed on a polarising beam

splitter(PBS). Path A and D are then overlapped on a rotated PBS(RPBS), consisting of a PBS with HWPs oriented at  $22.5^\circ$  on both in- and outputs. Coincidence measurements on output  $A'$  and  $D'$  at different polarisation projection combinations are used to herald an entangled Bell state on path  $B'$  and  $C'$ . On all four outputs a HWP followed by a PBS is installed to enable polarisation resolved measurements by projecting the states on to a pre-selected polarisation basis.

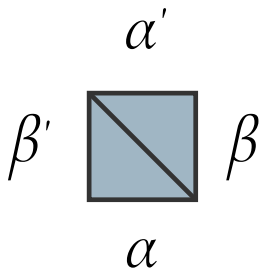
The two building blocks of the entanglement gate are HWPs and PBSs. Assuming a perfect input state the ideal linear operations of these two optical components may be described in a Jones vector inspired transformation matrix formalism[57]. Here a photon is modelled by a two dimensional vector where the two elements represents the creation of horizontal and vertical polarisation state on a specific spatial and temporal mode.  $\hat{\alpha}_H^\dagger$  ( $\hat{\alpha}_V^\dagger$ ) is the horizontal(vertical) photon creation operator. The time dependency and spatial dependency is left out for simplicity by assuming that the photons are perfectly overlapped in time and space. In this formalism linear operations may be described by Jones matrices, for which a HWP with fast axis oriented along the vertical spatial axis ( $\hat{\mathbf{T}}_{HWP}$ ) and an element-rotation operation ( $\hat{\mathbf{R}}(\theta)$ ) is given by:

$$\mathbf{T}_{HWP} = \begin{pmatrix} 1 & 0 \\ 0 & e^{i\pi} \end{pmatrix}, \quad \mathbf{R}(\theta) = \begin{pmatrix} \cos(\theta) & -\sin(\theta) \\ \sin(\theta) & \cos(\theta) \end{pmatrix}. \quad (4.1)$$

By combining these linear operations, the transformation matrix for a HWP oriented at  $22.5^\circ$  with respect to the fast axis is given by:

$$\begin{pmatrix} \hat{\alpha}'_H^\dagger \\ \hat{\alpha}'_V^\dagger \end{pmatrix} = \mathbf{R}(22.5^\circ)\mathbf{T}_{HWP}\mathbf{R}(-22.5^\circ) \begin{pmatrix} \hat{\alpha}_H^\dagger \\ \hat{\alpha}_V^\dagger \end{pmatrix} = \frac{1}{\sqrt{2}} \begin{bmatrix} 1 & 1 \\ 1 & -1 \end{bmatrix} \begin{pmatrix} \hat{\alpha}_H^\dagger \\ \hat{\alpha}_V^\dagger \end{pmatrix}. \quad (4.2)$$

Now extending the formalism to include two spatial photon modes a transformation matrix for a PBS with in and output relations as given in fig. 4.2 can be described by the matrix given in eq. (4.3). Here the horizontal polarisation is transmitted and the vertical polarisation is reflected, upon which it obtains a  $\pi/2$  phase shift.



The diagram shows a square representing a PBS. A diagonal line from the top-left to the bottom-right corner divides the square. The top-left corner is labeled  $\alpha'$ , the top-right corner is labeled  $\beta$ , the bottom-left corner is labeled  $\beta'$ , and the bottom-right corner is labeled  $\alpha$ .

$$\begin{pmatrix} \hat{\alpha}'_H^\dagger \\ \hat{\alpha}'_V^\dagger \\ \hat{\beta}'_H^\dagger \\ \hat{\beta}'_V^\dagger \end{pmatrix} = \begin{bmatrix} 1 & 0 & 0 & 0 \\ 0 & 0 & 0 & i \\ 0 & 0 & 1 & 0 \\ 0 & i & 0 & 0 \end{bmatrix} \begin{pmatrix} \hat{\alpha}_H^\dagger \\ \hat{\alpha}_V^\dagger \\ \hat{\beta}_H^\dagger \\ \hat{\beta}_V^\dagger \end{pmatrix}. \quad (4.3)$$

Figure 4.2: In and output relations of a PBS, with input modes  $\alpha$  and  $\beta$ , and output modes  $\alpha'$  and  $\beta'$ .

## 4.2 State evolution

By combining the HWP and PBS transformation matrices in eq. (4.2) and eq. (4.3) in accordance with the heralded entanglement scheme in fig. 4.1 a full transformation matrix of



the setup can be described. The extended operational matrix accounting for a vector space including all four spatial modes of the entanglement gate is:

$$\begin{pmatrix} \hat{a}'_H \\ \hat{a}'_V \\ \hat{b}'_H \\ \hat{b}'_V \\ \hat{c}'_H \\ \hat{c}'_V \\ \hat{d}'_H \\ \hat{d}'_V \end{pmatrix} = \underbrace{\begin{bmatrix} \frac{1}{2\sqrt{2}} & \frac{1}{2\sqrt{2}} & i\frac{1}{2\sqrt{2}} & -i\frac{1}{2\sqrt{2}} & \frac{1}{2\sqrt{2}} & -\frac{1}{2\sqrt{2}} & i\frac{1}{2\sqrt{2}} & i\frac{1}{2\sqrt{2}} \\ \frac{1}{2\sqrt{2}} & \frac{1}{2\sqrt{2}} & i\frac{1}{2\sqrt{2}} & -i\frac{1}{2\sqrt{2}} & -\frac{1}{2\sqrt{2}} & \frac{1}{2\sqrt{2}} & -i\frac{1}{2\sqrt{2}} & -i\frac{1}{2\sqrt{2}} \\ 0 & 0 & \frac{1}{\sqrt{2}} & \frac{1}{\sqrt{2}} & 0 & 0 & 0 & 0 \\ i\frac{1}{\sqrt{2}} & -i\frac{1}{\sqrt{2}} & 0 & 0 & 0 & 0 & 0 & 0 \\ 0 & 0 & 0 & 0 & \frac{1}{\sqrt{2}} & \frac{1}{\sqrt{2}} & 0 & 0 \\ 0 & 0 & 0 & 0 & 0 & 0 & i\frac{1}{\sqrt{2}} & -i\frac{1}{\sqrt{2}} \\ i\frac{1}{2\sqrt{2}} & i\frac{1}{2\sqrt{2}} & \frac{1}{2\sqrt{2}} & -\frac{1}{2\sqrt{2}} & i\frac{1}{2\sqrt{2}} & -i\frac{1}{2\sqrt{2}} & \frac{1}{2\sqrt{2}} & \frac{1}{2\sqrt{2}} \\ -i\frac{1}{2\sqrt{2}} & -i\frac{1}{2\sqrt{2}} & -\frac{1}{2\sqrt{2}} & \frac{1}{2\sqrt{2}} & i\frac{1}{2\sqrt{2}} & -i\frac{1}{2\sqrt{2}} & \frac{1}{2\sqrt{2}} & \frac{1}{2\sqrt{2}} \end{bmatrix}}_{\hat{\mathbf{T}}_{gate}} \begin{pmatrix} \hat{a}_H \\ \hat{a}_V \\ \hat{b}_H \\ \hat{b}_V \\ \hat{c}_H \\ \hat{c}_V \\ \hat{d}_H \\ \hat{d}_V \end{pmatrix}, \quad (4.4)$$

where  $\hat{a}'_V$  corresponds to a creation of a vertical polarised photon on path A and  $\hat{c}'_H$  corresponds to a creation of a horizontally polarised photon on path C', etc. Applying the full transformation matrix of the entanglement gate ( $\hat{\mathbf{T}}_{gate}$ ) to the input state

$$|\psi\rangle_{ABCD} = |HHHH\rangle_{ABCD} = \hat{a}_H^\dagger \hat{b}_H^\dagger \hat{c}_H^\dagger \hat{d}_H^\dagger |0\rangle, \quad (4.5)$$

yields the final state

$$\begin{aligned} |\psi\rangle_{A'B'D'C'} = & \frac{1}{64} \left( \hat{a}'_H + \hat{a}'_V + i2\hat{b}'_V + i\hat{d}'_H - i\hat{d}'_V \right) \left( i\hat{a}'_H + i\hat{a}'_V + 2\hat{b}'_H + \hat{d}'_H - \hat{d}'_V \right) \\ & \times \left( \hat{a}'_H - \hat{a}'_V - 2\hat{c}'_H + i\hat{d}'_H + i\hat{d}'_V \right) \left( i\hat{a}'_H - i\hat{a}'_V + i2\hat{c}'_V + \hat{d}'_H + \hat{d}'_V \right) |0\rangle. \end{aligned} \quad (4.6)$$

Expanding this expression and accounting for destructive photon interference, the final expression includes 144 terms out of which only eight terms, can possible result in a four-fold detection i.e. a concurrent detection on all four output modes ( $A'$ ,  $B'$ ,  $C'$ , and  $D'$ ). These are the entangled states

$$|\psi\rangle_{A'B'C'D',reduced} = \frac{1}{4} (\Psi_{A',D'}^+ \Phi_{B',C'}^+ - \Phi_{A',D'}^+ \Psi_{B',C'}^+), \quad (4.7)$$

where  $\Psi_{A,B}^\pm$  and  $\Phi_{A,B}^\pm$  are the maximally entangled Bell states[21]

$$\Psi_{A,B}^\pm = \frac{1}{\sqrt{2}} (\hat{a}_H^\dagger \hat{\beta}_V^\dagger \pm \hat{a}_V^\dagger \hat{\beta}_H^\dagger) |0\rangle, \quad (4.8a)$$

$$\Phi_{A,B}^\pm = \frac{1}{\sqrt{2}} (\hat{a}_H^\dagger \hat{\beta}_H^\dagger \pm \hat{a}_V^\dagger \hat{\beta}_V^\dagger) |0\rangle. \quad (4.8b)$$

From eq. (4.7) it is evident that upon a four-fold coincident measurement on the four output modes, the output state will be maximally entangled.

### 4.3 Heralding efficiency

An important feature of the entanglement gate is the ability to herald an EPR pair. As shown in previous section(section 4.2) a four-fold coincidence on path  $A'$ ,  $B'$ ,  $C'$  and  $D'$  can ideally only happen when a Bell state is shared between path  $A'$  and  $D'$  and path  $B'$  and  $C'$ . This feature may be utilised by sacrificing two outputs to *herald* a Bell pair on the remaining two. The heralding can be employed as a heralding station in a DIQKD protocol or as a local heralding of entangled photon generation. The latter is implemented in the setup in fig. 4.1. An optical element i.e. a HWP followed by a PBS, is implemented prior to the single photon detectors to enable polarisation resolving detection. By projective measurement we may then herald on either  $|HH\rangle_{A'D'}$ ,  $|VV\rangle_{A'D'}$ ,  $|HV\rangle_{A'D'}$  or  $|VH\rangle_{A'D'}$ . The heralding efficiency is given by ratio between the probability to successfully herald an entangled state and the total probability to get a heralding detection. The heralding efficiency is defined as [49]

$$\eta_H = \frac{\rho_{\Psi_{B,C}^+}^{(h,j)} + \rho_{\Phi_{B,C}^+}^{(h,j)}}{\rho_{\Psi_{B,C}^+}^{(h,j)} + \rho_{\Phi_{B,C}^+}^{(h,j)} + \rho_{\epsilon}^{(h,j)}}. \quad (4.9)$$

Here  $\rho_{\psi_{B,C}}^{(h,j)}$  is the probability to measure a certain state  $\psi_{B,C}$  on path  $B'$  and  $C'$  concurrent with a herald on path  $A'$  and  $D'$ ,  $h, j \in \{H, V\}$  is the polarisation projection of the heralding paths( $A'$  and  $D'$  respectively) and  $\epsilon$  is an erroneous state i.e. a heralding coincident detection between path  $A'$  and  $D'$ , that does not originate from the state in eq. (4.7) e.g. having a two photon state in one of paths  $B'$  or  $C'$ .

Two types of detectors can be considered: photon-number-resolving detectors and *non*-photon-number-resolving detectors. An example of the latter is SNSPDs, as described in appendix A.1, which are the used detectors in our setup. When two detectors are available, one on each heralding arm, we may herald on only one combination of polarisation projections  $|hj\rangle_{A'D'}$  with  $h, j \in \{H, V\}$ . Opposite with four detectors available, two on each heralding arm, all four projection combinations may be measured simultaneously. The availability of detectors is considered for both non-photon-number-resolving detectors and photon-number-resolving detectors, which yields a heralding efficiency of:

**Non-photon-number-resolving detectors** e.g. SNSPDs

2 detectors available:  $\rho_{\Psi_{B,C}^+}^{(j,j)} = \frac{1}{32}$  and  $\rho_{\Phi_{B,C}^+}^{(j,j)} = 0, \rho_{\epsilon}^{(j,j)} = \frac{17}{256}$  with  $j \in \{H, V\}$  **or**  $\rho_{\Psi_{B,C}^+}^{(j,h)} = 0$  and  $\rho_{\Phi_{B,C}^+}^{(j,h)} = \frac{1}{32}, \rho_{\epsilon}^{(j,h)} = \frac{17}{256}$  with  $j \neq h$  both cases yielding a heralding efficiency of

$$\eta_H = 32.0\%. \quad (4.10)$$

4 detectors available  $\rho_{\Psi_{B,C}^+}^{(h,j)} = \frac{1}{32}, \rho_{\Phi_{B,C}^+}^{(h,j)} = \frac{1}{32}$  and  $\rho_{\epsilon}^{(h,j)} = \frac{17}{256}$  with  $h, j \in \{H, V\}$  yielding a heralding efficiency of

$$\eta_H = 61.5\%. \quad (4.11)$$

**Photon-number-resolving detectors**

2 detectors available:  $\rho_{\Psi_{B,C}^+}^{(j,j)} = \frac{1}{32}, \rho_{\Phi_{B,C}^+}^{(j,j)} = 0$  and  $\rho_{\epsilon}^{(j,j)} = \frac{3}{64}$  with  $j \in \{H, V\}$  **or**  $\rho_{\Psi_{B,C}^+}^{(j,j)} = 0, \rho_{\Phi_{B,C}^+}^{(j,j)} = \frac{1}{32}$  and  $\rho_{\epsilon}^{(j,j)} = \frac{3}{64}$  with  $j \neq h$  yielding a heralding efficiency of

$$\eta_H = 40.0\%. \quad (4.12)$$

4 detectors available:  $\rho_{\Psi_{B,C}^+}^{(h,j)} = \frac{1}{16}$ ,  $\rho_{\Phi_{B,C}^+}^{(h,j)} = \frac{1}{16}$  and  $\rho_{\epsilon}^{(h,j)} = 0$  with  $h, j \in \{H, V\}$  both cases yielding a heralding efficiency of

$$\eta_H = 100\%. \quad (4.13)$$

The first presented heralding efficiency (eq. (4.10)) with two *non*-photon-number-resolving detectors is the case for the implemented experimental setup. The other scenarios provides inspiration for feasible setup improvements. The heralding efficiencies presented here are based on the ideal scenarios i.e. with a perfect single photon source and optical elements. A first attempt in trying to address a more realistic scenario has been investigated in [49]. A more accurate modelling of the effect of the single photon HOM visibility on the heralding efficiency is pending.

#### 4.4 Experimental setup alignment and characterisation

The experimental implementation of the heralded entanglement gate is presented in fig. 4.3. This consists of over 30 optical elements, which all need to play along together to realise the heralded entanglement generation presented in previous sections. In this section angular alignment and characterisation of all HWPs used is first presented, followed by the setup end-to-end transmission efficiency characterisation and finally photon mode matching and overlap characterisation.

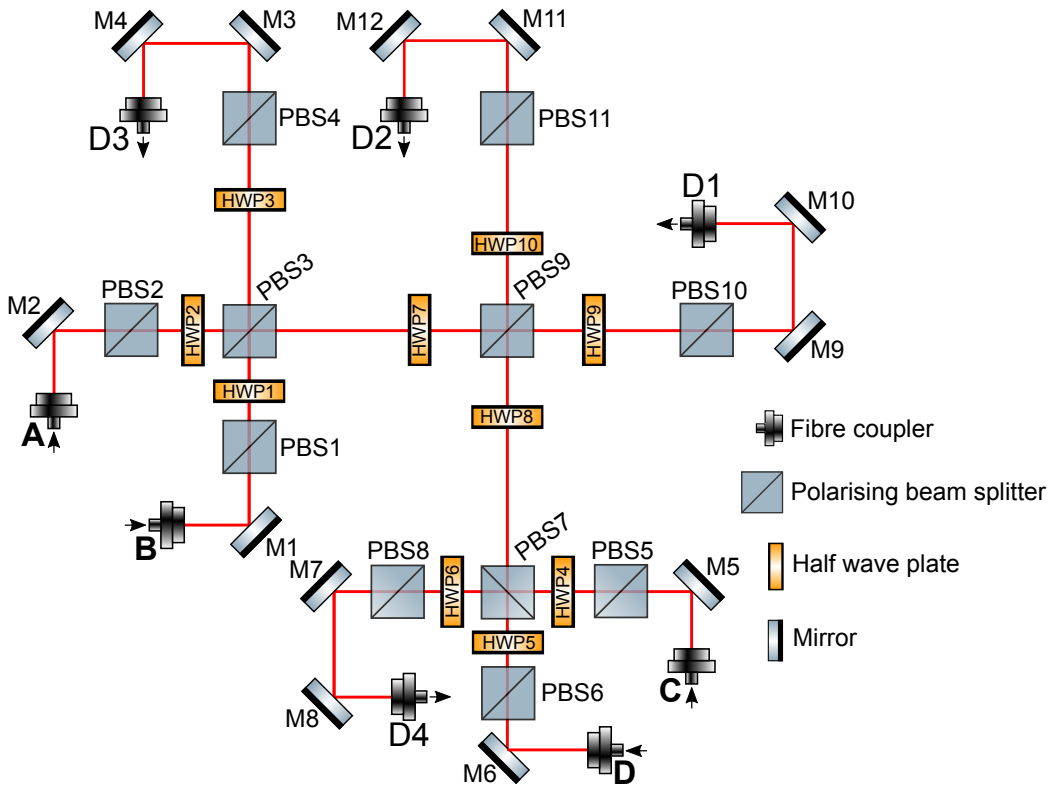


Figure 4.3: Sketch of the entanglement gate experimental setup with labelling of all optical components. Fibre coupler arrows indicate an in or output coupling.

### 4.4.1 HWP alignment and characterisation

In the heralded entanglement gate scheme the HWPs play a crucial role, and hence these need proper alignment. In the entanglement protocol the fast axis of the 8 HWPs must be set at an angle of  $22.5^\circ$  with respect to the vertical axis. The HWPs in the setup are commercial, free space HWPs mounted by hand in rotation mounts; consequently, the mount indicated angle do not necessarily reflect the true HWP angle. In order to characterise the *mount angle* to *true angle* relationship of the HWPs we employ the quarter-wave-plate(QWP) method[58]. The rotating wave plate method is based on a setup as depicted in fig. 4.4, where the Stokes parameters of an arbitrary light beam can be resolved by analysing the intensity of the transmitted light of a rotateable QWP followed by a polariser. This may be utilised to determine the angle of a HWP by sending a laser beam with well known polarisation through the HWP and resolve the polarisation of the transmitted light. First a brief introduction to the Stokes formalism.

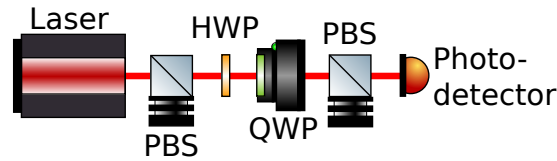


Figure 4.4: Rotating-wave-plate stokes polarimeter setup used to characterise the *mount angle* to *true angle* relationship of the setup HWPs and to confirm their final alignment.

Classical polarised light propagating along the  $z$ -axis may be described by two orthogonal components along the  $x$ - and  $y$ -axis. These components are given by

$$E_x(z, t) = E_{0x} \cos(\omega t - \kappa z + \delta_x), \quad (4.14a)$$

$$E_y(z, t) = E_{0,y} \cos(\omega t - \kappa z + \delta_y). \quad (4.14b)$$

Here  $E_{0x}$  and  $E_{0y}$  are the electric field amplitudes of the two orthogonal components,  $\omega = 2\pi\nu$  is the angular frequency,  $\kappa = 2\pi/\lambda$  is the wave number and  $\delta_x$  and  $\delta_y$  are phase constants.  $\omega t - \kappa z$  is also known as the *propagator*, as it describes the propagation of the wave in time and space. As the electromagnetic field is a non-observable we cannot extract any information of it's polarisation from the field itself. Instead we may eliminate the time-space propagator ( $\omega t - \kappa z$ ) between the two equations in eq. (4.14), which leads to the equation of an ellipse[57]. This ellipse visualises the polarisation behaviour of light, and is referred to as the *polarisation ellipse* illustrated in fig. 4.5. The ellipse equation is given by:

$$\underbrace{\sin^2 \delta}_{S_0^2} = \underbrace{\frac{\langle E_x(z, t)^2 \rangle_T}{E_{0x}^2}}_{S_1^2} + \underbrace{\frac{\langle E_y(z, t)^2 \rangle_T}{E_{0y}^2}}_{S_2^2} - \underbrace{\frac{2\langle E_x(z, t)E_y(z, t) \rangle_T}{E_{0x}E_{0y}}}_{S_3^2} \cos \delta, \quad (4.15)$$

where  $\delta = \delta_y - \delta_x$  and  $\langle \rangle_T$  denotes the time average. By time averaging the polarisation ellipse is transformed into the intensity domain (observable). Under-braced in eq. (4.15) is noted the corresponding *Stokes polarisation parameters* such that the equation reads  $S_0^2 = S_1^2 + S_2^2 + S_3^2$ . The four Stokes polarisation parameters can be used to describe un-, partially- and fully

polarised light. These are in matrix notation given by

$$\mathbf{S} = \begin{pmatrix} S_0 \\ S_1 \\ S_2 \\ S_3 \end{pmatrix} = \begin{pmatrix} \langle E_{0x}^2 \rangle_T + \langle E_{0y}^2 \rangle_T \\ \langle E_{0x}^2 \rangle_T - \langle E_{0y}^2 \rangle_T \\ \langle E_{0x} E_{0y} \cos \epsilon \rangle_T \\ \langle E_{0x} E_{0y} \sin \epsilon \rangle_T \end{pmatrix}. \quad (4.16)$$

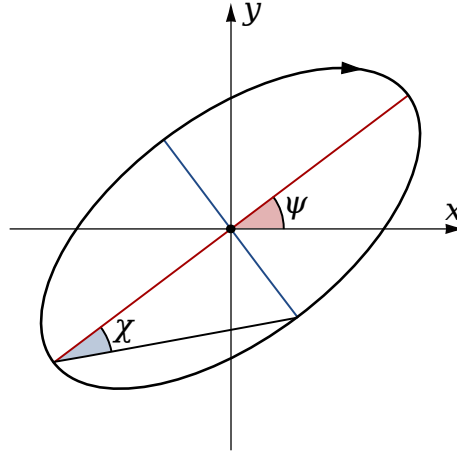


Figure 4.5: The polarisation ellipse. The span of the polarisation ellipse along the x-axis corresponds to  $2E_{0x}$  and likewise the span of the ellipse along the y-axis is  $2E_{0y}$ . Here the orientation angle( $\psi$ ) is marked in red and the is end ellipticity angle  $\chi$  marked in blue. Reprinted from [59].

The Stokes parameter  $S_0$  describes the total intensity of the optical beam,  $S_1$  describes the preponderance of linearly horizontally polarised light over linearly vertically polarised light,  $S_2$  describes the preponderance of linear  $+45^\circ$  polarised light over linear  $-45^\circ$  polarised light, and  $S_3$  describes the preponderance of right circularly polarised light over left circularly polarised light. The degree of polarisation(DOP) is given by  $DOP = \sqrt{S_1^2 + S_2^2 + S_3^2}/S_0$ . For completely polarised light  $DOP = 1$  and partially polarised light is represented by  $0 < DOP < 1$ .

The polarisation ellipse can be described in terms of two angles: The orientation angle  $\psi$  and an ellipticity angle  $\chi$  as seen in fig. 4.5. The ellipse collapses to a straight line when  $\chi = 0$  oriented at angle  $\psi$ , corresponding to the equator of the Poincaré sphere. This is the case when the light is purely a superposition of the in phase harmonic motions i.e. purely linearly polarised. The orientation angle and ellipticity angle is related to the Stokes parameters as

$$\psi = \frac{1}{2} \tan^{-1} \left( \frac{S_2}{S_1} \right) \quad (0 < \psi \leq \pi), \quad (4.17)$$

$$\chi = \frac{1}{2} \sin^{-1} \left( \frac{S_3}{S_0} \right) \quad \left( -\frac{\pi}{4} < \psi \leq \frac{\pi}{4} \right). \quad (4.18)$$

In the case where pure horizontally polarised light is transmitted through a HWP, the relation between the orientation of the HWP( $\theta_{HWP}$ ) and the orientation angle( $\psi$ ) is given by

$$\theta_{HWP} = \frac{1}{2} \psi. \quad (4.19)$$

In order to experimentally arrive at an set of Stokes parameters to characterise the angle of a given HWP, we here use the rotating quarter-waveplate measurement. This measurement uses a QWP that can be rotated through an angle  $\theta$  followed by a linear polariser with transmission axis fixed in the x-direction i.e. projecting on to the horizontal polarisation axis (as a PBS), after which a detector is placed. We place the HWP that has to be characterised in the path of a horizontally polarised laser beam before the rotating QWP. The setup is shown in fig. 4.4. The intensity of the optical beam on the detector is now related to the Stokes parameters as[58]

$$I(\theta) = \frac{1}{2}(A + B \sin(2\theta) + C \cos(4\theta) + D \sin(4\theta)), \quad (4.20)$$

where  $A = S_0 + S_1/2$ ,  $B = S_3$ ,  $C = S_1/2$  and  $D = S_2/2$ . The intensity is approximated as a truncated Fourier series consisting of a DC term, a second harmonic term, and two fourth harmonic terms. By sampling the intensity whilst rotating the QWP through  $180^\circ$  we may reconstruct the Stokes parameters according to[58, 60]

$$A = \frac{2}{N} \sum_{n=1}^N I_n, \quad B = \frac{4}{N} \sum_{n=1}^N I_n \sin(2\theta_n), \quad (4.21a)$$

$$C = \frac{4}{N} \sum_{n=1}^N I_n \cos(4\theta_n), \quad D = \frac{4}{N} \sum_{n=1}^N I_n \sin(4\theta_n). \quad (4.21b)$$

$$(4.21c)$$

When reconstructing the Stokes parameters from the sampled entities, it is crucial to consider the true retardance of the QWP used. This is included in the denominator in the following relations according to[60]

$$S_0 = \frac{A - C}{\tan^2(\delta/2)}, \quad S_1 = \frac{2C}{2 \sin^2(\delta/2)}, \quad (4.22a)$$

$$S_2 = \frac{2D}{2 \sin^2(\delta/2)}, \quad S_3 = \frac{B}{\sin(\delta)}. \quad (4.22b)$$

$$(4.22c)$$

The true retardance of the rotating QWP is determined with the crossed polariser method suggested in [61]. By removing the HWP in the setup in fig. 4.4, and setting the polarisers in a cross-polarisation configuration, the intensity measured by the detector will be given by  $I(\alpha, \delta) = I_0/4(1 + \cos(\delta) \cos(2\alpha))$ , where  $\alpha$  is the QWP angle. This leads to the following expression for the retardance:

$$\cos(\delta) = \frac{I(0^\circ, \delta) - I(90^\circ, \delta)}{I(0^\circ, \delta) + I(90^\circ, \delta)}. \quad (4.23)$$

Conducting this measurement we found that  $\delta = (1.553 \pm 0.001)\lambda \simeq (0.2472 \times 2\pi)\lambda$  for  $\lambda = 942\text{nm}$ , where  $2\pi$  corresponds to a full wavelength. The error on delta is estimated by the standard deviation from 10 separate measurements and propagated onto the retardance.

In order to recreate the Stokes parameters by sampling as described above, it is important to include a sufficient number of samples. Nyquist's sampling theorem states that "a continuous time signal can be reconstructed from its samples if it is sampled at a rate at least twice its highest frequency component"[62]. Following this rule of thumb we ought to sample at a rate above the Nyquist rate, i.e  $N > 8$  in this case. For this characterisation  $N = 12$  is chosen in order to be well above the thresh hold.

The HWP *mount angle to true angle* relationship is quantified by the measured values for the angle offset when the HWP *mount angle* is set to 0. This is presented in table 4.1 along with the measured HWP *true angles* in the final alignment of each of the HWPs. The error on  $\theta$  is estimated by an initial fit of a data set acquired from a measurement run without a HWP, which also determines the QWP *true angle to mount angle* offset. The final error estimations are based on error propagation[44].

HWP#	$\theta_{HWP}$ (Mount @ 0°)	$\theta_{HWP}$ (@22.5°)	DOP (@22.5°)	$\chi$ (@22.5°)
1	$(0.78 \pm 0.04)^\circ$	$(22.50 \pm 0.03)^\circ$	$(0.94 \pm 0.18)$	$(-0.62 \pm 0.03)^\circ$
2	$(-0.41 \pm 0.05)^\circ$	$(22.54 \pm 0.04)^\circ$	$(0.94 \pm 0.17)$	$(-0.72 \pm 0.03)^\circ$
3	$(-1.54 \pm 0.05)^\circ$	$(22.49 \pm 0.04)^\circ$	$(0.94 \pm 0.18)$	$(-0.39 \pm 0.03)^\circ$
4	$(-3.66 \pm 0.05)^\circ$	$(22.49 \pm 0.04)^\circ$	$(0.95 \pm 0.18)$	$(0.30 \pm 0.03)^\circ$
5	$(0.82 \pm 0.05)^\circ$	$(22.52 \pm 0.04)^\circ$	$(0.95 \pm 0.18)$	$(-1.49 \pm 0.03)^\circ$
6	$(4.93 \pm 0.05)^\circ$	$(22.52 \pm 0.04)^\circ$	$(0.93 \pm 0.18)$	$(-0.19 \pm 0.03)^\circ$
7	$(0.81 \pm 0.05)^\circ$	$(22.51 \pm 0.04)^\circ$	$(0.94 \pm 0.18)$	$(0.27 \pm 0.03)^\circ$
8	$(0.64 \pm 0.05)^\circ$	$(22.49 \pm 0.04)^\circ$	$(0.94 \pm 0.18)$	$(-0.52 \pm 0.03)^\circ$
9	$(1.48 \pm 0.05)^\circ$	$(22.48 \pm 0.04)^\circ$	$(0.95 \pm 0.18)$	$(0.63 \pm 0.03)^\circ$
10	$(2.81 \pm 0.05)^\circ$	$(22.50 \pm 0.04)^\circ$	$(0.95 \pm 0.18)$	$(-0.80 \pm 0.03)^\circ$

Table 4.1: Alignment and characterisation of HWP0-10 of the entanglement gate setup in fig. 4.3. First column (HWP#) is the number of the respective HWP according to fig. 4.3.  $\theta_{HWP}$  for Mount @ 0° notes the *mount angle to true angle* relationship, and  $\theta_{HWP}$  for mount @ 22.5° denotes measured HWP angle for the final HWP alignment.

#### 4.4.2 Transmission efficiency

In order to characterise the transmission efficiency of the the optical components a polarised continuous wave laser with wavelength  $\lambda = 942$  was sent through each of the input ports  $A1, A2, B1$  and  $B2$  in fig. 4.3, one at a time. The intensity on the transmitted and reflected output of PBS4, 6, 10 and 11 was measured, whilst all HWPs of the setup were aligned at  $\theta = 22.5^\circ$ . Next the input intensity is measured before the input polariser(PBS1,2,5 and 6) i.e just after the respective input collimator. The efficiency is then calculated from the input to output ratio. The reflected PBS polariser component is subtracted from the input intensity when evaluating the efficiency; hence, the efficiency measures should be considered as a lower bound. This measurement yields an end-to-end efficiency estimate of the entanglement gate, which offers insight in the degree of alignment and optical transmission efficiency. The measured efficiencies are presented in table 4.2.

The efficiency estimate  $C \rightarrow$  PBS10 transmitted is slightly alarming at  $(5.62 \pm 0.04)\%$  in comparison to the ideal 12.5%. This is, however, the only efficiency estimate below 60% of the ideally ideally expected. In comparison to the total efficiency of input C (83.25%), this may indicate an erroneous measurement. Further investigation is required to fully unravel the lack of transmission on this path.

Path	PBS	R/T	A	B	C	D	Ideal
$A'$	10	T	$(9.6 \pm 0.4)\%$	$(12.4 \pm 0.3)\%$	$(5.62 \pm 0.04)\%$	$(10.40 \pm 0.05)\%$	12.5%
		R	$(8.5 \pm 0.4)\%$	$(11.0 \pm 0.3)$	$(9.61 \pm 0.06)\%$	$(8.53 \pm 0.04)\%$	12.5%
$B'$	4	T	$(20.3 \pm 0.4)\%$	$(18.5 \pm 0.3)\%$			25%
		R	$(19.4 \pm 0.4)\%$	$(26.6 \pm 0.4)\%$			25%
$C'$	7	T			$(21.53 \pm 0.11)\%$	$(30.68 \pm 0.17)\%$	25%
		R			$(18.85 \pm 0.10)\%$	$(17.16 \pm 0.09)\%$	25%
$D'$	11	T	$(15.0 \pm 0.4)\%$	$(9.8 \pm 0.3)\%$	$(12.64 \pm 0.03)\%$	$(8.90 \pm 0.03)\%$	12.5%
		R	$(10.1 \pm 0.4)\%$	$(11.4 \pm 0.3)\%$	$(15.00 \pm 0.04)\%$	$(10.61 \pm 0.04)\%$	12.5%
Total			$(82.9 \pm 2.4)\%$	$89.7 \pm 5.5)\%$	$(83.25 \pm 0.3)\%$	$(86.28 \pm 0.4)\%$	100%

Table 4.2: Transmission efficiency of the entanglement gate. Path refers to path as depicted in fig. 4.1 and the PBS column refers to PBS number in fig. 4.3. R/T refers to an intensity measurement on the reflected/transmitted output of the PBS.

### 4.4.3 Mode matching

The working principle of the heralded entanglement gate is based on photon-photon interference, for which both spatial- and temporal mode overlap must be ensured. The photon overlap must be maximised on PBS3, 7 and 9 in fig. 4.3, corresponding to the three PBSs shown in fig. 4.1.

#### Spatial overlap

Best possible spatial overlap is ensured by maximising the the coupling of the input collimators on the collection ports according to an alignment procedure developed by Hans Eriksen [63]. This is done by maximising the the coupling efficiencies while sending a polarised CW laser with wavelength  $\lambda = 942\text{nm}$  through the gate, one input at a time while optimising the outcoupling in the step order according to table 4.3.

Step	1	2	3	4	5	6	7
Coupling	$A \rightarrow D1$	$D \rightarrow D1$	$D \rightarrow D4$	$C \rightarrow D4$	$D \rightarrow D2$	$A \rightarrow D3$	$B \rightarrow D3$
Alignment	M9 & M10	M6 & B2	M7 & M8	M5 & B1	M11 & M12	M3 & M 14	A1 & M1

Table 4.3: Spatial optimisation procedure as developed by [63] and in accordance with fig. 4.3.

Step 1-2 ensures  $A$ - $D$  overlap on PBS9, step 3-4 ensures  $C$ - $D$  overlap on PBS7 and step 5-7 ensures  $A$ - $B$  overlap on PBS3. After completion of this alignment procedure the spatial overlap of the single photon paths should be maximised on PBS-3, -7 and -9. The measured out coupling efficiencies are presented in table 4.4.



$\eta_{C,D}$	D1	D2	D3	D4
A	(91.3 $\pm$ 2.0)%	(86.6 $\pm$ 0.3)%	(92.6 $\pm$ 0.4)%	
B	(89.8 $\pm$ 0.5)%	(79.2 $\pm$ 0.3)%	(94.4 $\pm$ 0.3)%	
C	(92.0 $\pm$ 0.8)%	(92.7 $\pm$ 0.7)%		(94.3 $\pm$ 1.0)%
D	(91.6 $\pm$ 0.4)%	(94.6 $\pm$ 1.3)%		(94.6 $\pm$ 0.7)%

Table 4.4: Outcoupling efficiencies of the entanglement gate.  $\eta_{C,D}$  is the coupling efficiency between input colimator  $C \in \{A, B, C, D\}$  and detector output coupling  $D \in \{D1, D2, D3, D4\}$ . The **green** highlighted efficiencies corresponds to the optimised couplings and the **red** highlights are not optimised only characterised.

### Temporal overlap

The temporal overlap of the entanglement gate is optimised by evaluating a continuously measured photon arrival histogram for input  $A, B, C$ , and  $D$  (one at a time) on detector  $D1$ , while adjusting the freespace delay in the demultiplexer setup discussed in section 3.4. The demultiplexer output modes are connected to the entanglement gate as:  $M_1 \rightarrow D, M_2 \rightarrow C, M_3 \rightarrow A$  and  $M_4 \rightarrow B$ . Optimising the photon arrival time overlap on  $D1$  optimises the temporal photon overlap on PBS9 in the setup as shown in fig. 4.3. The photon arrival time histogram acquired on  $D1$  after optimisation is shown in fig. 4.6. After optimisation the temporal overlap on PBS-3 and -7, should also be maximised. The overlap of the photon arrival time on all four detectors ( $D1, D2, D3$  and  $D4$ ) are measured and characterised using the same statistical methods as discussed in section 3.4. The characterisation is presented in table 4.5. The overlap of photon arrival times on  $D1$  and  $D2$  is correlated with the temporal photon overlap on PBS9, and likewise  $D3$  is correlated with temporal overlap on PBS3 and  $D4$  with PBS7.

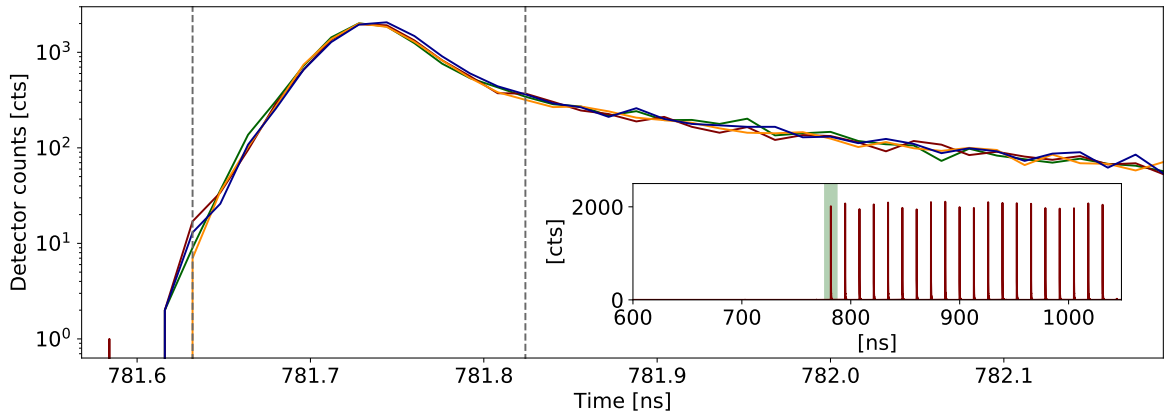


Figure 4.6: Photon arrival histogram collected on  $D1$ . The full burst arrival histogram is shown in the insert, where the **green** shaded region indicates to the time-window of the main figure. The photon arrival time of input  $A$  is shown in **red**,  $B$  in **green**,  $C$  in **orange** and  $D$  in **blue**.

Over- lap	B			A			C			D
	$\chi^2_\nu$	t-test	KS	$\chi^2_\nu$	t-test	KS	$\chi^2_\nu$	t-test	KS	
A	1.14	0.0346	0.0833							
C	0.729	-0.0685	0.0833	0.821	-0.102	0.0833				1
D	1.077	-0.0718	0.167	1.04	-0.0391	0.0833	1.58	-0.00314	0.0833	
A	1.25	-0.0452	0.0833							
C	4.64	0.0615	0.0833	1.85	0.106	0.0833				2
D	0.934	-0.0226	0.0833	2.42	0.103	0.0833	0.961	-0.00133	0.0833	
A	1.65	0.0241	0.0833							3
D							0.269	-0.909	0.25	4

Table 4.5: Overlap test between photon arrival histograms exemplified in fig. 4.6.  $\chi^2_\nu$  is the chi square reduced value of the two photon arrival histograms(eq. (3.6)), t-test is the two sample test statistics and KS is Kolomorgov-Smirnoff test statistics. The **green** highlighted test statistics corresponds to the aligned overlaps and the **red** highlights are non-aligned i.e. a result of the temporal alignment on output  $D_1$ .

## 4.5 Entanglement confirmation

The quantum correlations of the EPR photon pair on path  $B'$  and  $C'$  upon heralding on path  $A'$  and  $D'$  can be confirmed by evaluating *Bell's inequality* as described in section 1.2.1 in a partial Bell state measurement[21]. Bells theorem states that Bell's inequality is always obeyed in the local hidden variable(LHV) picture proposed by Einstein, Podolsky and Rosen(EPR) in the EPR paradox [64]. Quantum mechanics predicts violations of Bell's inequality. An experimental setup for testing Bell-inequalities was proposed by Clauser, Horne, Shimony and Holt(CHSH) in 1969[22]. They introduced an experimentally determinable parameter

$$S \equiv E(\theta_1, \theta_2) - E(\theta_1, \theta'_2) + E(\theta'_1, \theta_2) + E(\theta'_1, \theta'_2), \quad (4.24)$$

which according to Bell's theorem must obey the inequality

$$|S| \leq 2, \quad (4.25)$$

if the LHV picture is valid. The quantum correlations of the photon pairs in eq. (4.24) is given by

$$E(\theta_1, \theta_2) = \mathcal{P}_{11}(\theta_1, \theta_2) + \mathcal{P}_{00}(\theta_1, \theta_2) - \mathcal{P}_{10}(\theta_1, \theta_2) - \mathcal{P}_{01}(\theta_1, \theta_2), \quad (4.26)$$

where  $\mathcal{P}_{ij}(\theta_1, \theta_2)$  is the probability to have a coincident detection on detectors  $D_1(i)$  and  $D_2(j)$  with  $i, j \in \{0, 1\}$  and  $\theta_1$  and  $\theta_2$  is the orientations of the two HWPs in the two detection arms in accordance with the Bell experiment apparatus in fig. 4.7. A two photon quantum correlation fringe visibility of  $V_{E(\theta_1, \theta_2)} = 1/\sqrt{2}$  predicts violation of Bell's inequality in accordance with section 1.2.1. The probability of two detectors firing simultaneously is in theory given by[21]

$$\mathcal{P}_{ij}(\theta_1, \theta_2) = \frac{1}{2} \sin^2 \left[ 2(\theta_2 - \theta_1) + \delta_{ij} \frac{\pi}{2} \right], \quad (4.27)$$

where  $\delta_{i,j}$  is the Kronecker delta.

The experimental setup for measuring this  $S$  parameter is fairly simple and consist of two half wave plates(HWP), two polarising beam splitters(PBS) and four detectors. Two photons

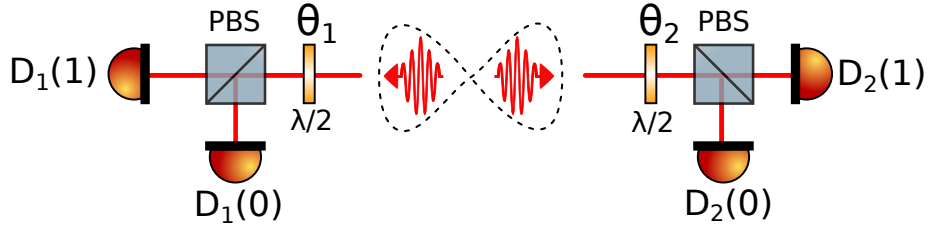


Figure 4.7: Bell experiment apparatus.

is each sent to an individual path containing a polarisation-resolving detector formed using a HWP and PBS with a single-photon detector in each output arm of the PBS as shown in fig. 4.7. The angle of the two HWPs is given by  $\theta_1$  and  $\theta_2$  as reflected in eq. (4.24). If the photon pair is an EPR pair in the photon polarisation basis the HWP configurations  $\theta_1 = 0^\circ$ ,  $\theta_2 = (\frac{22.5}{2})^\circ$ ,  $\theta'_1 = (\frac{45}{2})^\circ$  and  $\theta'_2 = (\frac{67.5}{2})^\circ$  will in theory violate the CHSH inequality in eq. (4.25) by yielding a theoretical value of  $S = 2\sqrt{2}$ .

## 4.6 Experimental results

The full experimental setup of the entanglement gate including the demultiplexed single photon source, as described in chapters 2 and 3 and the synchronisation electronics is presented in fig. 4.8

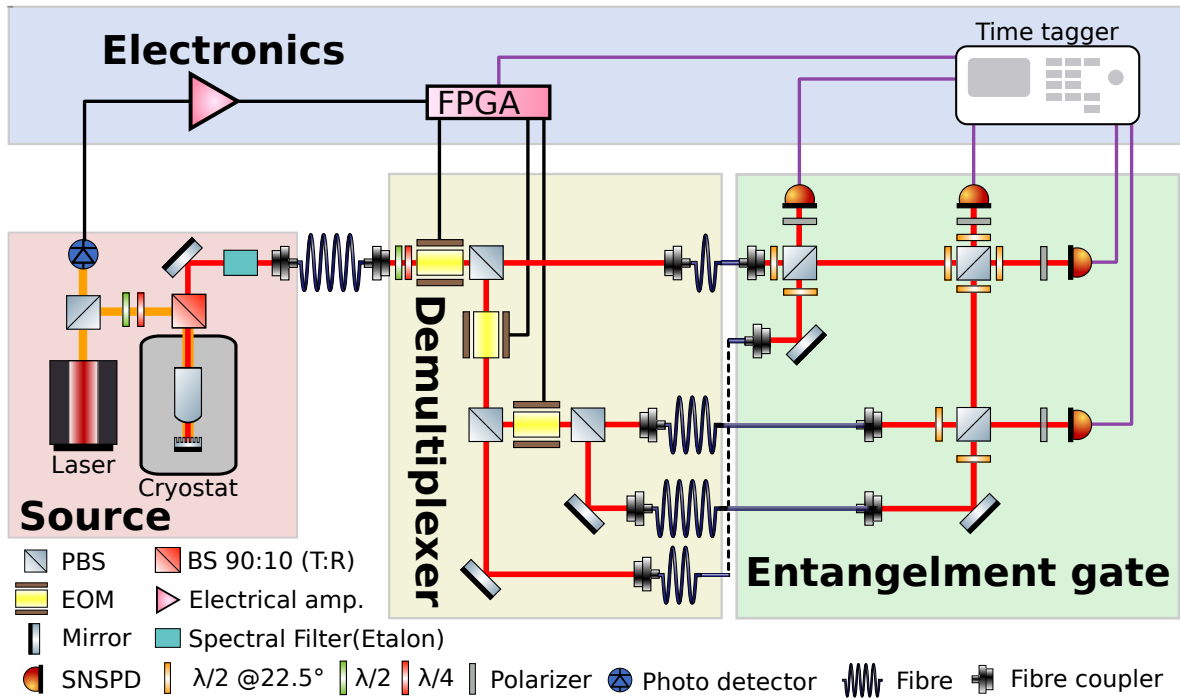


Figure 4.8: Schematic of the full experimental setup including the QD single photon source discussed in chapter 2, the demultiplexer discussed in chapter 3 and the electronics discussed in section 3.3.

The Bell experiment apparatus described in previous section (section 4.5) is already (intentionally) implemented in the heralded entanglement gate in fig. 4.1 on path  $B'$  and  $C'$ . Each of these

paths have a HWP followed by a fixed PBS with the transmitted output of the PBS coupled to a SNSPD. Due to a limited number of available detectors, we could not implement detection on the reflection arm of the PBS. We may instead add  $45^\circ$  to the HWP angle to rotate the projection axis by  $90^\circ$ , and thereby project along both the H-polarised and V-polarised basis states.

On the detection path  $A'$  and  $D'$  in fig. 4.1, two fixed PBS are implemented as seen in fig. 4.3. This projects the state upon measurement onto the horizontal polarisation axis. A coincident detection on path  $A'$  and  $D'$  thus implies that upon a subsequent joint detection on path on path  $B'$  and  $C'$  the measured state, in the ideal scenario, must be the maximally entangled Bell state  $\Psi_{B',C'}^+$  (c.f. eq. (4.7)).

When the heralded entanglement gate is spatially and temporally aligned, the source is operated according to chapter 2 at an excitation frequency of  $F_{ex} = 72.156\text{MHz}$  optimised to a single photon rate of  $3.8\text{MHz}$  and demultiplexed as described in chapter 3. The four-photon outputs are coupled to the entanglement gate which is set to herald on horizontal photon pairs on path  $A'$  and  $D'$ . The photon purity and indistinguishably presented in sections 2.4.1 and 2.4.2 is measured just prior to running the entanglement gate experiment.

With the source running the heralded entanglement gate is configured in  $(4 \times 12 =) 48$  different settings on path  $B'$  and  $C'$ , one at a time, to retrieve information about the state correlation and to evaluate the CHSH S-parameter. HWP3 in fig. 4.3 is set to  $\theta = \{0.0^\circ, 22.5^\circ, 45.0^\circ, 67.5^\circ\}$ , one at a time, while scanning HWP6 across  $\theta = 0^\circ \rightarrow 90^\circ$  in 12 discrete steps. The measurement for each HWP setting is run  $\sim 1.5$  hours while collecting time stamps on detector  $D1 - 4$ . Setup dedicated SNSPDs are used for detection and time stamps collected on a *quTAU* time tagger with time resolution of  $81\text{ps}$  [54] down sampled to a time bin size of  $486\text{ps}$ . After data acquisition the time stamps are intersected within a time window of  $1.458\text{ns}$  ( $= 3 \times \text{bin width}$ ), as visualised in the **green + red** area in fig. 4.9. This intersection is done for each of the 20 photon bins of the photon burst (see section 3.3.1). The intersection time window is chosen to include as many coincidences as possible, while rejecting most stray reflections of the pump laser in the source setup. This results in the four-fold coincidences presented in fig. 4.10, where the coincidences are marked in **red**, with uncertainties estimated by the square-root of coincidence counts  $\sqrt{N_{4F}}$ .

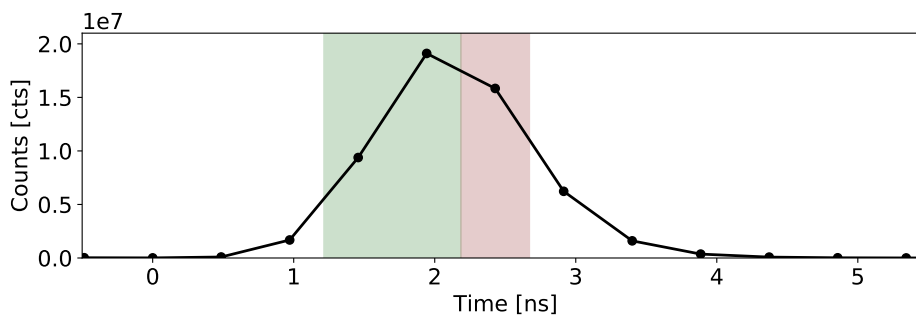


Figure 4.9: Photon arrival histogram of the first photon in the photon burst on detector  $D1$  during a measurement run in the  $\text{HWP3}=\text{HWP6}= 67.5$  configuration. The time axis has an arbitrary offset. The **green** fill en-capsules the two early time bins ( $972\text{ps}$ ) of the intersection time window. The **red** shaded en-capsules one time bin ( $486\text{ps}$ ) and the total shaded area en-capsules the full intersection time window ( $1.458\text{ns}$ ).

In fig. 4.10 the combined count rates on all four detectors are plotted in **green** on the right side y-axis, with respect to the HWP 3 waveplate settings. In all four count traces a periodic oscillation is visible which may be due to a  $\sim 1.5$  hour period temperature oscillation observed in the laboratory affecting the alignment of the source excitation laser. The total

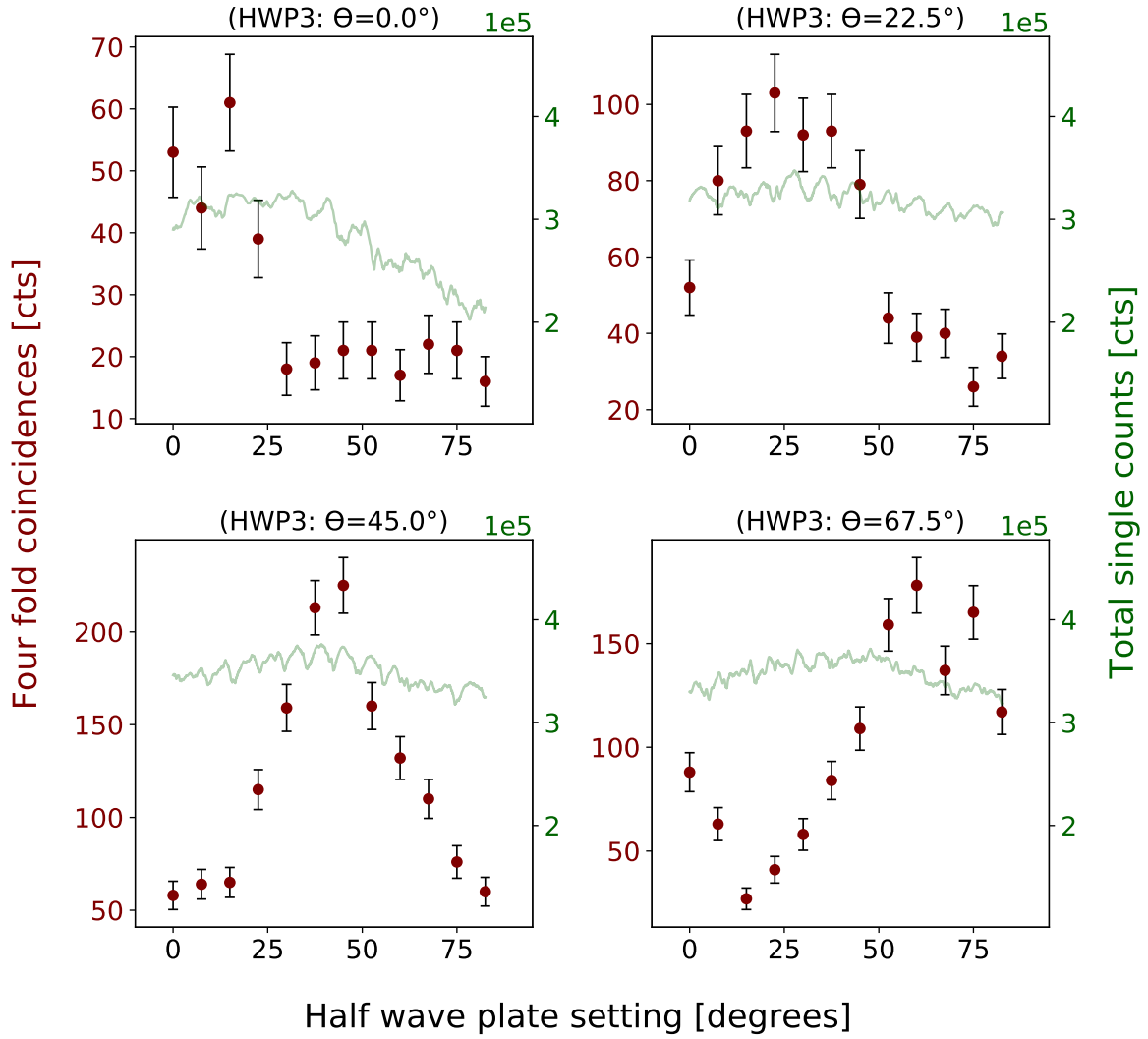


Figure 4.10: Raw four-fold coincidence counts with an intersection time window of three time bins (1.458ns) in red for each of the four HWP3 settings with respect to the HWP6 setting. The total counts across all four detectors is in the background plotted in green in order to give an insight in the source behaviour during each measurement setting.

count rate for HWP3 settings  $\{22.5^\circ, 45.0^\circ, 67.5^\circ\}$  is relatively constant over the period of the measurement. For HWP3 setting  $0.0^\circ$  a more pronounced decrease in counts occurs in the later half of the measurement. This occurred due to a spontaneous warm-up of the cryostat that causes a frequency shift of the QD emission frequency resulting in detuning with respect to the excitation laser. To account for difference in source efficiency, the four-fold coincidences are normalised with respect to the count rate of each detector and a rough estimate of the expected four fold coincidences. The normalisation factor is given by

$$N_{FF} = \sum_j \frac{4^3 S_{1j} S_{2j} S_{3j} S_{4j}}{f_{rep}^3}, \quad (4.28)$$

where  $S_{ij}$  is the number of counts per second in detector  $i$  in time interval  $j$ . The normalisation factor is individual for each HWP3 setting. The four-fold coincidences are next normalised

and fitted using  $\chi^2$ -regression fit routine[65]. The fit-model used is based on (4.27) and is given by:

$$f(\theta; A, \phi, f_0) = A \sin^2(2\theta - \phi) + f_0. \quad (4.29)$$

Here  $\theta$  is the HWP6 angle i.e.  $\theta_2$  in eq. (4.27), while  $\phi$  accounts for  $-2\theta_1$  and  $\delta_{ij}\pi/2$ , such that the expected  $\phi$ 's are  $-90^\circ$ ,  $45^\circ$ ,  $0^\circ$  and  $135^\circ$  for HWP3( $\theta_1$ ) setting  $0^\circ$ ,  $22.5^\circ$ ,  $45^\circ$  and  $67.5^\circ$ , respectively. The normalised data together with the fit-models is shown in fig. 4.11 and the fitted parameters summarised in table 4.6.

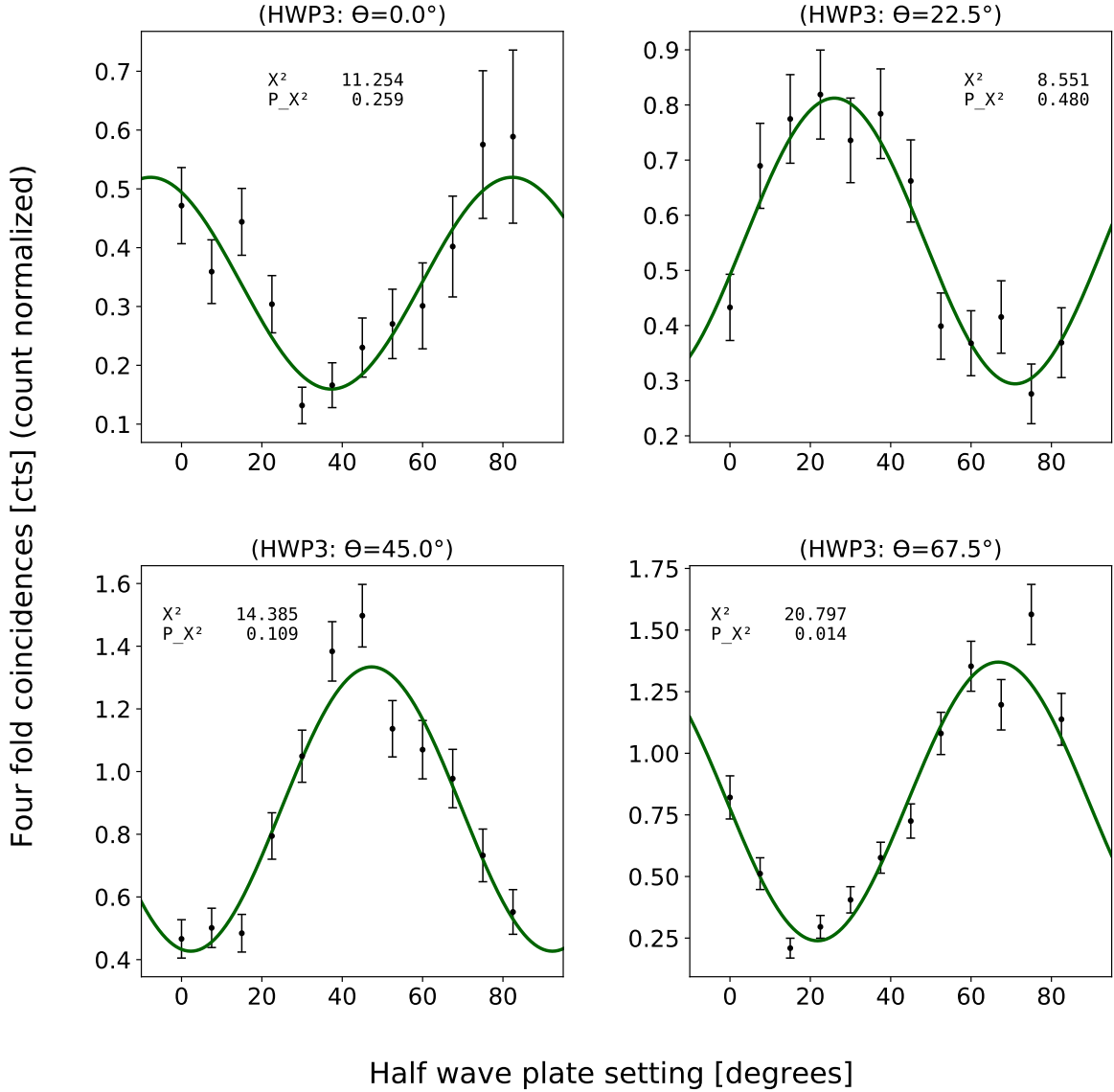


Figure 4.11: Normalised four-fold coincidences for an intersection time window of three time bins(1.458ns) marked with black dots, with the fit model shown in the green curve. The low  $P_{\chi^2}$  value of the fit in the HWP3  $67.5^\circ$  setting is most likely due to underestimation of errors.

The quantum correlations in eq. (4.25) are calculated by connecting the detection probability in eq. (4.26) to the respective measurement settings according to table 4.7. The detection probabilities are then calculated by the fit-model in eq. (4.29) using the respective fit pa-

Fit parameters	$A$	$\phi[deg^\circ]$	$f_0$	$\chi^2$	$P_{\chi^2}$	$V_P$
$\theta_{\text{HWP3}} = 0^\circ$	$0.36 \pm 0.05$	$(-74 \pm 4)^\circ$	$0.160 \pm 0.021$	11.254	0.259	53.0%
$\theta_{\text{HWP3}} = 22.5^\circ$	$0.52 \pm 0.06$	$(37.8 \pm 3)^\circ$	$0.294 \pm 0.030$	8.551	0.480	46.8%
$\theta_{\text{HWP3}} = 45^\circ$	$0.91 \pm 0.06$	$(-4.58 \pm 2)^\circ$	$0.43 \pm 0.03$	14.385	0.189	51.5%
$\theta_{\text{HWP3}} = 67.5^\circ$	$1.13 \pm 0.06$	$(136.5 \pm 1.5)^\circ$	$0.239 \pm 0.026$	20.797	0.014	70.3%

Table 4.6: Fit-parameters of the four-fold coincidence from fig. 4.11. The fit-modelling is in accordance with eq. (4.29). The number of degrees of freedom is in all fits  $N_{\text{dof}} = 9$ .  $V$  is the fringe visibility the fit-model.

rameters and normalised to 1/2. The procedure for calculating the  $\mathcal{P}_{ij}(\theta_1, \theta_2)$  values is here exemplified for  $i = j = 0$  and  $\theta_1 = 22.5^\circ$ :

$$\mathcal{P}_{00}(22.5^\circ, \theta_2) = \frac{1}{2} f(\theta_2 + 45^\circ; A, 135^\circ, f_0) \cdot \left( \frac{1}{A \cdot f_0} \right). \quad (4.30)$$

Here  $f$  is the fitfunction in eq. (4.29),  $A$  and  $f_0$  are the fitted parameters for setting HWP3=67.5°, and  $\phi$  is implemented as the theoretically expected value to compensate for disagreements between the noted HWP angle and the true angle of both HWP6 and HWP3. The error on  $\mathcal{P}_{ij}(\theta_1, \theta_2)$  is estimated assuming Poissonian statistics, by sweeping across the fit-provided co-variance matrix according to  $\sigma_f^2 = \sum_i^N \sum_j^N \frac{\partial f}{\partial x_i} \frac{\partial f}{\partial x_j} \text{cov}(x_i, x_j)$ .

Probability	Setting	
	HWP3	HWP6
$\mathcal{P}_{11}(0, \theta_2)$	$0.0^\circ$	$\theta_2$
$\mathcal{P}_{10}(0, \theta_2)$	$0.0^\circ$	$45^\circ + \theta_2$
$\mathcal{P}_{01}(0, \theta_2)$	$45.0^\circ$	$\theta_2$
$\mathcal{P}_{00}(0, \theta_2)$	$45.0^\circ$	$45^\circ + \theta_2$
$\mathcal{P}_{11}(22.5^\circ, \theta_2)$	$22.5^\circ$	$\theta_2$
$\mathcal{P}_{10}(22.5^\circ, \theta_2)$	$22.5^\circ$	$45^\circ + \theta_2$
$\mathcal{P}_{01}(22.5^\circ, \theta_2)$	$67.5^\circ$	$\theta_2$
$\mathcal{P}_{00}(22.5^\circ, \theta_2)$	$67.5^\circ$	$45^\circ + \theta_2$

Table 4.7: Connection between the detection probability in eq. (4.27) and the experimental configuration for four-fold coincidence acquisition.

The S-parameter is now calculated in accordance with eq. (4.24) and found to be maximised at  $\theta_2 = 11.71^\circ$  and  $\theta_2' = 33.32^\circ$ , which results in the quantum correlation parameters  $E(0.0^\circ, 11.71^\circ) = (0.47 \pm 0.05)$ ,  $E(0.0^\circ, 33.32^\circ) = (-0.47 \pm 0.04)$ ,  $E(22.5^\circ, 11.71^\circ) = (0.53 \pm 0.05)$  and  $E(22.5^\circ, 33.32^\circ) = (0.53 \pm 0.05)$  yielding an S parameter of

$$S = 2.01 \pm 0.10. \quad (4.31)$$

This is barely beyond the Bell inequality's classical limit of 2, though not within the standard deviation( $\sigma$ ). The error on S is propagated from the estimated errors on  $\mathcal{P}_{ij}$  according to the law of error propagation[44]. The fringe visibility of the quantum correlations do (c.f. section 1.2.1) have a lower bound for violating Bell's inequality. The observed visibility of

the fitted correlations were  $V_{E(22.5^\circ, \theta_2)} = 0.73 \pm 0.05$  and  $V_{E(0^\circ, \theta_2)} = 0.69 \pm 0.04$ .  $V_{E(22.5^\circ, \theta_2)}$  predicts a Bell violation within  $4\sigma$ . The low  $V_{E(0^\circ, \theta_2)}$ , is most likely due to cryostat warm-up that impacted the single-photon source quality during the measurement in the  $\text{HWP3} = 0^\circ$  measurement setting.

Several factors may have limited the quantum correlation visibility in the prented measurements: *firstly* the total single detector counts on the path including the rotating HWP3 varied during measurements as seen in fig. 4.12. This is maybe due to polarisation-dependent fibre-coupling efficiency on arm  $D$  when rotating HWP3. As the HWP3 sits between two linear polarisers (PBSs), wavefront distortions (due to the isogyre pattern of the birefringent crystal that form the HWP) could occur when the waveplate is rotated such that the light from one PBS is cross-polarized with respect to the PBS in front of the detector fibre. This results in a mode-mismatch at the single-mode fibre resulting in a lower collection efficiency. We observe that it is relatively pronounced with a  $\sim 30\%$  variation as seen on detector D4 in fig. 4.12.

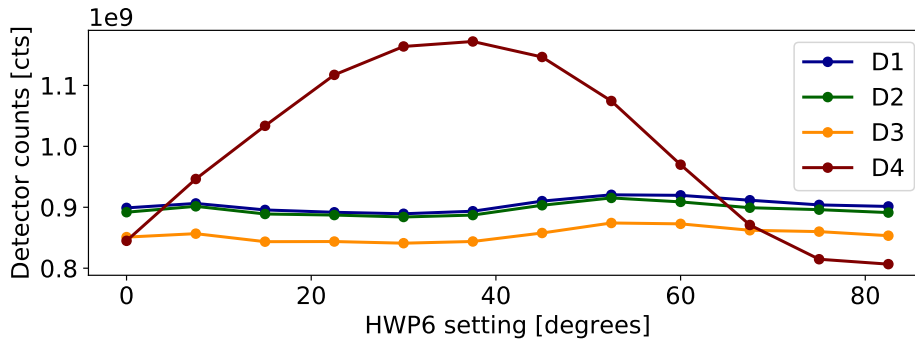


Figure 4.12: Total counts for each of the four detectors in measurement configuration  $\text{HWP3} = 45.0^\circ$ , with respect to the respective HWP6 setting.

*Secondly* the visibility of the coincidence probability  $V_P$  given in table 4.6 is highly sensitive to erroneous four-fold coincidences that may occur due to laser impurities or low HOM visibility of the single-photon source. The laser impurities are more likely to occur at longer times (with respect to pulse arrival time on the sample) due to reflections in the source setup. In the context of a DIQKD CHSH central heralding station, theoretical analysis presented in [66] explores the photon indistinguishability's impact on the obtainable order of Bell inequality violation. It is shown here that a  $V_{\text{HOM}} \approx 79\%$  for identical indistinguishability of the correlated photons, sets a lower threshold for violation of Bell's inequality. The setup analysed here is in great resemblance to the heralded entanglement gate presented in this chapter. As shown in section 3.6, the indistinguishability of the demultiplexed photons is well above this threshold, why a violation of Bell's inequality is feasible, but does imply a violation upper bound.

*Thirdly* as discussed in section 3.6 and seen in fig. 3.7, a detector correlation artefact is observed on the SNSPDs. As the same detection setup is used for the entanglement gate experiment, the presence of this artefact must be anticipated. We typically observe that the correlation noise was pronounced at non-zero time delays between two photons. The detector correlation noise can result in false four-fold coincidences, which is especially critical when the quantum correlation is expected to suppress four-fold coincidences.



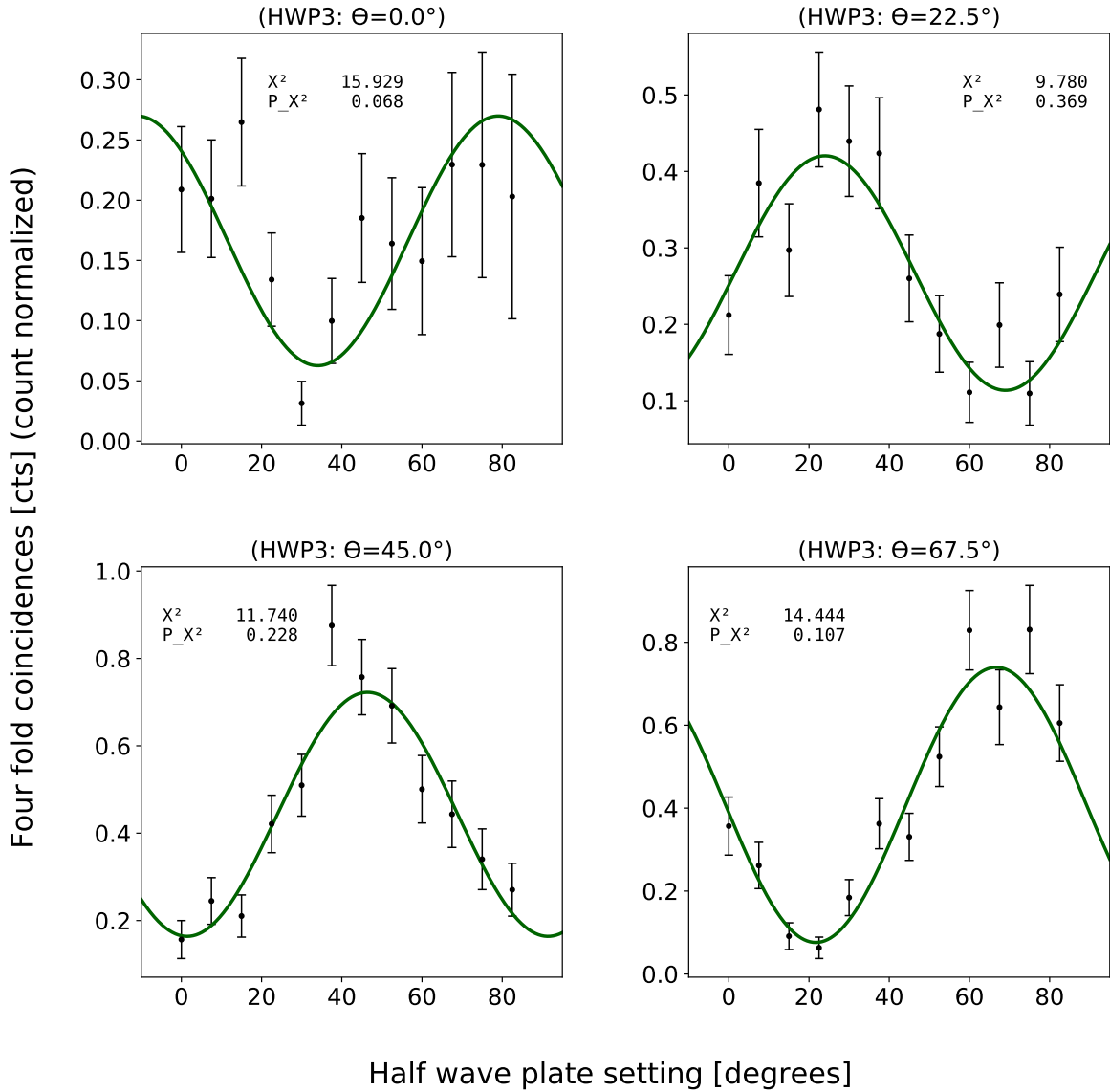


Figure 4.13: Normalised four-fold coincidences for an intersection time window of the two early time bins(972ps) marked with black dots with the fit model shown in the green curve.

With the objective of minimising the impact of the detector correlation artefact and laser impurity we test if shortening the measurement intersection time window to two time bins(972ps), that include the central bin and early side bin of the photon arrival histogram as visualised in green in fig. 4.9, improves the visibility. This data analysis is shown in fig. 4.13 and the corresponding fit-parameters presented in table 4.8. Here we see a vast improvement in the coincidence fringe visibility  $V_P$  and the resulting S parameter is

$$S = 2.24 \pm 0.08, \quad (4.32)$$

which is a violation of Bell's inequality of  $3\sigma$ . The quantum correlation fringe visibility  $V_{E(22.5^\circ, \theta_2)} = 0.813 \pm 0.008$  predicts a Bell inequality violation of  $S = 2.30 \pm 0.02$  i.e. a violation of  $15\sigma$ . In the data set for the HWP3=  $0^\circ$  configuration, however there seems to be a lack of tendency. This may be attributed to the cryostat warming up, leading to a fit p-value just above the standardised significance level of 5%.

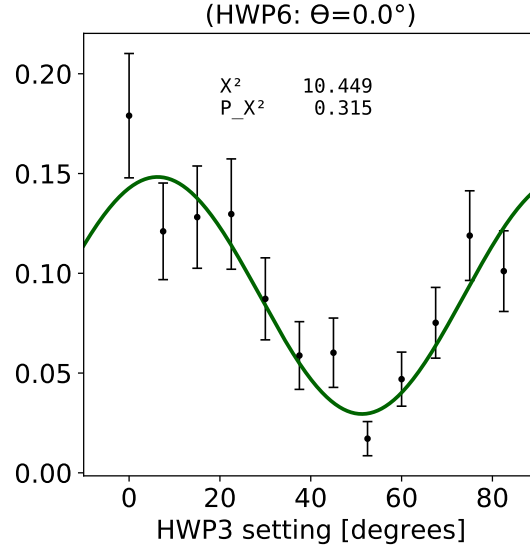


Figure 4.14: Normalised four-fold coincidences of a previous measurement marked in black dots. Intersection time window is here three time bins(1.458ns). The fit is shown as a green curve.

We could confirm this anomaly of the  $\text{HWP3}=0^\circ$  measurement using data from a previous run. Previous to the entanglement gate experiment, another measurement run on the setup was executed, keeping HWP6 constant at  $\theta = 0^\circ$  while altering HWP3 from  $0^\circ \rightarrow 90^\circ$  (i.e. reversed HWP roles), with an integration time of  $\sim 20$  minutes. The acquired normalised data-set with a three-bin intersection time window is presented in fig. 4.14. Due to symmetry in the entanglement gate and symmetry in the Bell state on path  $B'$  and  $C'$ , this data is identical to the  $\text{HWP3}=0^\circ$  data set.

Using this measurement run in the data analysis yields a slight increase in CHSH parameter for three-time-bin intersection window:  $S = 2.08 \pm 0.10$ , though still not a violation of Bell's inequality within the estimated uncertainty. All data analysis variations and the corresponding quantum correlation fringe visibility and S-parameter is presented in table 4.9

Fit parameters	$A$	$\phi[\text{deg}^\circ]$	$f_0$	$\chi^2$	$P_{\chi^2}$	$V_P$
$\theta_{\text{HWP6}} = 0.0^\circ$	$0.21 \pm 0.06$	$(-68 \pm 6)^\circ$	$0.063 \pm 0.015$	15.929	0.068	62.3%
$\theta_{\text{HWP6}} = 22.5^\circ$	$0.31 \pm 0.05$	$(42 \pm 4)^\circ$	$0.11 \pm 0.02$	9.780	0.379	57.4%
$\theta_{\text{HWP6}} = 45.0^\circ$	$0.56 \pm 0.05$	$(-3 \pm 3)^\circ$	$0.16 \pm 0.03$	11.740	0.228	63.0%
$\theta_{\text{HWP6}} = 67.5^\circ$	$0.66 \pm 0.05$	$(137 \pm 2)^\circ$	$0.076 \pm 0.018$	14.444	0.107	81.4%

Table 4.8: Fit-parameters of the four-fold coincidence from fig. 4.14. The fit-modelling is in accordance with eq. (4.29). The number of degrees of freedom is in all fits  $N_{dof} = 9$ .  $V_P$  is the fringe visibility the fit-model.

Data	# Bins	$\phi$	$V_{E(0^\circ, \theta_2)}$	$V_{E(22.5^\circ, \theta_2)}$	S
Original	3	F	$0.64 \pm 0.04$	$0.72 \pm 0.05$	$1.92 \pm 0.10$
		T	$0.69 \pm 0.04$	$0.73 \pm 0.05$	$2.01 \pm 0.10$
	2	F	$0.70 \pm 0.03$	$0.811 \pm 0.007$	$2.11 \pm 0.08$
		T	$0.77 \pm 0.04$	$0.813 \pm 0.008$	$2.24 \pm 0.08$
Alternative	3	F	$0.73 \pm 0.04$	$0.72 \pm 0.05$	$2.05 \pm 0.10$
		T	$0.74 \pm 0.04$	$0.73 \pm 0.05$	$2.08 \pm 0.10$
	2	F	$0.675 \pm 0.007$	$0.811 \pm 0.007$	$2.11 \pm 0.010$
		T	$0.676 \pm 0.015$	$0.813 \pm 0.008$	$2.11 \pm 0.010$

Table 4.9: The collected S parameters and quantum correlation fringe visibilities for different data analysis strategies. ‘Data’ column distinguished between the original data set and the alternative, using the HWP $6\theta = 0^\circ$  measurement from a previous run. The ‘# Bins’ column states the intersection window size where 2 is  $2 \times$  time-Bin depicted in green in fig. 4.9 and 3 is  $3 \times$  time bin depicted in green+red. The time bin size is = 486ps. The  $\phi$  column distinguishes between using the Fitted or Theoretically expected  $\phi$  value in the S parameter calculation. Two bin with theoretical  $\phi$  predicts a Bell inequality violation within 15 sigma of  $S = 2.30 \pm 0.02$  and delivers a fundamental evidence of quantum correlations.

## 4.7 Summary

This chapter introduced a setup for heralded photon entanglement generation that can be employed as the source in a DIQKD scheme. The heralding efficiency of the experimental implementation can in the ideal case reach  $P_s = 32.0\%$ , but feasible setup improvements in the form of four photon-number-resolving detectors indicates a heralding efficiency of unity in the ideal case. The experimentally achieved CHSH S-parameter of the heralded entangled state is  $S = 2.01 \pm 0.10$  for a 1.458ns coincidence intersection time window, and for a more narrow time window of 972ps we reach  $S = 2.24 \pm 0.08$ . The quantum correlation fringe visibility achieved predicts a violation of Bell’s inequality within  $15\sigma$ , i.e  $S = 2.30 \pm 0.02$ .

---

## Chapter 5

# Metasurface design proposal for partial Bell state measurement

---

A key component in DIQKD is a heralding station(HS). A brief example of the HS working principle is: Alice and Bob each have a pair of polarisation orthogonal photons. They each send one of the photons, chosen randomly, to the HS, which then performs a partial Bell state measurement, as will be described in section 5.1, on the received photon pair. This measurement will according to certain conditions execute entanglement swapping leaving the two photons that stayed with Alice and Bob in an entangled state[30]. A partial Bell state measurement setup is usually constructed from a beam splitter and two PBSs. However, advances in holographic media, micro and nanofabration in the last few decades, have enabled the practical realisation of optical elements with tailored spatially varying polarisation properties, even on sub-wavelength scale and at optical frequencies[67]. These devices consists of polarisation gratings in which the polarisation state of light can be varied controllably, point to point across an optical element by engineered polarisation-dependent diffraction. A highly convenient medium for realisation of such diffraction gratings are the engineered ultra-thin planar devices referred to as *metasurfaces*[68, 69]. These materials consists of sub-wavelength-spaced arrays of nano-photon phase shifters, composed of dielectric pillars that possess form birefringence[16, 68]. Non-classical multi-photon interferences with single metasurface have been demonstrated with fidelity estimations  $> 95\%$ [70] and  $> 96.5\%$ [71] between predicted and reconstructed density matrices. In this section a proposal for implementing a Bell state measurement design based on metasurfaces as described by [67] is presented. We begin this chapter with an introduction to the partial Bell state measurement, followed by an introduction to the metasurface operational properties and design strategies and end with a proposal for a new design for metasurface based partial Bell state measurements.

### 5.1 Partial Bell state measurement

With a partial bell state measurement we can discriminate between the four two-mode entangled Bell states. Depending on measurement outcome we can distinguish between the states  $|\Psi^+\rangle$ ,  $|\Psi^-\rangle$  and  $|\Phi^\pm\rangle$ (i.e. the measurement outcome is not able to distinguish between the two  $|\Phi^-\rangle$  and  $|\Phi^+\rangle$  states). The traditional setup for a partial Bell state measurement is schematically presented in fig. 5.1. This setup consists of three optical elements a BS and two

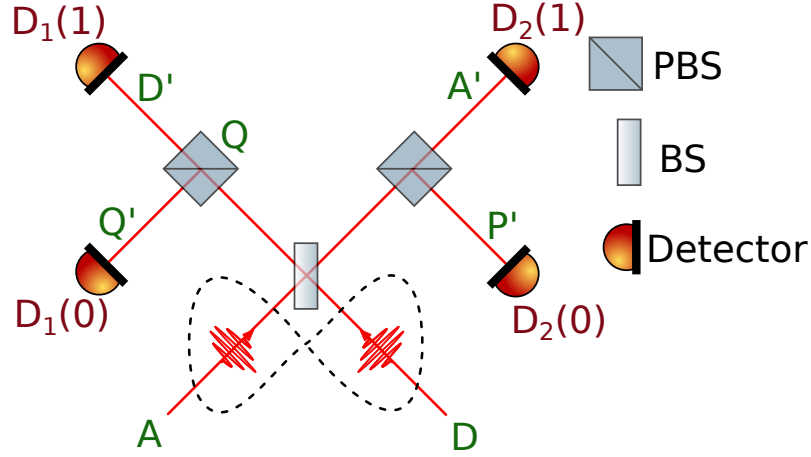


Figure 5.1: Schematic of a partial Bell state measurement. Here the green notations are spatial photon modes, red are detectors.

PBSs. For the spatial input modes  $A, D, P, Q$  and output modes  $A', D', P', Q'$  in fig. 5.1 the transformation matrices of the optical elements in the ideal scenario is given in appendix A.2. Combining all three optical elements the overall ideal transformation matrix of the partial Bell state measurement reads:

$$\text{Partial Bell : } \begin{pmatrix} \hat{a}'_H \\ \hat{p}'_V \\ \hat{d}'_H \\ \hat{q}'_V \end{pmatrix} = \frac{1}{\sqrt{2}} \begin{bmatrix} 1 & 0 & i & 0 \\ 0 & i & 0 & -1 \\ i & 0 & 1 & 0 \\ 0 & -1 & 0 & i \end{bmatrix} \begin{pmatrix} \hat{a}_H \\ \hat{a}_V \\ \hat{d}_H \\ \hat{d}_V \end{pmatrix}. \quad (5.1)$$

Here  $\hat{a}'_H(\hat{p}'_V)$  is the creation operator of a horizontal(vertical) polarised photon in the  $A'(P')$  spatial mode and so on. Applying the transformation matrix to the Bell state  $|\Psi^-\rangle = 1/\sqrt{2}(\hat{a}_H^\dagger \hat{d}_V^\dagger - \hat{a}_V^\dagger \hat{d}_H^\dagger)|0\rangle$  will result in the following state evolution:

$$|\Psi^-\rangle = 1/\sqrt{2}(\hat{a}_H^\dagger \hat{d}_V^\dagger - \hat{a}_V^\dagger \hat{d}_H^\dagger)|0\rangle \quad (5.2a)$$

$$\begin{aligned} & \downarrow \text{Partial Bell state measurement} \\ & = \frac{1}{2\sqrt{2}} \left[ (\hat{a}'_H + i\hat{d}'_H)(i\hat{q}'_V - \hat{p}'_V) - (i\hat{p}'_V - \hat{q}'_V)(i\hat{a}'_H + \hat{d}'_H) \right] |0\rangle \end{aligned} \quad (5.2b)$$

$$\begin{aligned} & = \frac{1}{2\sqrt{2}} \left[ i\hat{a}'_H \hat{q}'_V - \hat{a}'_H \hat{a}'_P + i^2 \hat{d}'_H \hat{q}'_V - i\hat{d}'_H \hat{p}'_V \right. \\ & \quad \left. - i^2 \hat{p}'_V \hat{q}'_V - i\hat{p}'_V \hat{d}'_H + i\hat{q}'_V \hat{a}'_H + \hat{d}'_H \hat{q}'_V \right] |0\rangle \end{aligned} \quad (5.2c)$$

$$= \frac{1}{\sqrt{2}} \left[ i\hat{a}'_H \hat{q}'_V - i\hat{d}'_H \hat{p}'_V \right] |0\rangle \quad (5.2d)$$

$$= \frac{i}{\sqrt{2}} \left( |HV\rangle_{A'Q'} - |HV\rangle_{D'P'} \right), \quad (5.2e)$$

where the creation operators has been applied to the vacuum state in eq. (5.2e). The interference terms may be eliminated according to the bosonic commutation relations in eq. (1.5).

This state evolution outlines that when the Bell state  $\Psi^-$  is incident, it will result in a coincident detection on either  $D_1(0)\&D_2(1)$  or  $D_1(1)\&D_2(0)$ . Here the detector(D) subscript refers to the detectors and the outcome of the measurement is indicated in the parenthesis. Evolving the other three Bell states results in the states just before detection of  $|\Psi^+\rangle \rightarrow -1/\sqrt{2}(|HV\rangle_{A'P'} + |HV\rangle_{D'Q'})$  i.e.  $|\Psi^+\rangle$  is distinguished by a coincident detection on  $D_1(0)\&D_1(1)$  or  $D_2(0)\&D_2(1)$  and  $|\Phi^\pm\rangle \rightarrow i/2(|HH\rangle_{A'A'} + |HH\rangle_{D'D'} \mp |VV\rangle_{P'P'} \mp |VV\rangle_{Q'Q'})$  i.e.  $|\Phi^\pm\rangle$  are distinguished on a two photon detection in either of the four detectors.

## 5.2 Metasurfaces

Metasurfaces as proposed and demonstrated on classical light[68, 67], may be a viable component to realise complex linear optical operations on a single thin film within quantum optics and photonics. Light encountering a metasurface diffraction grating will split into a finite number of diffraction orders due to the gratings periodical variation with space. The diffraction orders may be engineered to work as polarisation dependent beamsplitters with an arbitrary phase constant. This capability to implement linear operations in a thin-film reduces optical loss from absorption, hence offering a new device platform for quantum information processing. Furthermore, by programming the flexure in the thin film, it is possible to reprogram the linear operation as well [72]. The metasurfaces are modelled in a matrix modification of Fourier optics referred to as Matrix Fourier optics[67].

### 5.2.1 Matrix Fourier optics

In the plane-wave expansion picture of optics an electromagnetic field  $E(x, y)$  is formed from the interference of infinite many plane-waves incident at different angles. Individual plane-waves in this set are characterised by their in-plane wave-vector  $(k_x, k_y)$  and a weight( $A(k_x, k_y)$ ) given by the Fourier transform of the optical field:

$$A(k_x, k_y) = \iint_{-\infty}^{+\infty} E(x, y) e^{i(k_x x + k_y y)} dx dy. \quad (5.3)$$

The field at different positions in space can then be modelled by propagating each individual plane wave with its weight  $A(k_x, k_y)$  to the desired spatial position. This formalism, in its original form[73], does not include polarisation information of the electromagnetic field. This information is however included in the matrix Fourier optics formalism introduced by [67]. By describing the electromagnetic field in the Jones vector formalism as  $|E(x, y)\rangle = \tilde{J}(x, y) |E_0\rangle$ , assuming that the field is a normal incident uniform plane-wave, the space-dependence can be removed such that the integral in eq. (5.3) can be rewritten as:

$$\tilde{A}(k_x, k_y) = \iint_{-\infty}^{+\infty} \tilde{J}(x, y) e^{i(k_x x + k_y y)} dx dy, \quad (5.4)$$

where the tilde denotes a Jones matrix quantity. Here the Jones matrix Fourier series  $\tilde{J}(x, y)$  will be given by the matrix Fourier coefficient  $\tilde{J}_k$  summed over a specified(desired) set of diffraction orders  $(m, n) \in \{\ell\}$ :

$$\tilde{J}(x, y) = \sum_{(m,n) \in \{\ell\}} \tilde{J}_{(m,n)} e^{i(k_x x + k_y y)}. \quad (5.5)$$

A diffraction order  $(m, n)$  behaving as a polariser can be described by a Jones matrix that is a weighted dyadic(outer product) of the polarisation of interest expressed as a Jones vector:

$$\tilde{J}_{(m,n)} = c_k |p_{(m,n)}^*\rangle \langle p_{(m,n)}|. \quad (5.6)$$

Here  $c_{(m,n)}$  is a complex(scalar-valued) weight given by  $c_{(m,n)} = a_{(m,n)} e^{i\phi_{(m,n)}}$ . This describes a Jones matrix analysing for the chosen Jones vector  $|p_{(m,n)}\rangle$  in accordance with Malu's law. I.e., If the orthogonal polarisation is incident ( $|q_{(m,n)}^\perp\rangle$ ) the output light is quenched. The light emerging from the  $\tilde{J}_{(m,n)}$  analysing order will carry the polarisation state  $|p_{(m,n)}\rangle$  [67]. There are specific restrictions when working with metasurfaces in this formalism e.g. local linear birefringance is required for metasurfaces which implies the symmetry of the Jones vector(adjunct) in eq. (5.6). As a result the output polarisation of each analyser(diffraction order) is the complex conjugate of the Jones vector being analysed for, equivalent to a mirroring about the equatorial plane of the Poincaré sphere.

The optical power (normalised to the incident power) on order  $(m, n)$  with its preferred polarisation  $|q_{(m,n)}\rangle$  is given by

$$I_q^{(m,n)} = \langle q_{(m,n)} | \tilde{J}_{(m,n)}^\dagger \tilde{J}_{(m,n)} | q_{(m,n)} \rangle, \quad (5.7)$$

and the optical power when the orthogonal polarisation  $|q_{(m,n)}^\perp\rangle$  is incident is  $I_{q^\perp}^{(m,n)} = \langle q_{(m,n)}^\perp | \tilde{J}_{(m,n)}^\dagger \tilde{J}_{(m,n)} | q_{(m,n)}^\perp \rangle$ . These two measures give rise to the diffraction order contrast:

$$\eta_c = \frac{I_q^k - I_{q^\perp}^k}{I_q^k + I_{q^\perp}^k}. \quad (5.8)$$

The diffraction order optical power and contrast are entities used to quantify the efficiency of each diffraction order, and are key parameters when designing the metasurface. The metasurface optimisation is based on optimisation through gradient descent. First step in the metasurface design phase is specifying the number of desired orders  $\{\ell\}$  and their respective polarisation analysis  $|q_{m,n}\rangle$ . Then a random metasurface design is chosen  $\tilde{J}(x, y)$  defining the linearly birefringent wave-plate at each discrete point of the metasurface. By calculating the Fourier matrix coefficient in eq. (5.4) the Fourier Jones matrix coefficient can be evaluated as  $\tilde{J}(k_x, k_y) = \frac{1}{2\pi} \tilde{A}(k_x, k_y)$ , where  $k_x$  and  $k_y$  can be parameterized by integer indices of  $m$  and  $n$  in order to find the matrix Fourier coefficient  $\tilde{J}(m, n)$  for any diffraction order  $(m, n)$ . The optical power of each diffraction order and diffraction order contrast is then evaluated and based on these evaluations a new design for  $\tilde{J}(x, y)$  is chosen. This process is cyclic, and the new design for each cycle is picked from a library of elements chosen through gradient descent. The process is continued until the diffraction order intensity power and contrast converges. The demonstrated diffraction order contrast in [67] is  $> 90\%$  for six diffraction orders and  $> 92\%$  for four, but reaching up to  $99\%$  for individual orders.

### 5.3 Metasurface partial Bell state measurement

To design a metasurface grating that can conduct a partial Bell state measurement, it must do linear operations on the two incident spatial modes in accordance with eq. (5.1). In order to simplify the phase operations of the gratings, we may realise that the two  $\pi$  phase operations in eq. (5.1) are not strictly necessary in order to distinguish Bell states. Removing these will simply swap the detection coincidences distinguishing the  $|\Psi^+\rangle$  and  $|\Psi^-\rangle$  Bell states. Hence we may write an alternative partial Bell state measurement transformation matrix as

$$\text{Partial Bell : } \begin{pmatrix} \hat{a}'_H \\ \hat{p}'_V \\ \hat{d}'_H \\ \hat{q}'_V \end{pmatrix} = \begin{pmatrix} \hat{\alpha}'_{(1,0),H} \\ \hat{\alpha}'_{(0,1),V} \\ \hat{\alpha}'_{(-1,0),H} \\ \hat{\alpha}'_{(0,-1),V} \end{pmatrix} = \frac{1}{\sqrt{2}} \begin{pmatrix} 1 & 0 & i & 0 \\ 0 & i & 0 & 1 \\ i & 0 & 1 & 0 \\ 0 & 1 & 0 & i \end{pmatrix} \begin{pmatrix} \hat{a}'_H \\ \hat{a}'_V \\ \hat{d}'_H \\ \hat{d}'_V \end{pmatrix}, \quad (5.9)$$

where the columns highlighted in green operate on spatial mode  $A$  and the red columns operate on  $D$ . The output relations of the partial Bell measurement transformation matrix in eq. (5.1) are mapped onto the metasurface diffraction orders as

$$\{\ell\} \in \{(1,0), (0,1), (-1,0), (0,-1)\} \Leftrightarrow \{\hat{a}'_H, \hat{p}'_V, \hat{d}'_H, \hat{q}'_V\}, \quad (5.10)$$

where  $\hat{\alpha}'_{(m,n),j}$  is the creation operator of a photon in the  $(m,n)$  diffraction order with polarisation  $j \in \{H, V\}$ . From this transformation matrix we can design the four diffraction orders, by analysing for the Jones vectors  $|p_{(1,0)}\rangle = |p_{(-1,0)}\rangle = |H\rangle$  and  $|p_{(0,1)}\rangle = |p_{(0,-1)}\rangle = |V\rangle$ . In terms of quantum interference an important element in the transformation matrix in eq. (5.1), is the difference in phase alteration of the two incident spatial modes. To accommodate this a setup design with two independent metasurface gratings placed just next to each other as illustrated in fig. 5.2a is chosen, each with diffraction orders as depicted in fig. 5.2b. Here the arrow direction refers to the polarisation orientation of the Jones vector being analysed for in the respective diffraction order. The light diffracted by the metasurface transmits through a 2f Fourier imaging setup to overlap the identical diffraction orders of the two metasurfaces. Lastly to imitate the linear operations of a beamsplitter as in the original Bell measurement setup in fig. 5.1, horizontal and vertical polarised light are each split in to two diffraction orders with equal probability. The Jones matrix defining each diffraction order is outlined in table 5.1

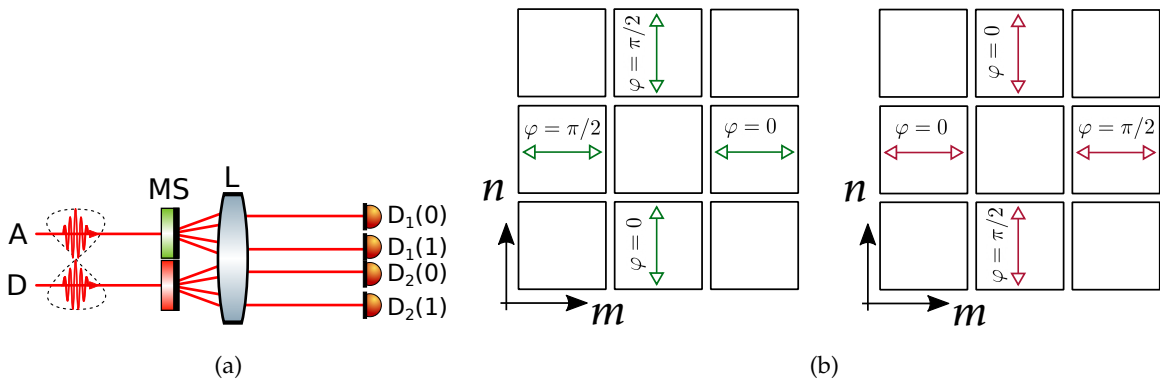


Figure 5.2: Proposed metasurface design for a partial Bell state measurement. **(a)** Experimental implementation of the metasurface partial Bell state measurement. MS indicates the metasurfaces and L indicates a 2f Fourier imaging setup. **(b)** schematic overview of the diffraction polarisation analysing orders. The arrows indicate the the linear polarisation basis being analysed for in the respective order.  $\phi$  indicates the phase alteration of the diffraction order. The left design operates on spatial mode  $A$  and the right on mode  $D$ . Each diffraction order carry an  $a = 1/2$  not noted in the figure leading to the Jones matrix weight of each diffraction order  $c_{(m,n)} = \frac{1}{2}e^{i\phi_{(m,n)}}$ .



$(m, n)$	(1,0)	(0,1)	(-1,0)	(0,-1)
A	$\tilde{J}_{(m,n)} = \frac{1}{\sqrt{2}}  V\rangle \langle V $	$\tilde{J}_{(m,n)} = i \frac{1}{\sqrt{2}}  H\rangle \langle H $	$\tilde{J}_{(m,n)} = i \frac{1}{\sqrt{2}}  V\rangle \langle V $	$\tilde{J}_{(m,n)} = \frac{1}{\sqrt{2}}  H\rangle \langle H $
D	$\tilde{J}_{(m,n)} = i \frac{1}{\sqrt{2}}  V\rangle \langle V $	$\tilde{J}_{(m,n)} = \frac{1}{\sqrt{2}}  H\rangle \langle H $	$\tilde{J}_{(m,n)} = \frac{1}{\sqrt{2}}  V\rangle \langle V $	$\tilde{J}_{(m,n)} = i \frac{1}{\sqrt{2}}  H\rangle \langle H $

Table 5.1: Jones matrices of the metasurface diffraction orders. The green column refers to the metasurface operating on the spatial input mode  $A$  and the red refers to the metasurface operating on spatial input mode  $D$ .

The transformation matrix of the designed metasurface setup, modelled with defects, is shown in appendix A.3. Here a perfect temporal and spatial overlap after the 2f Fourier imaging setup is assumed. For simplicity we also assume that all orders have the same defects. e.g. the splitting ratio between identical polarisation analysers are assumed equal for all pairs of polarisation analysing diffraction orders etc.

For two pure states the fidelity is given by  $F = |\langle \psi_{ideal} | \psi \rangle|^2 = \langle \psi_{ideal} | \psi \rangle \langle \psi | \psi_{ideal} \rangle$ , where  $|\psi\rangle$  is the experimental obtainable state, while  $|\psi_{ideal}\rangle$  is the ideal scenario. For  $|\Psi^-\rangle$  these two are after the transformation of eq. (5.9) and eq. (A.4) respectively given by:

$$|\psi_{ideal}\rangle = \frac{1}{\sqrt{2}} \left( \hat{\alpha}_{(1,0),H}^\dagger \hat{\alpha}_{(0,1),V}^\dagger - \hat{\alpha}_{(-1,0),H}^\dagger \hat{\alpha}_{(0,-1),V}^\dagger \right) |0\rangle, \quad (5.11)$$

$$|\psi\rangle = \frac{1}{\sqrt{2}} \eta_L \eta_C \sqrt{V} \left( \hat{\alpha}_{(1,0),H}^\dagger \hat{\alpha}_{(0,1),V}^\dagger \eta_S \left[ e^{i2\phi_0} - e^{i2\phi_1} \right] \eta_S \right. \\ \left. + \hat{\alpha}_{(-1,0),H}^\dagger \hat{\alpha}_{(0,-1),V}^\dagger \left[ e^{i2\phi_1} - e^{i2\phi_0} \right] (1 - \eta_S) \right). \quad (5.12)$$

In the experimental obtainable output state only the terms that can result in non-zero values due to the orthogonality of the Hilbert space, when overlapped with the ideal state, has been included for simplicity. Now evaluating the fidelity:

$$F_{|\Psi^-\rangle} = \frac{1}{2} \eta_L \eta_C \sqrt{V} \langle 0 | \left( \hat{\alpha}_{(1,0),H}^\dagger \hat{\alpha}_{(0,1),V}^\dagger - \hat{\alpha}_{(-1,0),H}^\dagger \hat{\alpha}_{(0,-1),V}^\dagger \right) \\ \times \left( \hat{\alpha}_{(1,0),H}^\dagger \hat{\alpha}_{(0,1),V}^\dagger \left[ e^{i2\phi_0} - e^{i2\phi_1} \right] \eta_S + \hat{\alpha}_{(-1,0),H}^\dagger \hat{\alpha}_{(0,-1),V}^\dagger \left[ e^{i2\phi_1} - e^{i2\phi_0} \right] (1 - \eta_S) \right) |0\rangle \times \text{h.c.} \\ = \frac{1}{4} \eta_L^2 \eta_C^2 V \left( \left[ e^{i2\phi_0} - e^{i2\phi_1} \right] \eta_S - \left[ e^{i2\phi_1} - e^{i2\phi_0} \right] (1 - \eta_S) \right) \\ \times \left( \left[ e^{-i2\phi_0} - e^{-i2\phi_1} \right] \eta_S - \left[ e^{-i2\phi_1} - e^{-i2\phi_0} \right] (1 - \eta_S) \right) \\ = \frac{1}{4} \eta_L^2 \eta_C^2 V \left( e^{-i2\phi_0} - e^{-i2\phi_1} \right) \left( e^{i2\phi_0} - e^{i2\phi_1} \right) \\ = \eta_L^2 \eta_C^2 V \sin^2(\Delta\phi), \quad (5.13)$$

where  $\Delta\phi = \phi_1 - \phi_0$ . In the same manor the fidelity for input state  $|\Psi^+\rangle$  and  $|\Phi^\pm\rangle$  is evaluated resulting in:  $F_{|\Psi^+\rangle} = 4\eta_L^2 \eta_C^2 V (\eta_S - \eta_S^2)$  i.e. not dependent on the phase difference of the diffraction orders, but on the splitting ratio, and  $F_{|\Phi^\pm\rangle} = \eta_L^2 \eta_C^2 V$  i.e. dependent on neither the phase or splitting ratio. All fidelity estimations are visualised in fig. 5.3a with respect to the splitting ratio and the phase difference in the lossless scenario i.e.  $\eta_L = 1$ , and with diffraction order contrast  $\eta_C = 92\%$ , as demonstrated lower bound[67], and a photon indistinguishability  $V = 92.8\%$ , as measured in section 2.4.2, reaching a maximal fidelity of  $F = 78.5\%$ . In fig. 5.3b the fidelity estimations are presented for a diffraction order contrast of  $\eta_C \sim 99\%$ , which is reached for two out of four diffraction orders in[67], and a photon indistinguishability of 96%, as demonstrated on a QD single photon source platform in [39] similar to the one in this thesis. The resulting fidelity for alle three input Bell states reaches a maximum value of  $F = 94.1\%$ .

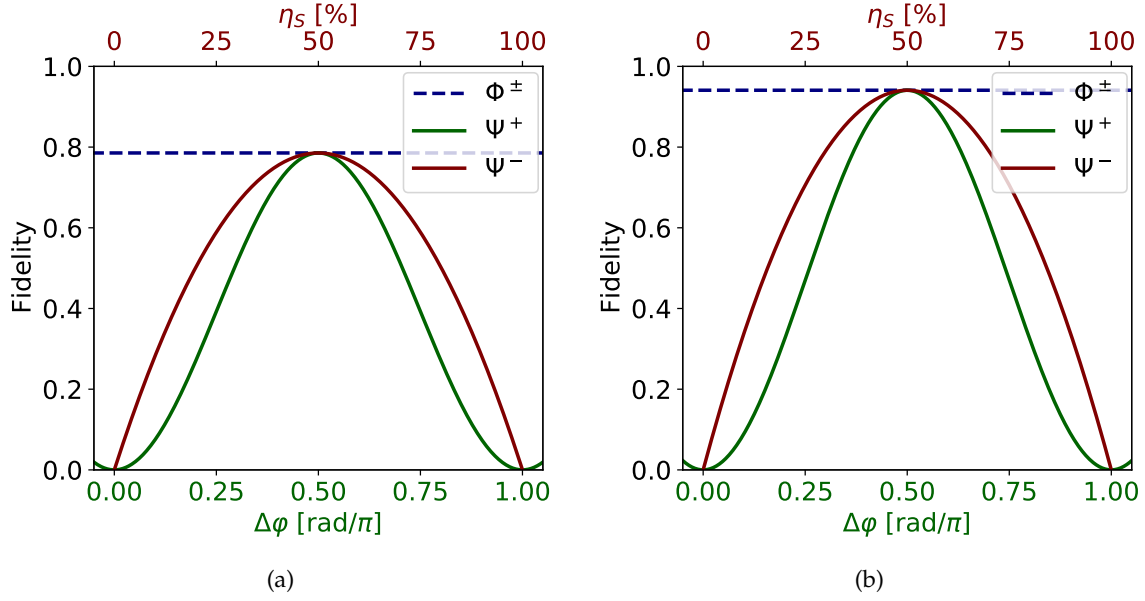


Figure 5.3:

Fidelity estimations of the metasurface output states modelled with defects in eq. (A.4) with respect to the ideal scenario in eq. (5.9).  $\Psi^+$ 's fidelity dependency is plotted with respect to the green(lower) x-axis,  $\Psi^-$ 's fidelity dependency is plotted with to the red(upper) x-axis and  $\Phi^\pm$  is constant over both axis. **(a)** Lower bound fidelity estimation with the photon indistinguishability characterised in section 2.4.2 ( $V_{HOM} = 92.8\%$ ) and a diffraction order contrast of  $\eta_c = 92\%$  reaching a maximum fidelity for all incident Bell states  $F = 78.5\%$ . **(b)** Optimistic scenario with a diffraction order contrast of  $\eta_c = 99\%$  as obtained in two out of four diffraction orders in [67] and a photon indistinguishability of  $V_{HOM} = 96\%$  as achieved in [39], reaching a maximum fidelity for all incident Bell states of  $F = 94.1\%$ .

## 5.4 Summary

This chapter proposed a thin-film metasurface design for carrying out partial Bell state measurements for possible integration in the entanglement gate, or as a heralding station in a DIQKD protocol. The design in the loss-less scenario yields an estimated output state fidelity of  $F = 94.1\%$  based on an optimistic diffraction order contrast and photon indistinguishability achieved on the InAs/GaAs QD platform[39]. A lower bound output state fidelity of  $F = 78.5\%$  is also presented based on the photon indistinguishability achieved in this thesis and the lower bound diffraction order contrast as evaluated in [67].

---

## Chapter 6

# Conclusion and outlook

---

### Conclusion

The first goal of this thesis was to demonstrate temporal-to-spatial mode demultiplexing of a four-photon source from a high-purity, indistinguishable single-photon source based on an InAs/GaAs quantum dot(QD) embedded in a photonic nanostructure. Here a QD was found at wavelength  $\lambda = 942.0\text{nm}$  and the emitted single photon quality characterised. The QD excitation rate of  $F_{ex} = 76.152\text{MHz}$  combined with an expected source efficiency of  $\eta_S \approx 6.1\%$  should result in a single photon rate of  $F_{SP} = 4.6\text{MHz}$ . The achieved single photon rate is  $3.8\text{MHz}$  corresponding to a  $5.1\%$  source efficiency. The experimentally achieved single photon purity of the QD emitted single photons is  $g^{(2)}(\tau = 0) = (0.92 \pm 0.02)\%$  and with a photon indistinguishability of  $V_{HOM} = (92.8 \pm 0.3)\%$ .

The source next underwent a temporal-to-spatial mode conversion in the demultiplexer setup for four spatial output modes. The expected four-fold coincidence rate with respect to the achieved single photon rate is  $22.64\text{Hz}$ . This estimation is consistent with the measured four-fold coincidence rate of  $3.41\text{Hz}$  with a source efficiency of  $3.0\%$ . The HOM visibility measured on overlapped demultiplexer output modes ( $M_{1-4}$ ) is across output  $M_1$  and  $M_2$ :  $V_{HOM,1\&2} = (89.5 \pm 1.8)\%$ , across  $M_1$  and  $M_3$ :  $V_{HOM,1\&3} = (86.9 \pm 1.7)\%$  and across  $M_1$  and  $M_4$ :  $V_{HOM,1\&4} = (84.8 \pm 1.7)\%$  with time difference between the emission of the overlapped photons of  $\Delta t = 262.6\text{ns}$ ,  $\Delta t = 525.3\text{ns}$  and  $\Delta t = 789.9\text{ns}$ , respectively. These visibilities are considered a lower bound for a demultiplexed single photon source with a direct HOM visibility (i.e. measured directly out of the QD single photon source) of  $V_{HOM,source} = (91.1 \pm 1.3)\%$ .

The four-photon source was subsequently implemented in an quantum gate protocol for entanglement generation. The heralding efficiency of the experimental implementation with two non-photon-number-resolving detectors at the heralding station can in the ideal case reach  $P_s = 32.0\%$ , but feasible setup improvements in the form of four photon-number-resolving detectors indicates a heralding efficiency of unity in the ideal case. The experimentally achieved CHSH inequality S-parameter of the heralded entangled output state is  $S = 2.01 \pm 0.10$  for a  $1.458\text{ns}$  coincidence intersection time window, and for a more narrow time window of  $972\text{ps}$  we reach  $S = 2.24 \pm 0.08$ , violating Bells inequality by  $3\sigma$ . The quantum correlation fringe visibility achieved of  $V_{E(22.5^\circ, \theta_2)} = 81.3 \pm 0.8$  predicts an even greater violation of Bell's inequality of  $S = 2.30 \pm 0.02$  i.e. a violation of  $15\sigma$ .

Finally a design proposal for a metasurface grating implementation of a Bell state measurement is presented. The capability to implement linear operations in a thin-film reduces optical loss from absorption, which is crucial for quantum protocols. The design in the loss less scenario yields an estimated output state fidelity of  $F = 94.1\%$  based on an optimistic diffraction order contrast and photon indistinguishability achieved on the introduced InAs/GaAs QD platform. A lower bound output state fidelity of  $F = 78.5\%$  is also presented based on photon indistinguishability achieved in this thesis and the lower bound diffraction order contrast as presented in [67].

## Outlook

The heralded entanglement generator presented in this thesis can be implemented in a E91 based DIQKD scheme by connecting output  $B'$  and  $C'$  to Alice and Bob respectively, thus sending heralded photonic EPR pairs to the two parties. i.e., by connecting a heralding station to output  $A'$  and  $D'$  the arrival of an EPR pair at Alice and Bob's location may be heralded in order to overcome the Bell inequality detection loophole, as required to ensure the privacy of the generated one time-pad key. This is, however, not the only promising utilisation of the of the entanglement gate. The generated heralded Bell states may also be used in quantum random number generators[74] certified by Bell inequality violation[75]. True random number generation is a key components in DIQKD protocols in order to ensure true random measurement basis choices for Alice and Bob. This is enabled with EPR pairs, due to the intrinsic random nature of photonic qubits.

Controlled-NOT(CNOT) gates can be used to implement an arbitrary unitary operation on  $N$  qubits, and are therefore universal for quantum computation[19]. Recently an experimental demonstration of heralded CNOT operation between two single photons has been carried out for the first time[76], with a 1.4Hz operation rate and average gate fidelity of  $F = 87.8\%$ . The experimental implementation of this CNOT gate is in great resemblance to the setup presented in this thesis. It includes a high rate, high purity and indistinguishable QD single photon source actively demultiplexed into four spatial modes coupled to a heralded entanglement gate. The main difference here is the replacement of the PBS superimposing path  $A$  and  $B$  (or  $C$  and  $D$ ) with a PBS in the diagonal/anti-diagonal basis(i.e. transmitting  $|D\rangle$  and reflecting  $|A\rangle$ ) and replacement of the PBS superimposing path  $A$  and  $D$  with a PBS in the right/left circularly polarised basis(i.e. transmitting  $|R\rangle$  and reflecting  $|L\rangle$ ). The latter PBS carries out a partial bell state measurement(BSM) in that basis on path  $A'$  and  $D'$ . The output of the BSM is then classically feed-forwarded to a Pauli operator on path  $B'$  and  $C'$  to execute a CNOT operation. Here incident photons in path  $B$  and  $C$  are considered ancillary photons. This setup expansion poses an interesting alteration to the heralded entanglement gate presented in this thesis, in the context of quantum computations. Especially so, considering the potentially improved single-photon rates of 122MHz presented in [39].

Another more noninvasive improvement of the entanglement gate setup is an expansion of the projective detectors into the circular polarisation domain(i.e. by adding a QWP on each detection arm) on path  $B'$  and  $C'$ . This enables Bell state fidelity analysis of the heralded EPR pairs according to[76, 77]

$$\begin{aligned} F_{\Psi\pm} &= \frac{1 \mp 1 - P_{HH} - P_{VV} \pm P_{DD} \pm P_{AA} \pm P_{RR} \pm P_{LL}}{2}, \\ F_{\Phi\pm} &= \frac{P_{HH} + P_{VV} \pm P_{DD} \pm P_{AA} \mp P_{RR} \mp P_{LL}}{2}, \end{aligned} \quad (6.1)$$

where  $P_{ii}$  is the joint-measurement probability.

Regarding multiphoton sources a relatively simple expansion of the demultiplexing setup is presented in [49]. The setup alteration is in the form of a resonant EOM that enables parallel four-mode demultiplexing using the existing setup. This would enable eight-mode conversion of a single photon source, which paves the way to operation of two parallel entanglement gates generating multiple Bell states with mutual photon indistinguishability. Furthermore, recent developments in nano-opto-electro-mechanical switches[78, 79, 80] have proven an exciting platform for 'on chip' demultiplexing of QD single photon sources. This enables compact and low-loss demultiplexing and/or other QD based photonic quantum networks.

Further design possibilities on the metasurface platform uncludes a design spanning a tetahedron on the Poincare sphere as proposed in[67] for classical light analysis. This design may also be considered for quantum optics full state tomography. In this case a diffraction order overlap is not required, but eight detectors are, for full state tomography of a two-photon state. Beyond state tomography, only the imagination is boundary(almost) to the utilisation of the thin-film metasurafece platform. By cascading metasurfaces, more complex polarisation dependent linear operations with low losses may be enabled, proving an interesting subject in the quantum optics of tomorrow.

---

# Bibliography

---

- [1] Max Planck. Ueber das gesetz der energieverteilung im normalspectrum. *Annalen der Physik*, 309(3):553–563, 1901.
- [2] A. Einstein. Über einen die erzeugung und verwandlung des liches betreffenden heuristischen gesichtspunkt. *Annalen der Physik*, 322(6):132–148, 1905.
- [3] N. Bohr. On the Constitution of Atoms and Molecules. *Phil. Mag. Ser. 6*, 26:1–24, 1913.
- [4] J. J. Sakurai and Jom Napolitano. *Modern Quantum Mechanics*. Cambridge University Press, second edition, 2017.
- [5] A. Einstein, B. Podolsky, and N. Rosen. Can quantum-mechanical description of physical reality be considered complete? *Phys. Rev.*, 47:777–780, May 1935.
- [6] J. S. Bell. On the einstein podolsky rosen paradox. *Physics Physique Fizika*, 1:195–200, Nov 1964.
- [7] B. Hensen, H. Bernien, A. E. Dréau, A. Reiserer, N. Kalb, M. S. Blok, J. Ruitenberg, R. F. L. Vermeulen, R. N. Schouten, C. Abellán, W. Amaya, V. Pruneri, M. W. Mitchell, M. Markham, D. J. Twitchen, D. Elkouss, S. Wehner, T. H. Taminiau, and R. Hanson. Loophole-free bell inequality violation using electron spins separated by 1.3 kilometres. *Nature*, 526(7575):682–686, 2015.
- [8] Marissa Giustina, Marijn A.M. Versteegh, Sören Wengerowsky, Johannes Handsteiner, Armin Hochrainer, Kevin Phelan, Fabian Steinlechner, Johannes Kofler, Jan-Åke Larsson, Carlos Abellán, and et al. Significant-loophole-free test of bell’s theorem with entangled photons. *Physical Review Letters*, 115(25), Dec 2015.
- [9] Lynden K. Shalm, Evan Meyer-Scott, Bradley G. Christensen, Peter Bierhorst, Michael A. Wayne, Martin J. Stevens, Thomas Gerrits, Scott Glancy, Deny R. Hamel, Michael S. Allman, and et al. Strong loophole-free test of local realism. *Physical Review Letters*, 115(25), Dec 2015.
- [10] E. Knill, R. Laflamme, and G. J. Milburn. A scheme for efficient quantum computation with linear optics. *Nature*, 409(6816):46–52, 2001.
- [11] Jonathan Barrett, Lucien Hardy, and Adrian Kent. No signaling and quantum key distribution. *Physical Review Letters*, 95(1), Jun 2005.

- [12] Artur K. Ekert. Quantum cryptography based on bell's theorem. *Phys. Rev. Lett.*, 67:661–663, Aug 1991.
- [13] NewScientist. Ibm unveils its first commercial quantum computer. <https://www.newscientist.com/article/2189909-ibm-unveils-its-first-commercial-quantum-computer/>. [Online; accessed 19-May-2021].
- [14] Stefano Pironio, Antonio Acín, Nicolas Brunner, Nicolas Gisin, Serge Massar, and Valerio Scarani. Device-independent quantum key distribution secure against collective attacks. *New Journal of Physics*, 11(4):045021, Apr 2009.
- [15] Qiang Zhang, Xiao-Hui Bao, Chao-Yang Lu, Xiao-Qi Zhou, Tao Yang, Terry Rudolph, and Jian-Wei Pan. Demonstration of a scheme for the generation of “event-ready” entangled photon pairs from a single-photon source. *Physical Review A*, 77(6), Jun 2008.
- [16] Amir Arbabi, Yu Horie, Mahmood Bagheri, and Andrei Faraon. Dielectric metasurfaces for complete control of phase and polarization with subwavelength spatial resolution and high transmission. *Nature nanotechnology*, 10, 08 2015.
- [17] Charles H. Bennett and Gilles Brassard. Quantum cryptography: Public key distribution and coin tossing. *Theoretical Computer Science*, 560:7–11, Dec 2014.
- [18] John Preskill. Lecture notes for physics 219: Quantum computation. 01 1999, updated 2018.
- [19] Michael A. Nielsen and Isaac L. Chuang. *Quantum Computation and Quantum Information: 10th Anniversary Edition*. Cambridge University Press, 2010.
- [20] Peter Knight Christopher Gerry. *Introductory quantum optics*. Cambridge University Press, 2005.
- [21] Mark Fox. *Quantum optics: an introduction*. Oxford Master Series in Physics, 6. Oxford University Press, USA, 2006.
- [22] John F. Clauser, Michael A. Horne, Abner Shimony, and Richard A. Holt. Proposed experiment to test local hidden-variable theories. *Phys. Rev. Lett.*, 23:880–884, Oct 1969.
- [23] Nicolas Gisin, Grégoire Ribordy, Wolfgang Tittel, and Hugo Zbinden. Quantum cryptography. *Reviews of Modern Physics*, 74(1):145–195, Mar 2002.
- [24] A.J. Menezes, J. Katz, P.C. van Oorschot, and S.A. Vanstone. *Handbook of Applied Cryptography*. Discrete Mathematics and Its Applications. CRC Press, 1996.
- [25] R.L. Rivest, A. Shamir, and L. Adleman. A method for obtaining digital signatures and public-key cryptosystems. *Communications of the ACM*, 21:120–126, 1978.
- [26] Antía Lamas-Linares and Christian Kurtsiefer. Breaking a quantum key distribution system through a timing side channel. *Optics Express*, 15(15):9388, 2007.
- [27] Lars Lydersen, Carlos Wiechers, Christoffer Wittmann, Dominique Elser, Johannes Skaar, and Vadim Makarov. Hacking commercial quantum cryptography systems by tailored bright illumination. *Nature Photonics*, 4(10):686–689, Aug 2010.
- [28] Charles H. Bennett, Gilles Brassard, and N. David Mermin. Quantum cryptography without bell's theorem. *Phys. Rev. Lett.*, 68:557–559, Feb 1992.

- [29] Antonio Acín, Nicolas Brunner, Nicolas Gisin, Serge Massar, Stefano Pironio, and Valerio Scarani. Device-independent security of quantum cryptography against collective attacks. *Physical Review Letters*, 98(23), Jun 2007.
- [30] Jan Kołodyński, Alejandro Máttar, Paul Skrzypczyk, Erik Woodhead, Daniel Cavalcanti, Konrad Banaszek, and Antonio Acín. Device-independent quantum key distribution with single-photon sources. *Quantum*, 4:260, Apr 2020.
- [31] Peter Michler. *Single Semiconductor Quantum Dots*. NanoScience and Technology. Springer, 2009.
- [32] Charles Kittel. *Introduction to Solid State Physics*. John Wiley sons, Inc, eight edition, 2005.
- [33] Steven H. Simon. *The Oxford Solid State Basics*. Oxford University Press, first edition, 2019.
- [34] wikimedia. Band gap comparison. [https://upload.wikimedia.org/wikipedia/commons/thumb/0/0b/Band\\_gap\\_comparison.svg/2000px-Band\\_gap\\_comparison.svg.png](https://upload.wikimedia.org/wikipedia/commons/thumb/0/0b/Band_gap_comparison.svg/2000px-Band_gap_comparison.svg.png). [Online; accessed 11-March-2021].
- [35] G. Kiřsanskè. *Electrical control of excitons in semiconductor nanostructures*. PhD thesis, Niels Bohr Institute, University of Copenhagen, 2012.
- [36] S. Mahmopdian P. Lodahl and S. Stobbe. Interfacing single photons and single quantum dots with photonic nanostructures. *Rev. Mod. Phys.* 87, 347, 2015, 2014.
- [37] Murray Sargent Pierre Meystre. *Elements of Quantum Optics*. Springer, 4th ed edition, 2007.
- [38] Freja Pedersen. *Deterministic Single and Multi-Photon Sources with Quantum dots in Planar Nanostructures*. PhD thesis, Niels Bohr Institute, University of Copenhagen, 2020.
- [39] Ravitej Uppu, Freja T. Pedersen, Ying Wang, Cecilie T. Olesen, Camille Papon, Xiaoyan Zhou, Leonardo Midolo, Sven Scholz, Andreas D. Wieck, Arne Ludwig, and et al. Scalable integrated single-photon source. *Science Advances*, 6(50):eabc8268, Dec 2020.
- [40] M. Arcari, I. Söllner, A. Javadi, S. Lindskov Hansen, S. Mahmoodian, J. Liu, H. Thyrrstrup, E.H. Lee, J.D. Song, S. Stobbe, and et al. Near-unity coupling efficiency of a quantum emitter to a photonic crystal waveguide. *Physical Review Letters*, 113(9), Aug 2014.
- [41] Xiaoyan Zhou, Irina Kulkova, Toke Lund-Hansen, Sofie Hansen, Peter Lodahl, and Leonardo Midolo. High-efficiency shallow-etched grating on gaas membranes for quantum photonic applications. *Applied Physics Letters*, 113:251103, 12 2018.
- [42] C. C. Gerry and P. L. Knight. *Introductory Quantum Optics*. Cambridge University Press, third printing edition, 2008.
- [43] R. Hanbury Brown and R. Q. Twiss. Correlation between photons in two coherent beams of light. *Nature*, 1956.
- [44] R. J. Barlow. *Statistics: A Guide and Reference to the Use of Statistical Methods in the Physical Sciences*. Manchester Physics Series. Wiley, 1993.



- [45] Ou Z. Y. Hong, C. K. and L. Mandel. Measurement of subpicosecond time intervals between two photons by interference. *Physical Review Letters*, 1987.
- [46] K. H. Madsen, S. Ates, J. Liu, A. Javadi, S. M. Albrecht, I. Yeo, S. Stobbe, and P. Lodahl. Efficient out-coupling of high-purity single photons from a coherent quantum dot in a photonic-crystal cavity. *Phys. Rev. B*, 90:155303, Oct 2014.
- [47] Charles Santori, David Fattal, Jelena Vuckovic, Glenn Solomon, and Yoshihisa Yamamoto. Indistinguishable photons from a single-photon device. *Nature*, 419, 10 2002.
- [48] Feng Liu, Alistair J. Brash, John O’Hara, Luis M. P. P. Martins, Catherine L. Phillips, Rikki J. Coles, Benjamin Royall, Edmund Clarke, Christopher Bentham, Nikola Prtljaga, and et al. High purcell factor generation of indistinguishable on-chip single photons. *Nature Nanotechnology*, 13(9):835–840, Jul 2018.
- [49] Thomas Hummel. *Multiphoton generation from a single quantum dot in a photonic nanostructure*. PhD thesis, Niels Bohr Institute, University of Copenhagen, 2019.
- [50] Eberly J.H. Milonni P.W. *Laser Physics*. Wiley, 2 edition, 2010.
- [51] Ela Ugur. *Multi-photon interference towards entanglement generation*. Master’s thesis, Niels Bohr Institute, University of Copenhagen, 2018.
- [52] ThorLabs. Pbs053 spec. sheet. <https://www.thorlabs.com/drawings/a3bea21a9eb94f00-B9A25B86-B470-583E-19AD7EF232E18802/PBS053-AutoCADPDF.pdf>. [Online; accessed 27-April-2021].
- [53] Pauli Virtanen, Ralf Gommers, Travis E. Oliphant, Matt Haberland, Tyler Reddy, David Cournapeau, Evgeni Burovski, Pearu Peterson, Warren Weckesser, Jonathan Bright, Stéfan J. van der Walt, Matthew Brett, Joshua Wilson, K. Jarrod Millman, Nikolay Mayorov, Andrew R. J. Nelson, Eric Jones, Robert Kern, Eric Larson, C J Carey, İlhan Polat, Yu Feng, Eric W. Moore, Jake VanderPlas, Denis Laxalde, Josef Perktold, Robert Cimrman, Ian Henriksen, E. A. Quintero, Charles R. Harris, Anne M. Archibald, Antônio H. Ribeiro, Fabian Pedregosa, Paul van Mulbregt, and SciPy 1.0 Contributors. SciPy 1.0: Fundamental Algorithms for Scientific Computing in Python. *Nature Methods*, 17:261–272, 2020.
- [54] quTools. qutau timetagger spec. sheet. [https://www.qutools.com/products/quTAU/quTAU\\_datasheet.pdf](https://www.qutools.com/products/quTAU/quTAU_datasheet.pdf), 2021. [Online; accessed 10-May-2021].
- [55] Hui Wang, Z.-C. Duan, Y.-H. Li, Si Chen, J.-P. Li, Y.-M. He, M.-C. Chen, Yu He, X. Ding, Cheng-Zhi Peng, and et al. Near-transform-limited single photons from an efficient solid-state quantum emitter. *Physical Review Letters*, 116(21), May 2016.
- [56] Juan C. Loredó, Nor A. Zakaria, Niccolò Somaschi, Carlos Anton, Lorenzo de Santis, Valerian Giesz, Thomas Grange, Matthew A. Broome, Olivier Gazzano, Guillaume Coppola, and et al. Scalable performance in solid-state single-photon sources. *Optica*, 3(4):433, Apr 2016.
- [57] Eugene Hect. *Optics*. Pearson Education. Addison Wesley, fourth edition, 2002.
- [58] Beth Schaefer, Edward Collett, Robert Smyth, Daniel Barrett, and Beth Fraher. Measuring the stokes polarization parameters. *American Journal of Physics - AMER J PHYS*, 75, 02 2007.

- [59] Wikipedia. Stokes parameters. [https://en.wikipedia.org/wiki/Stokes\\_parameters](https://en.wikipedia.org/wiki/Stokes_parameters). [Online; accessed 21-April-2021].
- [60] Paul Williams. Rotating-wave-plate stokes polarimeter for differential group delay measurements of polarization-mode dispersion. *Applied optics*, 38:6508–15, 12 1999.
- [61] Dennis H. Goldstein. *Polarized Light, Revised and Expanded (Optical Science and Engineering)*. CRC Press, 2 edition, 2003.
- [62] Edward A. Lee David G. Messerschmitt. *Digital Communication, 2nd Edition*. 2 edition, 1993.
- [63] H. T. Eriksen. *Heralded Entanglement Generation with Quantum Dot Single Photon Sources*. Master’s thesis, Niels Bohr Institute, University of Copenhagen, 2020.
- [64] A. Einstein, B. Podolsky, and N. Rosen. Can quantum-mechanical description of physical reality be considered complete? *Phys. Rev.*, 47:777–780, May 1935.
- [65] Hans Dembinski and Piti Ongmongkolkul et al. scikit-hep/iminuit. Dec 2020.
- [66] Eva María G. Ruiz. *Study of InGaAs quantum dots as single-photon sources for Device-Independent Quantum Key Distribution*. Master’s thesis, Niels Bohr Institute, University of Copenhagen, 2019.
- [67] Noah Rubin, Gabriele DâAversa, Paul Chevalier, Zhujun Shi, Wei Ting Chen, and Federico Capasso. Matrix fourier optics enables a compact full-stokes polarization camera. *Science*, 365:eaax1839, 07 2019.
- [68] Nanfang yu and Federico Capasso. Flat optics with designer metasurfaces. *Nature materials*, 13:139–50, 01 2014.
- [69] Alexander V. Kildishev, Alexandra Boltasseva, and Vladimir M. Shalaev. Planar photonics with metasurfaces. *Science*, 339(6125), 2013.
- [70] Kai Wang, James G. Titchener, Sergey S. Kruk, Lei Xu, Hung-Pin Chung, Matthew Parry, Ivan I. Kravchenko, Yen-Hung Chen, Alexander S. Solntsev, Yuri S. Kivshar, Dragomir N. Neshev, and Andrey A. Sukhorukov. Quantum metasurface for multiphoton interference and state reconstruction. *Science*, 361(6407):1104–1108, 2018.
- [71] R. Bekenstein, I. Pikovski, H. Pichler, E. Shahmoon, S. F. Yelin, and M. D. Lukin. Quantum metasurfaces with atom arrays. *Nature Physics*, 16(6):676–681, Mar 2020.
- [72] Pascal Berto, Laurent Philippet, Johann osmond, Chang Liu, Adeel Afridi, Marc Marques, Bernat Agudo, Gilles Tessier, and Romain Quidant. Tunable and free-form planar optics. *Nature Photonics*, 09 2019.
- [73] Joseph W Goodman. *Introduction to Fourier Optics*. McGraw-Hill series in electrical and computer engineering. McGraw-Hill, 2nd ed edition, 1996.
- [74] Miguel Herrero-Collantes and Juan Carlos Garcia-Escartin. Quantum random number generators. *Reviews of Modern Physics*, 89(1), Feb 2017.
- [75] S. Pironio, A. Acín, S. Massar, A. Boyer de la Giroday, D. N. Matsukevich, P. Maunz, S. Olmschenk, D. Hayes, L. Luo, T. A. Manning, and et al. Random numbers certified by bell’s theorem. *Nature*, 464(7291):1021–1024, Apr 2010.

- [76] Jin-Peng Li, Xuemei Gu, Jian Qin, Dian Wu, Xiang You, Hui Wang, César Schneider, Sven Höfling, Yong-Heng Huo, Chao-Yang Lu, Nai-Le Liu, Li Li, and Jian-Wei Pan. Heralded non-destructive quantum entangling gate with single-photon sources. 10 2020.
- [77] Andrew G. White, Alexei Gilchrist, Geoffrey J. Pryde, Jeremy L. O'Brien, Michael J. Bremner, and Nathan K. Langford. Measuring two-qubit gates. *Journal of the Optical Society of America B*, 24(2):172, jan 2007.
- [78] Peter Lodahl. Quantum-dot based photonic quantum networks. *Quantum Science and Technology*, 3(1):013001, oct 2017.
- [79] Leonardo Midolo, Albert Schliesser, and Andrea Fiore. Nano-opto-electro-mechanical systems. *Nature Nanotechnology*, 13(1):11–18, 2018.
- [80] Camille Papon, Xiaoyan Zhou, Henri Thyrrestrup, Zhe Liu, Søren Stobbe, Rüdiger Schott, Andreas D. Wieck, Arne Ludwig, Peter Lodahl, and Leonardo Midolo. Nanomechanical single-photon routing. *Optica*, 6(4):524–530, Apr 2019.
- [81] Chandra M Natarajan, Michael G Tanner, and Robert H Hadfield. Superconducting nanowire single-photon detectors: physics and applications. *Superconductor Science and Technology*, 25(6):063001, Apr 2012.

---

# Appendix A

## Appendix

---

### A.1 Single photon detectors

Two common detectors used for single photon detection are *Avalanche Photodiode (APD)* and *Superconducting Nano-wire Single Photon Detectors (SNSPD)*. Both type of photon detectors are used in this thesis.

#### Avalanche Photodiode(APD)

APDs consists of semiconductor in a P-N junction reversely biased. The electric field is so high that a single charge carrier injected into the system can trigger a self-sustaining avalanche which functions as a trigger signal. When a photon hits the APD the photoelectric effect excites a such charge carrier and triggers this mechanism. The APD have a typical recovery profile of a Heaviside function. The APDs used in this work is for timing purposes, why a special fast APD is used, that suffers from a very low efficiency at the operational wavelength but high time resolution. For acquiring time stamps of the single photon events a PicoQuant time tagger *PicoHarp 300* with a 4 ps. bin size is used together with the fast APD.

#### Superconducting Nanowire Single Photon Detector(SNSPD)

SNSPDs consists of sputtered niobium nitride (NbN) nanowire maintained well below superconducting critical temperature  $T_c \approx 17.4\text{K}$  and current biased just below its critical current. Individual infrared photons have enough energy to disrupt hundreds of Cooper pairs in a superconductor and thereby forming a hotspot effectively increasing the resistance from zero, which generates a measurable output voltage pulse across the nanowire[81].

Four SNSPDs are dedicated for the entanglement experimens. All four detector channels are connected to the setup by optical fibers spliced on to the detectors with an estimated efficiency of  $\simeq 98\%$ . The fibers have have a transport efficiency of  $\simeq 94\%$  and the detectors them selves are specified at  $> 95\%$  efficiency, resulting in a total detector efficiency of for the SNSPD channels of  $\eta_{det} = (88 \pm 1)\%$ . For source characterisation two SNSPDs are dedicated with a measured 65% efficiency.

The SNSPD have an exponential recovery profile, where the dead time is determined by the time the detector needs to reach back 95% of the original efficiency. The dead time for all

SNSPDs used in the experimental work is  $\tau_{dead} = 70$  ns. The detector details are summarised in table A.1.

Detector	Efficiency at 940 nm	Resolution FWHM	Dark counts	Deadtime ( $\tau_{dead}$ )
SNSPD	88%(65%)	200ps	< 5Hz	70ns
Fast APD	1%	40 ps	$\sim 300$ Hz	50ns

Table A.1: Performance of the single photon detectors used in the experimental work. Resolution is here referring to the timing jitter of the detectors as characterised in [38]. The efficiency in parenthesis() are the for the source dedicated SNSPD, the other is entanglement gate and demultiplexer dedicated SNSPDs.

## A.2 Transformation matrices of optical elements in partial Bell state measurement

Beamsplitter transformation matrix:

$$\begin{pmatrix} \hat{a}'_H^\dagger \\ \hat{a}'_V^\dagger \\ \hat{p}'_H^\dagger \\ \hat{p}'_V^\dagger \\ \hat{d}'_H^\dagger \\ \hat{d}'_V^\dagger \\ \hat{q}'_H^\dagger \\ \hat{q}'_V^\dagger \end{pmatrix} = \underbrace{\begin{bmatrix} \frac{1}{\sqrt{2}} & 0 & 0 & 0 & \frac{i}{\sqrt{2}} & 0 & 0 & 0 \\ 0 & \frac{1}{\sqrt{2}} & 0 & 0 & 0 & \frac{i}{\sqrt{2}} & 0 & 0 \\ 0 & 0 & 1 & 0 & 0 & 0 & 0 & 0 \\ 0 & 0 & 0 & 1 & 0 & 0 & 0 & 0 \\ \frac{i}{\sqrt{2}} & 0 & 0 & 0 & \frac{1}{\sqrt{2}} & 0 & 0 & 0 \\ 0 & \frac{i}{\sqrt{2}} & 0 & 0 & 0 & \frac{1}{\sqrt{2}} & 0 & 0 \\ 0 & 0 & 0 & 0 & 0 & 0 & 1 & 0 \\ 0 & 0 & 0 & 0 & 0 & 0 & 0 & 1 \end{bmatrix}}_{M_{BS}} \begin{pmatrix} \hat{a}^\dagger_H \\ \hat{a}^\dagger_V \\ \hat{p}^\dagger_H \\ \hat{p}^\dagger_V \\ \hat{d}^\dagger_H \\ \hat{d}^\dagger_V \\ \hat{q}^\dagger_H \\ \hat{q}^\dagger_V \end{pmatrix}. \quad (\text{A.1})$$

Transformation matrix of two PBS, one on each output arm of the BS:

$$\begin{pmatrix} \hat{a}''_H^\dagger \\ \hat{a}''_V^\dagger \\ \hat{p}''_H^\dagger \\ \hat{p}''_V^\dagger \\ \hat{d}''_H^\dagger \\ \hat{d}''_V^\dagger \\ \hat{q}''_H^\dagger \\ \hat{q}''_V^\dagger \end{pmatrix} = \underbrace{\begin{bmatrix} 1 & 0 & 0 & 0 & 0 & 0 & 0 & 0 \\ 0 & 0 & 0 & i & 0 & 0 & 0 & 0 \\ 0 & 0 & 1 & 0 & 0 & 0 & 0 & 0 \\ 0 & i & 0 & 0 & 0 & 0 & 0 & 0 \\ 0 & 0 & 0 & 0 & 1 & 0 & 0 & 0 \\ 0 & 0 & 0 & 0 & 0 & 0 & 0 & i \\ 0 & 0 & 0 & 0 & 0 & 0 & 1 & 0 \\ 0 & 0 & 0 & 0 & 0 & i & 0 & 0 \end{bmatrix}}_{M_{PBS}} \begin{pmatrix} \hat{a}^\dagger_H \\ \hat{a}^\dagger_V \\ \hat{p}^\dagger_H \\ \hat{p}^\dagger_V \\ \hat{d}^\dagger_H \\ \hat{d}^\dagger_V \\ \hat{q}^\dagger_H \\ \hat{q}^\dagger_V \end{pmatrix}. \quad (\text{A.2})$$

Combined transformation matrix of the BS and two PBSs forming the partial Bell state measurement:

$$\begin{pmatrix} \hat{a}''^\dagger_H \\ \hat{a}''^\dagger_V \\ \hat{p}''^\dagger_H \\ \hat{p}''^\dagger_V \\ \hat{d}''^\dagger_H \\ \hat{d}''^\dagger_V \\ \hat{q}''^\dagger_H \\ \hat{q}''^\dagger_V \end{pmatrix} = \mathbf{M}_{PBS} \mathbf{M}_{BS} \begin{pmatrix} \hat{a}^\dagger_H \\ \hat{a}^\dagger_V \\ \hat{p}^\dagger_H \\ \hat{p}^\dagger_V \\ \hat{d}^\dagger_H \\ \hat{d}^\dagger_V \\ \hat{q}^\dagger_H \\ \hat{q}^\dagger_V \end{pmatrix} = \begin{bmatrix} \frac{1}{\sqrt{2}} & 0 & 0 & 0 & \frac{i}{\sqrt{2}} & 0 & 0 & 0 \\ 0 & 0 & 0 & i & 0 & 0 & 0 & 0 \\ 0 & 0 & i & 0 & 0 & 0 & 0 & 0 \\ 0 & \frac{i}{\sqrt{2}} & 0 & 0 & 0 & -\frac{1}{\sqrt{2}} & 0 & 0 \\ \frac{i}{\sqrt{2}} & 0 & 0 & 0 & \frac{1}{\sqrt{2}} & 0 & 0 & 0 \\ 0 & 0 & 0 & 0 & 0 & 0 & 0 & i \\ 0 & 0 & 0 & 0 & 0 & 0 & i & 0 \\ 0 & -\frac{1}{\sqrt{2}} & 0 & 0 & 0 & \frac{i}{\sqrt{2}} & 0 & 0 \end{bmatrix} \begin{pmatrix} \hat{a}^\dagger_H \\ \hat{a}^\dagger_V \\ \hat{p}^\dagger_H \\ \hat{p}^\dagger_V \\ \hat{d}^\dagger_H \\ \hat{d}^\dagger_V \\ \hat{q}^\dagger_H \\ \hat{q}^\dagger_V \end{pmatrix}. \quad (\text{A.3})$$

### A.3 Metasurface design transformation matrix

Assuming the spatial and temporal overlap to be perfect after the 2f Fourier imaging setup in fig. 5.2a, the transformation matrix of the metasurface design in fig. 5.2 including defects is shown in eq. (A.4). Here the variables before the double vertical line are multipliers for that row.  $\eta_L$  is the overall efficiency of the setup, such that  $\sqrt{1 - \eta_L}$  is coupled into a lossy state  $\hat{L}$ .  $\eta_S$  is the splitting ratio between the orders with shared polarisation dependency, ideally this is  $\eta_S = 1/2$ .  $\eta_C$  is the diffraction order contrast of the metasurface.  $\phi_0$  and  $\phi_1$  are the phase shift of the diffraction orders, ideally  $\phi_0 = 0$  and  $\phi_1 = \pi/2$ .  $V$  is the indistinguishably of the incident single photons, and  $\hat{\beta}^\dagger_{(m,n),j}$  with  $j \in \{H, V\}$  is the creation operator of a distinguishable photon in the spatial mode  $(m, n)$ . For simplification we assume that all orders have the same defects.

$$\begin{pmatrix} \hat{\alpha}_{(1,0),H}^\dagger \\ \hat{\alpha}_{(1,0),V}^\dagger \\ \hat{\alpha}_{(0,1),H}^\dagger \\ \hat{\alpha}_{(0,1),V}^\dagger \\ \hat{\alpha}_{(-1,0),H}^\dagger \\ \hat{\alpha}_{(-1,0),V}^\dagger \\ \hat{\alpha}_{(0,-1),H}^\dagger \\ \hat{\alpha}_{(0,-1),V}^\dagger \\ \hat{\beta}_{(1,0),H}^\dagger \\ \hat{\beta}_{(1,0),V}^\dagger \\ \hat{\beta}_{(0,1),H}^\dagger \\ \hat{\beta}_{(0,1),V}^\dagger \\ \hat{\beta}_{(-1,0),H}^\dagger \\ \hat{\beta}_{(-1,0),V}^\dagger \\ \hat{\beta}_{(0,-1),H}^\dagger \\ \hat{\beta}_{(0,-1),V}^\dagger \\ \hat{L} \end{pmatrix} = \frac{1}{\sqrt{2}} \begin{pmatrix} \sqrt{\sqrt{V}\eta_L} \\ \sqrt{\sqrt{V}\eta_L} \\ \sqrt{\sqrt{V}\eta_L} \\ \sqrt{\sqrt{V}\eta_L} \\ \sqrt{\sqrt{V}\eta_L} \\ \sqrt{\sqrt{V}\eta_L} \\ \sqrt{\sqrt{V}\eta_L} \\ \sqrt{\sqrt{V}\eta_L} \\ \sqrt{(1-\sqrt{V})\eta_L} \\ \sqrt{(1-\sqrt{V})\eta_L} \\ \sqrt{(1-\sqrt{V})\eta_L} \\ \sqrt{(1-\sqrt{V})\eta_L} \\ \sqrt{(1-\sqrt{V})\eta_L} \\ \sqrt{(1-\sqrt{V})\eta_L} \\ \sqrt{(1-\sqrt{V})\eta_L} \\ \sqrt{(1-\sqrt{V})\eta_L} \\ \sqrt{1-\eta_L} \\ \sqrt{1-\eta_L} \\ \sqrt{1-\eta_L} \\ \sqrt{1-\eta_L} \\ 1 \end{pmatrix} \begin{pmatrix} e^{i\phi_0}\sqrt{\eta_C\eta_S} & 0 & e^{i\phi_1}\sqrt{\eta_C\eta_S} & 0 \\ 0 & e^{i\phi_0}\sqrt{(1-\eta_C)\eta_S} & 0 & e^{i\phi_1}\sqrt{(1-\eta_C)\eta_S} \\ e^{i\phi_1}\sqrt{(1-\eta_C)\eta_S} & 0 & e^{i\phi_0}\sqrt{(1-\eta_C)\eta_S} & 0 \\ 0 & e^{i\phi_1}\sqrt{\eta_C\eta_S} & 0 & e^{i\phi_0}\sqrt{\eta_C\eta_S} \\ e^{i\phi_1}\sqrt{\eta_C(1-\eta_S)} & 0 & e^{i\phi_0}\sqrt{\eta_C(1-\eta_S)} & 0 \\ 0 & e^{i\phi_1}\sqrt{(1-\eta_C)(1-\eta_S)} & 0 & e^{i\phi_0}\sqrt{(1-\eta_C)(1-\eta_S)} \\ e^{i\phi_0}\sqrt{(1-\eta_C)(1-\eta_S)} & 0 & e^{i\phi_1}\sqrt{(1-\eta_C)(1-\eta_S)} & 0 \\ 0 & e^{i\phi_0}\sqrt{\eta_C(1-\eta_S)} & 0 & e^{i\phi_1}\sqrt{\eta_C(1-\eta_S)} \\ e^{i\phi_0}\sqrt{\eta_C\eta_S} & 0 & e^{i\phi_1}\sqrt{\eta_C\eta_S} & 0 \\ 0 & e^{i\phi_0}\sqrt{(1-\eta_C)\eta_S} & 0 & e^{i\phi_1}\sqrt{(1-\eta_C)\eta_S} \\ e^{i\phi_1}\sqrt{(1-\eta_C)\eta_S} & 0 & e^{i\phi_0}\sqrt{(1-\eta_C)\eta_S} & 0 \\ 0 & e^{i\phi_1}\sqrt{\eta_C\eta_S} & 0 & e^{i\phi_0}\sqrt{\eta_C\eta_S} \\ e^{i\phi_1}\sqrt{\eta_C(1-\eta_S)} & 0 & e^{i\phi_0}\sqrt{\eta_C(1-\eta_S)} & 0 \\ 0 & e^{i\phi_1}\sqrt{(1-\eta_C)(1-\eta_S)} & 0 & e^{i\phi_0}\sqrt{(1-\eta_C)(1-\eta_S)} \\ e^{i\phi_0}\sqrt{(1-\eta_C)(1-\eta_S)} & 0 & e^{i\phi_1}\sqrt{(1-\eta_C)(1-\eta_S)} & 0 \\ 0 & e^{i\phi_0}\sqrt{\eta_C(1-\eta_S)} & 0 & e^{i\phi_1}\sqrt{\eta_C(1-\eta_S)} \\ \sqrt{1-\eta_L} & \sqrt{1-\eta_L} & \sqrt{1-\eta_L} & \sqrt{1-\eta_L} \\ & & & 1 \end{pmatrix} \begin{pmatrix} \hat{a}_H^\dagger \\ \hat{a}_V^\dagger \\ \hat{d}_H^\dagger \\ \hat{d}_V^\dagger \\ \hat{L} \end{pmatrix} \quad (\text{A.4})$$